Theses and Dissertations   Graduate School

2023

A sustainable ultrafiltration of sub-20 nm nanoparticles in water and isopropanol: experiments, theory and machine learning

Jie McAtee
Virginia Commonwealth University

1

A sustainable ultrafiltration of sub-20 nm nanoparticles in water and isopropanol: experiments, theory and machine learning

A dissertation submitted in partial fulfillment of the requirements for the degree of Doctor of Philosophy at Virginia Commonwealth University

By

Jie Z McAtee

Ph.D., Heating, Ventilation, and Air conditioning Engineer, Tianjin University, China, 2017

M.S., Heating, Ventilation, and Air conditioning Engineer, Beijing University of Civil Engineering and Architecture, China, 2012

B.S., Heating, Ventilation, and Air conditioning Engineer, Beijing University of Civil Engineering and Architecture, China, 2009

Advisor: Sheng-Chieh Chen

Assistant Professor, Department of Mechanical and Nuclear Engineering

Virginia Commonwealth University

Richmond, Virginia

May 2023

Acknowledgment

I would like to express my sincere gratitude to my supervisor, Prof. Sheng-Chieh Chen, for his unwavering support, constructive advice, and invaluable guidance during my Ph.D. study. Prof. Chen's professionalism, positive attitude, and motivation have inspired me to become a better researcher and a better person. I am grateful not only for his academic mentorship but also for his personal support and sharing of life experiences. I am also deeply grateful to Prof. Chen's wife and family for making my time in a foreign country easier and more enjoyable.

I would also like to thank my dissertation committee members, Prof. Daren Chen, Prof. Hong Zhao, Prof. Ka Un Lao, and Prof. Jing Wang, for their expertise, insightful comments, and guidance, which have been instrumental in shaping my research. I am also grateful to Prof. Dmitry Pestov and Prof. Carl Mayer for their technical support and assistance in material characterization at the VCU facility center. Special thanks also go to Wilson Poon and Prof. Longest for their support and inspiring suggestions, as well as Tianwei Liu, Jianping Chen, and Sarah Strickler for their comforting words and encouragement.

I wish to express my heartfelt appreciation to my beloved husband, Collin McAtee, for his unwavering support during my PhD journey. His constant emotional encouragement and willingness to discuss technical problems with me were invaluable in helping me navigate the challenges I encountered along the way. I will always cherish the memories of him staying by my side while I conducted experiments in the lab, even during late-night hours. In addition, his selflessness in taking care of household chores and cooking allowed me to focus on my research and dissertation writing. I am truly blessed to have such a wonderful partner who believed in me and supported me in every way possible.

Tables of Contents

List of Figures

Figure 4.1 Schematic of ultrafiltration for nanoparticles smaller than 10 mn. VDW is the Van del Waals interaction, which is cause by correlations in the fluctuating polarizations of nearby particles. EDL is the electrostatic double layer interaction. The blue dots and the green dots in the figures

7

List of Tables

Abstract

A SUSTAINABLE ULTRAFILTRATION OF SUB-20 NM NANOPARTICLES IN WATER AND

ISOPROPANOL: EXPERIMENTS, THEORY AND MACHINE LEARNING

By Jie Z McAtee

A dissertation submitted in partial fulfillment of the requirements for the degree of Doctor of Philosophy at Virginia Commonwealth University

Virginia Commonwealth University, 2023

Advisor: Dr. Sheng-Chieh Chen

Assistant Professor, Department of Mechanical and Nuclear Engineering

This research focused on ultrafiltration (UF) for particles down to 2 nm against membranes with pore sizes larger than 100 nm in water and IPA. Unlike the use of nanofiltration (NF) membranes (small pore sizes of 2, 5, and 10 nm) that remove nanoparticles through sieving, which results in high energy consumption, ultrafiltration (UF) with a high ratio of pore size to particle size has the potential to save up to 90% of energy. Considering the widespread use of NF membranes in various industries, such as pharmaceuticals, biochemistry, food, and water treatment, it is essential and urgent to investigate the potential of energy-efficient filtration methods.

To study the UF under large pore to particle diameter ratio (PPDR) condition, a measurement method capable of effectively measuring nanoparticles down to several nanometers in size needed

to be developed. Most of the measurement methods are either time consuming or incapable of measuring particles down to 2 nm. This study combined electrospray (ES) with scanning mobility particle sizer (SMPS) to measure the small particles. The ES was able to aerosolize colloids from water and IPA with minimal loss and no measurement interference, allowing the SMPS to measure the aerosols accurately down to 2 nm. This fast and effective method provides timely and precise data. To further verify the measurement results, the collected particles were observed by scanning electron microscope (SEM). The images showed that individual particles were successfully generated by the ES and the size measured by SMPS matched with the size provided by the manufacturer. The ES-SMPS system was used to obtain the retention efficiency for different sizes of ZnS, Au and PSL challenged on different pore sizes of polytetrafluoroethylene (PTFE), polyvinylidene fluoride (PVDF) and polycarbonate (PCTE) membranes. Results showed that the retention efficiencies in IPA were higher than that of water for all three membranes. The surface electrical enhanced PTFE had a comparable or greater efficiency for all four sizes of NPs than the PCTE. In addition, the highest efficiency was found to be ~80% with 10 nm Au nanoparticle challenged on 100 nm rated PTFE membrane among all the available experimental conditions, which demonstrated the feasibility of the proposed sustainable UF.

In order to gain a deeper understanding of the experimental results, theoretical calculations were required. However, there has been a lack of models that can accurately predict the retention efficiency of small particles in medium-polarity organic solvents. While Derjaguin, Landau, Verwey and Overbeek (DLVO) models are commonly used to qualitatively predict the deposition of colloidal particles, a quantitative model was needed in this case. To achieve this, transport models were incorporated, the DLVO models were modified for the organic solvent, and a Maxwell model was added. The new models were validated by comparing the experimental data

with the calculated data, and the filtration efficiencies were explained using the validated model. This study found that the use of IPA led to higher retention efficiency mainly due to the change of AB interaction from repulsion to attraction. Enhancing the electric attraction could form a secondary minimum, which promoted the deposition of nanoparticles. These findings suggest that the 80% efficiency observed in the experiments, though surprising, can still be improved. Further optimization is needed to achieve satisfactory results.

It is not practical to use experimental method to find the optimal solution, and numerous trail and error cases need to be run to obtain the approximately optimal condition by theoretical calculation. In order to provide a convenient and effective method to obtain the best solution, machine learning was applied in our research. Although machine learning models have been widely used to study fouling and membrane fabrications, no model has been built for optimizing filtration conditions for UF. In this study, the UF performance was optimized by combining a multilayer perceptron artificial neural network (MLP-ANN) with a particle swarm optimization algorithm (PSO). The inputs included membrane zeta potential, pore size, particle size, particle zeta potential, and Hamaker constant, while the output was the retention efficiency. The model was trained, tested, and validated using data obtained from experiments, as well as calculated retention efficiencies for various nanoparticles (Au, ZnS, SiO_2, Al_2O_3, Si_3N_4, and PSL) with sizes ranging from 5-100 nm against PTFE, PVDF, and PCTE membranes with sizes ranging from 50-200 nm. The ANN model provided highly correlated predicted values with target values, as indicated by R^2 values of 0.996, 0.992, and 0.962 for the training, validation, and test datasets, respectively. The PSO model was then used to find the optimized combination of inputs that would result in the highest retention efficiency and lowest energy use. The results showed that a filtration efficiency of 99.9% could be achieved by using 3.4 nm Si3N4 (with a zeta potential of 36.5 mV)

on the PCTE membrane and 28.4 nm ZnS (with a zeta potential of -20.8 mV) on the PTFE membrane. If the membrane or particle type was not pre-determined, the conditions to achieve a filtration efficiency of 99.9% were a 52.2 nm filter with a -20.3 mV zeta potential, 5.5 nm nanoparticles with a 41.4 mV zeta potential, and a combined Hamaker constant. The model can be extended to predict and optimize most of the UF applied in pharmaceutical, biochemical, food, and water treatment industries.

This research utilized experimental method to verify feasibility of using large pore size membrane to filter small particles. Theoretical models for deposition of small NPs in organic solvent were developed and applied to explain the mechanisms. By establishing PSO and ANN models, the filtration conditions were optimized to attain a retention efficiency of 99.9%, resulting in the attainment of a sustainable design.

Chapter 1. Introduction

1.1 Sustainability of liquid filtration

Liquid filtration is a contamination control method for process liquids. Filtration membranes are applied to remove particle, gel, agglomerate and metal ion contamination in chemicals, water and other process materials. Based on the pore size or operation pressure (or transmembrane pressure, TMP), liquid filtration can be categorized into microfiltration (MF), ultrafiltration (UF), nanofiltration (NF) and reverse osmosis (RO) (Fig.1.1) [1].
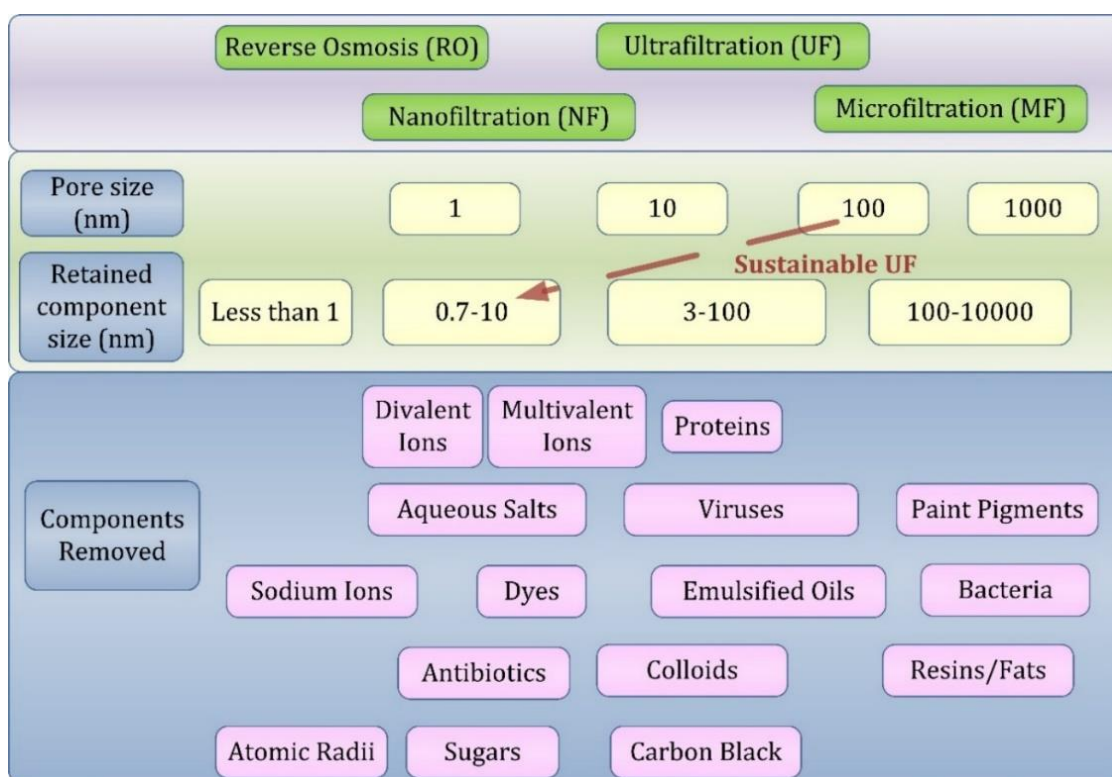
Figure 1.1 Pressure-driven membrane filtration. The red dash line means the proposed method of using 100 nm pore size membrane to filter 0.7-10 nm particles, which is energy efficient

For liquid filtration, sieving, diffusion, interception, impaction and electric exclusion are the main removal mechanisms. Among them, sieving is very important for MF, UF and NF, and electric exclusion is essential for NF and RO. By sieving, MF is usually used to remove bacteria,

turbidity and fine particles in sizes > 100 nm (Fig.1.1). UF is usually for the removal of viruses, endotoxins, proteins and silica, which have sizes of > 20 nm. As NF uses both sieving and electric exclusion mechanisms for solutes removal, its applications are more widely including industries of drinking water and wastewater treatment, oil and petroleum, food, pharmaceutical, textile, biomedical, semiconductor, etc.[2]. NF shares many similar characteristics with RO but requires a lower TMP than RO, thus, it is capable to retain small substance such as ions but more energy efficient. Encouraged by this idea and noticed that UF also shares the sieving characteristics with NF but requires lower TMP, researchers consider using UF to substitute NF to remove sub-10 nm particles using the mechanism of electric exclusion rather than sieving exclusion to save energy (Red dash line in Fig.1.1).

A potential application for this is in semiconductor manufacturing. Tons of water or processing liquids are used in daily current integrated circuit (IC) production [3] and the particle level in the water or chemicals is required to be less than 30 particles/ml of size greater than the 6.5 nm in 2022 according to the international technology roadmap for semiconductors (ITRS) [4]. Generally, the dead-end filtration uses NF (typically pore sizes 1~10 nm) membranes with very small pores, e.g., 2, 5 and 10 nm rated, to remove the nanoparticles by sieving, which results in high energy consumption (Top left figure in Fig.1.2). Hu et al. [5] and Lee [6] reported that approximately 60,000 megawatt-hour energy was used just for performing the liquid filtrations. The use of energy is expecting to further increase with decreasing feature (node) sizes because the critical particle size, defined as the size above which a particle presented in cleanroom air, processing gases and processing liquids, is shirking. For saving energy, the feasibility of using large-pored membranes (Top right figure in Fig.1.2), i.e., ultrafiltration (UF, membrane pore sizes 10~100 nm), to collect small nanoparticles (NPs) with 1.7, 5, 6.6 and 10 nm in aqueous systems

17

was first reported by Chen et al. [7] and Lee et al. [8]. Their studies showed that the TMP was reduced to 0.2-0.3 bar when filtering water with 2-10 nm particles by membranes with pore sizes of 25~100 nm compared to 1-20 bars by membranes with 1-10 nm pores. This means the energy consumption can be reduced by more than 90%, around 54 GWh (gigawatt-hour) and saving $378M per year assuming having 100 of 3-5 nm Fabs in the US in the near future (Fig.1.2). However, it should be noted that the processing liquid used in semiconductor factories include other chemical liquids (acid, base and IPA etc.) than water [9], thus the performance of UF in non-aqueous system still needs to be studied.
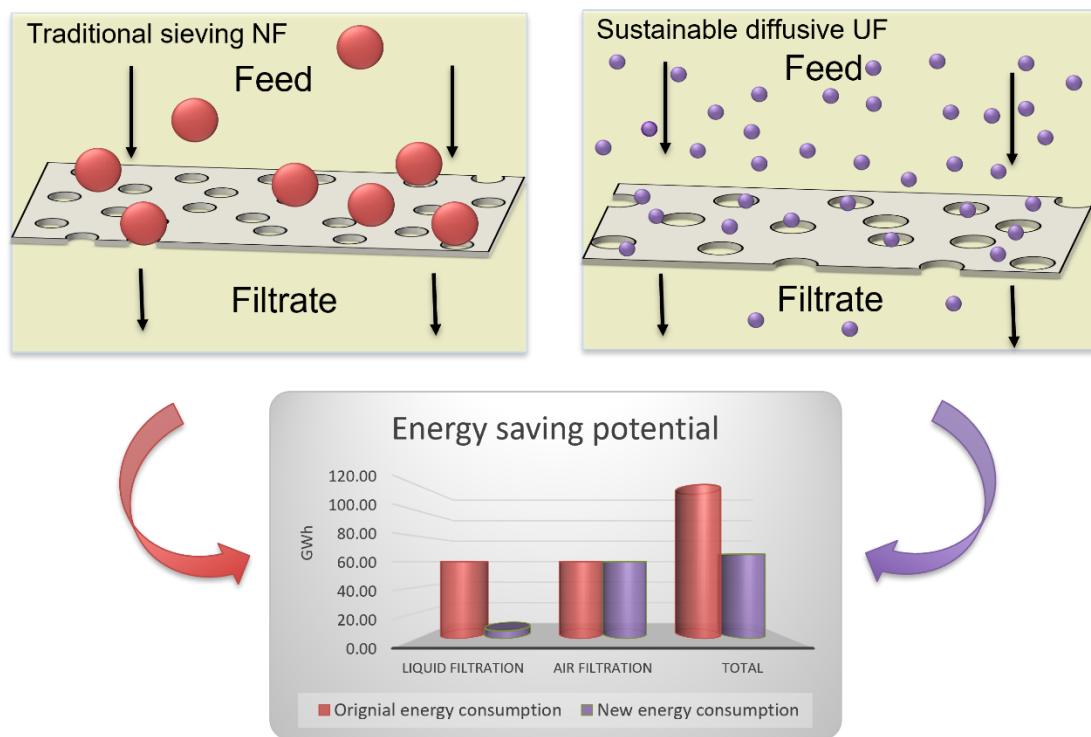
Figure 1.2 Potential energy savings by using UF membrane with large pore size to filter small particles

18

1.2 Methods to measure small nanoparticles in different liquids

Membrane ultrafiltration has been widely studied in aqueous system including particle removal in municipal water and wastewater treatments [10-13] as well as process liquids in various industries such as semiconductor [14], pharmaceuticals [15], food and beverage [16]. Different from aqueous solution, IPA is a slight polar organic solvent which can change the performance of UF. For example, the dielectric constant and zeta potential can be changed when IPA solution is used instead of water [17]. For liquid filtration, electric exclusion is a crucial removal mechanism and affected by the dielectric constant and zeta potential. Therefore, the retention efficiency would be significantly varied [18]. However, studies on UF in IPA are limited. To our best knowledge, there is only one literature [19]reported retention efficiency when 10 nm nanoparticles were challenged on 10 nm pore size different membranes in IPA. The major mechanism for UL of this paper was still sieving. As mentioned in the introduction part, this is not energy efficient and different from our research goal, so it is necessary to perform more studies on UL in IPA with small ratio of particle size to pore size (PPD).

Measuring small particles (down to 2 nm) in IPA is also a challenge. Methods that can measure small particles include using dynamic light scattering (DLS), transmission and scanning electron microscopy (TEM/SEM), UV/vis or fluorescence spectroscopy, inductively coupled plasma-mass spectrometry (ICP-MS), nanoparticle tracking analysis (NTA), electrospray-scanning mobility particle sizer (ES-SMPS), as shown in Table 1.1. However, most of these methods have drawbacks. For example, DLS is sensitive to the particle diameter because it analyzes the particle speed by measuring the rate at which the intensity of the scattered light fluctuates and the intensity is proportional to the sixth power of the particle diameter[20]; TEM/SEM are time-consuming and not cost-effective [21]; UV/vis requires relatively high feed

concentrations due to their low sensitivity [7]. Lee et al. [22] applied ICP-MS, NTA and ES-SMPS system to measure particles down to 2 nm in water. Their results showed that ICP-MS had high sensitivity to a wide range of elements and had a broad analytical working concentration range as long as samples meet the mass requirement. In addition, they reported that both NTA and ES-SMPS had good performance in measuring size and count of particles. However, the particles they used were gold NPs in their paper with high refractive index, which is a requirement for applying NTA. It is very difficult to measure particles with low refractive index using NTA and the operation is very complicated. For ES-SMPS, it can be applied to measure particles down to 1 nm and is not sensitive to the material of the particle. However, the liquid medium is an essential factor that determines if the whole system will work [23]. For most of the published literatures used ES-SMPS system, the liquid was water, including Lee's study. When the liquid changes, special treatment or setup needs to apply. A short summary about the characteristics of different measurement methods in measuring small nanoparticles is shown in Table 1.1.

Table 1.1 Features of prevalent measurement methods for particles with sizes below 20 nm

Measurement method	Feature
Liquid particle counter (LPC)	Lower limit size is 20 - 30 nm
Dynamic light scattering (DLS)	Sensitive to the present of small amount of large particles
Nanoparticle tracking analysis (NTA)	Selective to particle material (high refractive index)
TEM/SEM	Time consuming and results could be not representative
ICP-MS	Time consuming and expensive
Electrospray-SMPS (ES-SMPS)	o Size 1 nm to 1000 nm o Economically acceptable o Low sample concentration o Steady cone-jet shape needs to be formed

1.3 Theories for predicting retention efficiency

To explain the experimental results, theoretic models need to be introduced. Unlike air filtration, liquid filtration includes two main processes, i.e., transport and interaction [24]. First of all, particles are transported to the vicinity of the filter (membrane) surface by convection and/or diffusion. To calculation the efficiency due to the transportation, classic air filtration models or capillary tube models can be used depending on if the filter is fibrous membrane or capillary pore membranes (Fig.1.3). The main mechanisms are diffusion and interception. Impaction and settling on the filter surface were not considered due to the negligible inertia and gravity of NPs.

The second process is the interaction between the particles and the membranes (Fig.1.3). The well-known DLVO theory was established by Derjaguin, Landau, Verwey, and Overbeek in the 1940s (Derjaguin and Landau 1941, Verwey and Overbeek 1948) and describes stabilization of charged surfaces interacting through a liquid medium [25]. The DLVO theory explains particle interactions by combining electrostatic potential due to repulsive electrostatic double layer, and attractive London–van der Waals interactions. Although the DLVO theory is often in a good estimate for intersurface forces for surface separations down to about 5 nm [26], researchers also found that classical DLVO theory have some discrepancies when describing many deposition/filtration processes, such as membrane fouling and organic solvent liquid filtration [27]. It is believed that additional interactions existed between the particles and membranes but not being considered is the problem. Brant and Childress [28] demonstrated that acid–base (AB) (polar) interactions was the main reason that resulted the discrepancy between the experimental results and DLVO prediction result. Lee et al. [24] noticed that Born repulsion should be introduced to allows a better description of the interactions when the particles come close to the collector surface with distances of a few nanometers and less. Wijenayaka et al. [29] and Fjordbøge et al. [30]

demonstrated that steric interactions are not unneglectable if the surfaces of the particles are functionalized. Yin et al. [18] found that the interfacial forces predicted by xDLVO approach appeared to be more consistent to the force curves measured by the atomic force microscopy, especially in strongly hydrophilic systems. Trinh et al. [31] and Tanudjaja and Chew [32] applied xDLVO models to predict membrane fouling in organic liquids. Therefore, extended DLVO theory (xDLVO) with all possible interactions should be applied[29, 30, 33, 34].

If the DLVO/ xDLVO predict the total interaction to be strong attractive energy, the particles will deposit on the surface of the membrane. No further detachment will happen for this case. If the total interaction is repulsion, it is most likely that most of the particles will not be captured by the membrane. If the interaction energy is shallow attractive or repulsion, detachment also needs to be considered. However, the possibility of the particles detached from the membrane is also not well studied. Lee et al. [24] considered an additional hydrodynamic force that can induce the detachment of colloids from the membrane. However, hydrodynamic force usually applies to bigger particles [35]. For particles less than 10 nm, thermal rebound (kinetic energy) plays the most important role. The Maxwell-Boltzmann equation, which forms the basis of the kinetic theory of gases, defines the distribution of speeds for a particle at a certain temperature. The area under the distribution curve represents the total number of the particles. Hahn and O'Melia [36] used Maxwell approach to estimate particle collision efficiencies. Although there are several other methods to predict possibility of particle deposition, such as Monte Carlo model [37-39], three-dimensional particle tracking model [40] and dual deposition model [41], Maxwell approach is considered as the most computer cost-effective and direct method. In addition, Shen et al. [42] found that Maxwell model provides much more accurate estimations of collision efficiencies for the small colloid. However, 1.5 orders of magnitude deviation in estimation collision efficiencies

for larger particles. Therefore, more studies are needed to further validate the model in predicting the detachment.
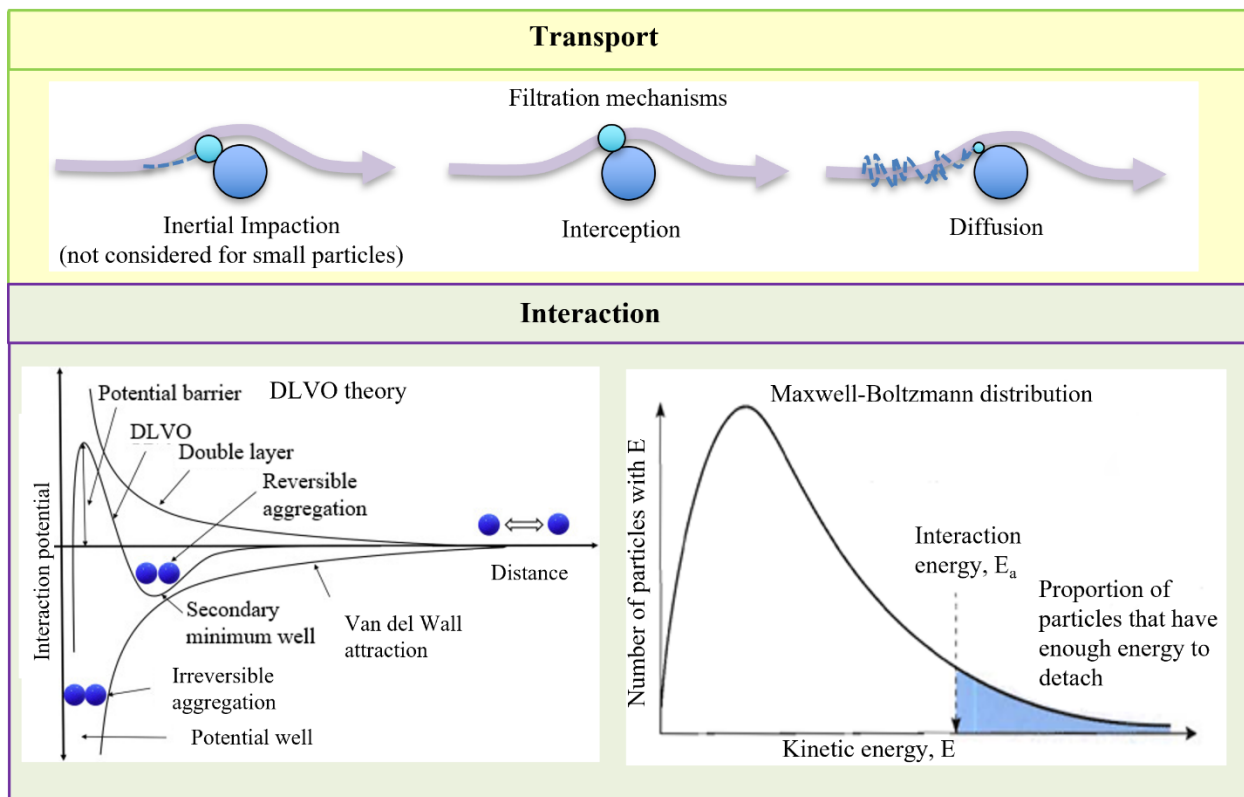
Figure 1.3 Theories to explain deposition of colloidal particles. Reproduced from Ref [25] with permission from ScienceDirect

Literatures discussed the accuracy about DLVO/xDLVO theories are commonly seen, but limited studies reported applying all the theoretical models to explain filtration phenomenon [24]. And to our best knowledge, there is no study investigated the appropriate models for non-aqueous system for particles down to 2 nm.

1.4 Machine learning Techniques

ML techniques are generally categorized into 4 groups: supervised learning, unsupervised learning, semi-supervised learning, and reinforced learning [43]. Unsupervised learning or semi-supervised learning is very useful when user does not know what to extract from the data [44]. Reinforced learning can greatly improve the learning performance when a small amount of labelled data is provided [45]. For UF problems, the learning goals are usually known and the training data can be obtained, so supervised learning is the most commonly used algorithm [46-48].

Among the supervised algorithms, ANN model with different algorithms, including feedforward neural network [49], radial basis function (RBF) [50-52], self-organizing map (SOM) [53], recurrent neural network (RNN) [54], convolutional neural network (CNN) [55], Hybrid neural network [56]etc. (Fig.1.4), have been widely applied to UF processes. Bowen et al. [57, 58] successfully applied BP-ANN to predict membrane fouling during ultrafiltration and microfiltration of proteins and colloids. Zhao et al. [59] developed BP-ANN and RBF-ANN models to predict permeate water total dissolved solids (TDS,) and showed that the ANN models were more accurate than the traditional diffusion based models. Alizadeh and Kavianpour [60] developed wavelet ANN to predict water quality. Curcio et al. [61] used a classic ANN for prediction and control of flux decline in a cross-flow membrane process. However, the accuracy of an ANN prediction is greatly affected by the ANN structure, which depends on the task to be performed. Therefore, appropriate ANN models for our cases are still needed to be developed.
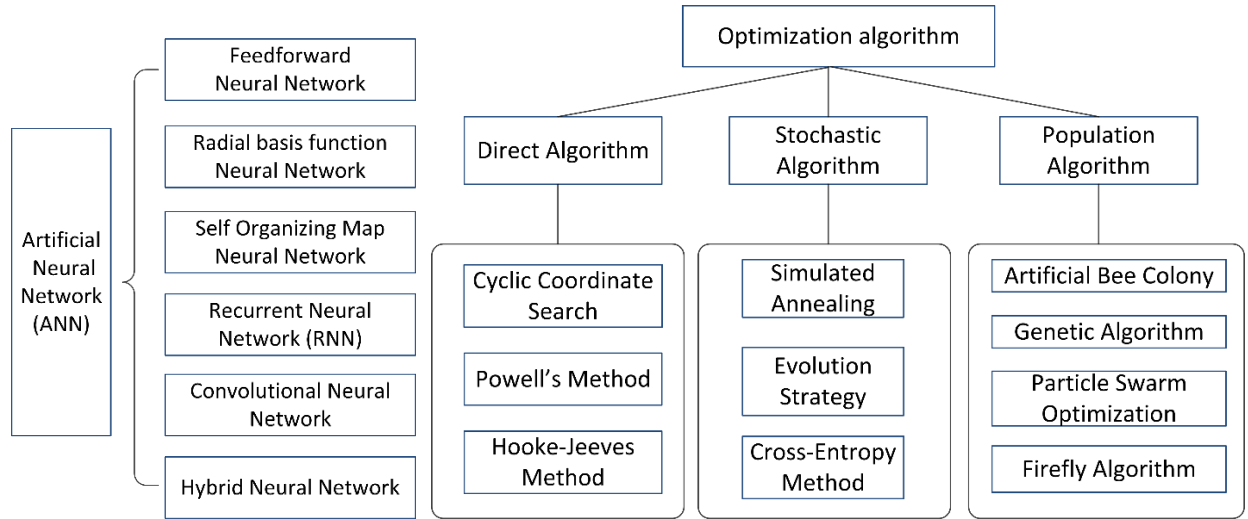
Figure 1.4 State-of-the-art artificial neural networks and optimization algorithms

After running the ANN models, predication results can be provided. To further optimize the results, an optimization method needs to be determined. In general, optimization algorithm includes direct algorithm, stochastic algorithm, and population algorithm (Fig. 1.4) [62-64]. Among these algorithms, population algorithm has advantages over the other algorithms [65, 66]. It has been reported that population algorithms have a high probability of converging to the optimal solution as they explore a wide search space and maintain a diverse population of solutions, and it is highly scalable and can handle problems with a large number of variables and constraints. In addition, population algorithms are robust to changes in problem parameters and constraints, making them suitable for dynamic environments [67]. Moreover, population algorithms strike a balance between exploration and exploitation, which enables them to avoid getting stuck in local optima and discover new promising solutions. Therefore, this research chose this algorithm to perform the optimization. In this category, PSO is considered as the most promising method.

PSO is an optimization algorithm that can use a complex, multi-variable cost function to predict the inputs at the extrema value [68, 69]. In PSO, the particles, or output of different input

combinations, are randomly distributed in the initial state and move according to a set of rules, including direction and velocity, based on reported results of the previous move [70-72]. After iterations, all particles are likely to fall into the global extrema, and the value at that point would be reported alongside the parameters of the particles, offering a combination of input and output at the global extrema value. The number of particles is determined manually. If the number of particles is small, there is a chance that all particles will eventually fall into a local extremum. To avoid this from happening, results with various number of particles should be tested to select the best balance between the computing complexity and the accuracy of the model. For the applications on membrane filtration, PSO model were mostly used to tune the hyper parameters in ANN models. Fetimi et al. [70] applied PSO to optimize the ANN parameters for better predicting the removal of the cationic dye safranin-O from an aqueous solution. Yusuf et al. [73] utilized three different PSO models to train the neural network and found that the combined model could predict the dynamic behavior of filtration process. PSO was also proved to be a good tool in tuning proportional integral derivative (PID) controller in RO system [74]. However, there is a scarcity of literature that utilizes PSO to enhance the performance of UF although it is a very promising method.

1.5 Objectives and Arrangement of the Dissertation

Based on the review for the ultrafiltration shown from section 1.1-1.4, it is very necessary to develop sustainable filtration system and understand its performance from experimental and theoretical aspects. Machine learning technique should also be utilized to facilitate researchers or engineers to choose filtration conditions that can have high filtration performance. Therefore, there are three objectives in my study.

To begin with, measuring particles down to 1.7 nm in liquid is a great challenge so far [7, 8]. The current available methods are either having high requirements for the sample (DLS, NTA, ICP-MS) [20, 22] or time consuming and cost-ineffective (TEM/SEM, ICP-MS) [21, 22]. In addition, no study has found measuring retention efficiencies for particles down to 1.7 nm in IPA. Therefore, it is very necessary to build a new measuring system that can effectively and accurately measure particle characterizations in IPA. In chapter 2, a measurement method for characterizing particles down to 2.8 nm in water and IPA was developed.

In addition, the theoretical models to explain the phenomena in liquid filtration are very complicated. As particles will experience transportation, interaction (deposition) and detachment, three corresponding sets of models should be considered [24]. In general, air filtration models can elucidate the particle transportation very well. However, DLVO/xDLVO models used to describe the interactions between particles and membranes still have noticeable discrepancies when applied to membrane filtration especially in non-aqueous system [18, 31, 32]. Moreover, there are limited studies discussed the detachment [24, 42]. One of the possible reasons is that particles can usually tightly deposit on the surface of the membrane if the capture mechanism is sieving. However, our research is intending to use large pore size membranes to capture small particles to achieve energy conversation. Thus, the detachment is likely to occur and the models that can predict the

27

detachment are also needed to be discussed. Therefore, chapter 3 elucidated the models developed for the filtration in IPA with small NPs.

Lastly, it has been demonstrated that ANNs are effective methods to model non-linear multifactor problems. Successful applications include predicting membrane fouling [57, 58], calculating of permeate flux decline [59], and optimizing membrane fabrication [75]. An essential factor that determines the predict accuracy of the models is matching of ANN architecture to the target [76]. For our research, it is expected to predict the retention efficiency when different operation conditions are given, such as different membranes and particles. An appropriate model for this purpose has not been developed yet. In addition to prediction, it is very useful to provide the optimized operation condition that the UF can have high retention efficiency but low energy consumption. Therefore, in Chapter 4, ANN and PSO models were built and their performances were evaluated. These models can help the operators to better understand the performance of the filtration system and choose the best operation conditions.

Chapter 2. Experimental retentions of sub-10 nm colloidal nanoparticles by large-pore ultrafiltration membranes in isopropanol and water

Abstract

Effective removal of small colloidal nanoparticles (NPs, e.g., < 20 nm), including rigid particles, macromolecules, organics, viruses, antibiotics, hormones, etc., by dead-end filtration, is very important in drinking water, chemical, biopharmaceutical, and semiconductor factories. Most existing operations focused on sieving mechanism-based filtration with small-pore membranes (e.g., < 20 nm) to capture these tiny NPs, which unfortunately leads to high energy consumption. This study proposed an emerging method that is to use large pore membranes (i.e., ~100 nm) to capture NPs down to 2.8 nm. The ultimate goal is to address the grand challenge presented in the United Nations Sustainable Development Goal 12 on energy saving. To capture (or adhere) small NPs by large-pore membranes, the surface electrostatic interactions between NP and membrane should be considered in addition to the sieving mechanism. To examine the feasibility of the proposed method, the retention efficiency of ~100 nm rated polyvinylidene fluoride (PVDF), polytetrafluoroethylene (PTFE), and polycarbonate track-etched (PCTE) (as a model filter) membranes against 2.8 nm ZnS quantum dot (QD), 5 and 10 nm Au and 100 nm PSL in water and isopropanol (IPA) (a representative organic solvent) were studied experimentally. The electrospray-scanning mobility particle sizer (ES-SMPS) was extended to measure the size distribution of these nanosized colloids before and after the membrane to determine the retention efficiency in IPA. Results showed that ES-SMPS system successfully measured particles down to 2.8 nm in water and IPA and the requirement for the concentration limit was as low as 1×10^7 particles/mL for 5 nm Au NP and 5×10^8 particles/mL for 2.8 nm ZnS QDs.

2.1 Introduction

Dead end ultrafiltration (UF, membrane pore sizes between 10~100 nm) and nanofiltration (NF, membrane pore sizes between 1~10 nm) are pressure-driven membrane separation technologies widely applied in food [77], biomedical [78], biopharmaceutical [79], chemical [80], drinking water [81], wastewater [82], and semiconductor industries [14, 19, 83]. For example, the biopharmaceutical industry removes viruses as small as 20 nm by NF in the production of mammalian derived biotherapeutics [79]. Water and wastewater plants need to filter out colloidal particles smaller than 20 nm (~1-20 nm), such as amino acids, antibiotics, and hormones [82]. In semiconductor fabrication plants (Fabs), which manufacture 10 nm or larger node chips, UF is typically used to remove particles in process liquids, including massively used ultrapure water (UPW) and isopropanol (IPA) [3, 9]. However, the critical particle size, the diameter above which a liquid-borne particle becomes a "killer defect" affecting the functionality of the device, is currently reduced to as small as 3 nm in state-of-the-art 3 and 5 nm node Fabs[84]. Therefore, NF membranes are used instead to remove these tiny nanoparticles (NPs) by the sieving mechanism. However, NF is operated at lower flux and higher back pressure of 1 to 20 bars compared to UF, which leads to the total energy consumption of ~30 gigawatt-hours a year for operating the NF in a typical 3 nm Fab [5, 6].

To address the grand challenge presented in the United Nations Sustainable Development Goal 12 which intends to reduce the ecological footprint by changing the way of producing and consuming goods and resources, it is desirable to use UF membranes to remove sub-20 nm NPs (particle to pore diameter ratio, PPDR<<1) if the retention can be improved to be as high as that of NF. With UF, the flux rate can also be increased to shorten the manufacturing time. To capture small NPs by large pore membranes when the sieving mechanism is diminished, the collection will

rely on electrostatic and van der Waal attractions, thus the surface interactions between NP and membrane should be considered. Chen et al. [7] and Lee et al. [8] reported that retention efficiencies can reach 40-50% when challenging 50 and 100 nm rated polycarbonate track-etched (PCTE) membranes with 1.7 nm NPs (PPDR=0.017-0.034) due to overall negative interaction energy. However, their filtrations were only performed in the aqueous system, besides, no theoretical results for particles smaller than 60 nm were shown.

IPA is a representative organic solvent and one of the major chemicals used in silicon chip fabrications [3]. Different from aqueous solutions, IPA is a slightly polar organic solvent that can change the performance of UF from the surface electrostatic interactions. Park et al. [17] showed that adding IPA to water changes the electrokinetic (e.g., dielectric constant and zeta potential) and interfacial characterization of the solution (e.g., viscosity). Yin et al. [18] conducted UF in different organic solvents and found that the zeta potentials of SiO_2 particles and polyacrylonitrile membranes became less negative as the dielectric constant of the solvent increased. Li et al. [85] and Kochan et al. [86] found that the IPA increased the permeability of the polymeric membranes. These changes affect the physicochemical interactions between the colloids and membranes, which are the main filtration mechanisms for UF with PPDR<<1, and thus influence the performance of the UF. However, there are very limited studies that have reported UF for small NPs conducted in IPA. Tsuzuki [83] and Takakura and Tsuzuki [19] did measure the retention of 10 and 30 nm NPs in IPA and sulfuric acid, but the influence of liquid on the surface interaction and retention efficiency was not studied because the major mechanism of their UF was sieving (PPDR>1).

To study UF, especially in IPA for such small NPs, an appropriate and efficient measurement method needs to be developed. There are seven measurement technologies for sizing and counting

colloidal particles, including liquid particle counter (LPC) [87], dynamic light scattering (DLS) [88], nanoparticle tracking analysis (NTA)[89], scanning electron microscopy (SEM) or transmission electron microscopy (TEM) [21, 90], ultraviolet-visible spectroscopy (UV/vis) [91-93], inductively coupled plasma-mass spectrometry (ICP-MS) [22, 94], and electrospray-scanning mobility particle sizer (ES-SMPS) [22]. Among these methods, ES-SMPS is a very promising method to measure particles in the liquid. Unlike other measurement methods which have general issues of sizing accuracies and detection limitations for sub-20 nm NPs, ES-SMPS has a detection capability of NPs down to 1.1 nm (using Nano Enhancer 3757, TSI Inc., Shoreview, MN), low interference, particle material independent feature, fast and nearly real-time registration, relatively low sample concentration requirement (i.e., 1 x 10^7 particles/mL, ~13 ng/L or ~13 ppt for 5 nm Au NP and 5 x 10^8 particles/mL, ~23 ppt for 2.8 nm ZnS QDs), and economically efficient. However, a limitation is that a stable Taylor Cone needs to be formed at the tip of the capillary for the ES to successfully aerosolize particles, which limits the application to liquids with an appropriate conductivity and viscosity [23, 95]. No study has successfully applied the ES-SMPS system to high-concentration IPA, to our best knowledge.

Therefore, the objective of this study is to investigate a reliable method to measure the retention efficiency of colloids down to 2.8 nm in IPA solution for large pore membranes.

2.2 Methods

2.2.1. Challenging particles and solutions

To investigate the mechanisms of retention efficiency of different NPs in UFs, this study used 2.8 nm ZnS quantum dots (QDs), 5 and 10 nm Au NPs and 100 nm PSL as the challenging particles. The ZnS QDs were synthesized according to Komada et al. [96] and Segets et al. [97]. The mean number weighted particle size was 2.8 nm by SMPS and TEM (refer to SI D in Supporting Information). The ZnS QD powder was dispersed in Milli-Q water (EMD Millipore Corp., Billerica, MA) with a concentration of 2 µg/mL. The original concentration of the ZnS suspension was 4.2×10^{13} particles/mL based on a density of 4.09 g/cm^3 of ZnS QDs. The ZnS suspension was ultrasonicated for 10 min and then diluted 500 times with IPA (99.5% electronic grade solution, Thermo Fisher Scientific Inc. Waltham, MA) as the challenging suspension.

For the Au NPs, both the 5 nm Au (Nanopartz Inc., Loveland, CO, USA) and 10 nm Au NPs (Ted Pella Inc., Redding, CA, USA) are stabilized by tannic acid. The original concentrations were provided by the manufacturers with 4.76 x 10^{13} p/mL and 1.47 x 10^{12} p/mL, respectively. The 5 nm Au NPs were diluted 500 times while the 10 nm Au NPs were diluted 100 times by IPA. The 100 nm PSL particles were purchased from Thermo Fisher Scientific (Thermo Fisher Scientific Inc. Waltham, MA). Taking the density of 1.05 g/cm^3 and the concentration of 1%, the original concentration of PSL particles was 1.8 x 10^{13} p/mL. Approximately 500 times dilution was prepared as upstream suspension.

Based on 100-500 times dilutions by the 99.5% IPA for these colloidal suspensions, the challenging suspensions remained at concentrations of IPA higher than 98-99%. Thus, the liquid system of the current UF was considered to be pure IPA in the theoretical modeling. For the filtrations under aqueous conditions, challenging particles were suspended and diluted in Milli-Q

water. The zeta potentials for all the NPs in IPA and water were measured by a Zetasizer Nano ZS (Malvern Instruments, Malvern, UK). The measurement conditions were the same to the filtration experiments. The summary of the particle information is listed in Table 2.1.

Table 2.1. Summary of the nanoparticle characterizations

Nanoparticles	Size (nm)	Zeta potential (mV)		Upstream concentration (p/mL)
		IPA	Water	
ZnS	2.8	-0.7	-15	8.5×10^{10}
Au	5	-1.0	-31	9.5×10^{10}
Au	10	-2.1	-32	1.5×10^{10}
PSL	100	-*	-	3.6×10^{10}

* zeta potentials for PSL were not measured as the main removal mechanism for the 100 nm PSL was sieving.

2.2.2 Membranes

The membranes examined in this study include a PTFE (W.L. Gore & Associates Inc., Newark, DE), a PVDF (EMD Millipore Inc., Darmstadt, Germany), and a PCTE (GE Healthcare Biosciences, Pittsburgh, PA) membrane and their information is summarized in Table 2.2. The pore sizes for the PVDF and PCTE are both 100 nm while that of the PTFE is 130 nm. Therefore, the PPDRs were all less than 0.1, except for the 100 nm PSL. The use of the PCTE as the model filter was due to its relatively simple structure and frequently studied. The use of PSL was intended to show the dominance of the sieving mechanism compared with other UFs under small PPDRs. The PTFE and PVDF are fibrous-like and sponge-like, respectively, and PCTE is a capillary tube membrane. The PTFE was modified to be positively charged while PVDF and PCTE were kept being inherently negatively charged. The zeta potentials were measured by a surface zeta potential cell (ZEN1020, Malvern Instruments, Malvern, UK). Water or IPA were added to the cuvette to make the measuring conditions as close as the filtration conditions. Results are shown in Table 2.2.

Table 2.2. Summary of membrane information

Membrane	Material	Pore size (nm)	Zeta potential (mV)	
			IPA	Water
PCTE	Polycarbonate track-etched (Hydrophilic)	100	-7.1	-11.0
PTFE	Polytetrafluoroethylene (Hydrophilic)	130	7.0	14.0
PVDF	Polyvinylidene fluoride (Hydrophilic)	100	-8.0	-12.2

2.2.3. Experimental systems and retention efficiency measurement

A peristaltic pump (Model 77252-72, Masterflex L/S, Radnor, PA), as shown in Fig. 2.1, was applied to run the UF. The filter holder is a 47 mm diameter metal holder (Toyo Roshi Kaisha Ltd., Tochigi, Japan). To study the effect of filtration velocity on filtration retention efficiency, two flow fluxes of 1.8 and 10.8 mL/min (~0.0018 and 0.01 cm/s) were applied. The influents were prepared to be 50 mL to ensure the liquid fills the entire tube when performing the UF. About 5 mL effluent was collected in consideration of the total feed less than a monolayer of NP deposition on the membranes. A transmission electron microscopy (TEM, JEM-F200, Tokyo, Japan) was used to confirm the sizes and deposition of the 2.8 nm ZnS QDs and 5 nm Au NPs on UF membranes.

In this study, the ES-SMPS (TSI model 3480, 3085, and 3776, TSI Inc., Shoreview, MN), as shown in Fig. 2.1, was used to measure the upstream and downstream particle concentration of the membrane. The chamber pressure was 4 psi. The applied voltages for IPA and water were from 2.2-2.8 kV and 3.0-3.3 kV, respectively. The aerosol flow through the DMA (or nano-DMA) was 1.5 L/min.

The ES generates particles based on the electrostatic separation of the highly charged droplets containing particles. Conductive solutions of colloids were placed in a pressure chamber and then delivered to the end of a capillary (0.04 mm inner diameter and 24 cm in length, TSI Inc., Shoreview, MN). An electrical field was exerted at the exit of the capillary tube, which induced a surface charge on the liquid. By adjusting the voltage, a cone-jet mode was formed, and fine-charged droplets containing the NPs were sprayed out. The liquid from the droplet evaporated in the ionization chamber and airborne NPs remained. The NPs were then introduced into SMPS for particle size and concentration measurement. To obtain the colloidal particle concentration in the liquid before and after the filtration, the correlation between prepared colloidal concentration and aerosolized particle concentration by ES-SMPS should be built (results are shown in Fig. 2.5 in section 2.3.1). Once the relationship is determined, the retention efficiency, E_r, can be calculated as:

$$E_r = 1 - \frac{C_{inf}}{C_{eff}} \tag{2.1}$$

where C_{inf} is the particle concentration in the influent, #/mL, and C_{eff} is the particle concentration in the effluent, #/mL.
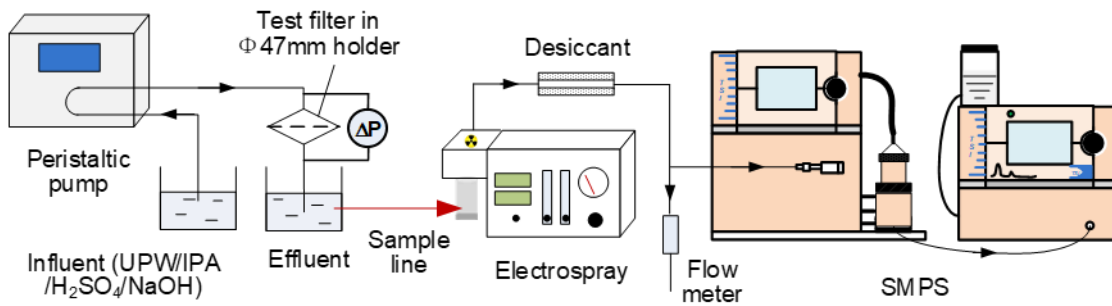
Figure 2.1. Schematic diagram of the ultrafiltration colloids measuring system.

2.3 Results and Discussions

2.3.1. Measuring colloidal particles in IPA using ES-SMPS

For the electrospray, the presence of salts or surfactants typically added to stabilize the colloid, can result in the formation of salt particles during evaporation and then interfere with the SMPS measurement. To avoid interference with seeding particles in the suspension, the droplet size needs to be controlled by adjusting the chamber pressure or the conductivity of the solution to separate the residues from the seeding particles [22, 95] As the presence of high concentration of IPA significantly decreased the conductivity of the suspension, which could cause an instability (i.e., agglomeration) of the colloids, only the chamber pressure was adjusted to separate residues from seeding particles. For the colloids used in our study, ZnS does not have residues, but Au and PSL NP suspensions had residues due to the use of stabilizers. The SMPS measurement results of 10 nm Au and 2.8 nm ZnS NPs are shown in Fig. 2.2 as examples to confirm the separation and size of seeding particles.

Figs. 2.2 (a-c) show that the size distribution of the seeding particles remained (peaking at 14.9 nm) while the distribution of the residues changed when different chamber pressures were applied. It is seen the best operation condition was 4 psi because the size distributions could be totally separated from the residues and the spraying was most stable (not shown). The reason for seeing the peak value of 14.9 nm instead of 10 nm as provided by the vendor was due to the tannic acid cap and the attachments of impurities and surfactants during the evaporation process. Similarly, the size of the 5 nm Au NPs was measured as 7.5 nm. There was no residue effect for the 2.8 nm ZnS QDs (Fig. 2.2d) as no stabilizer was used. The effect was negligible for the PSL due to its large size. To approve the size, TEM images of 2.8 nm NP from the upstream suspension

and 5 nm NPs collected on the PCTE were shown in Fig. 2.3. The images show that the sizes of the 2.8 and 5 nm NPs were approximately 2.8±0.2 and 7.5±1 nm, respectively.
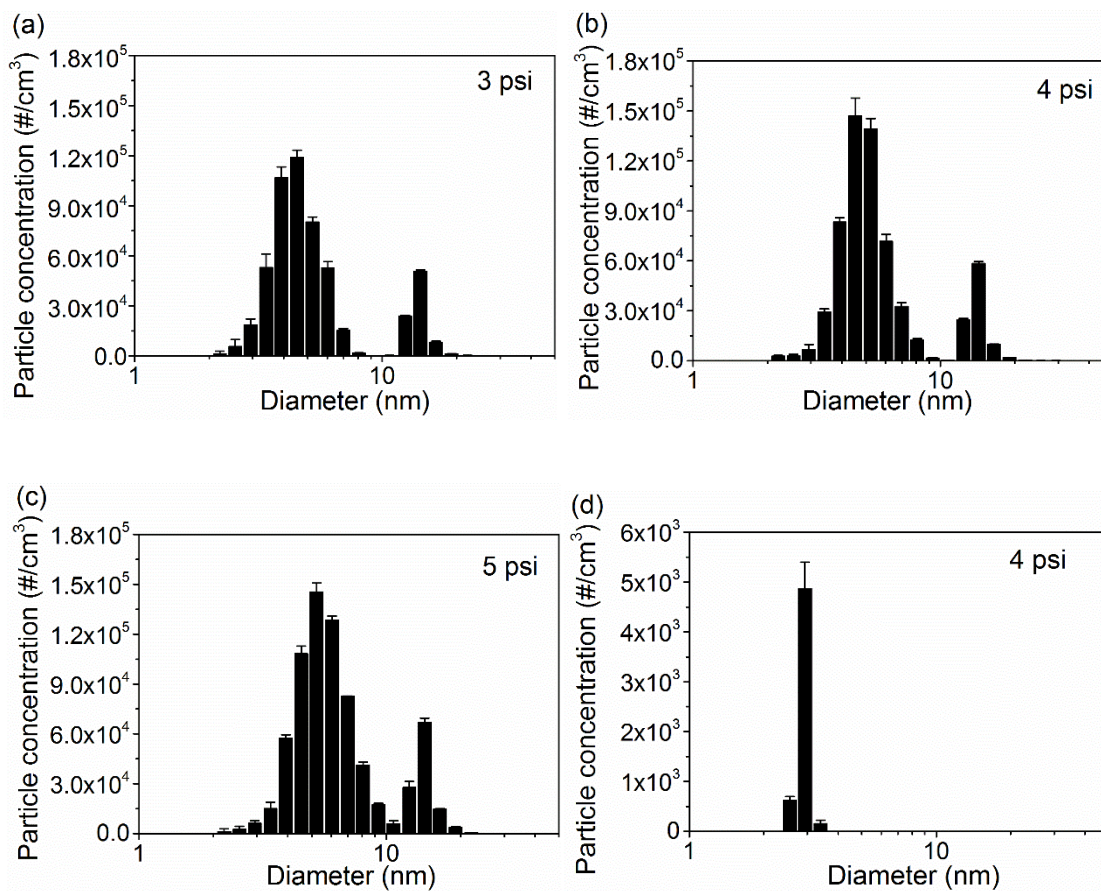
Figure 2.2. Particle size distribution for 10 nm Au NPs under: (a) 3, (b) 4 and (c) 5 psi, and 2.8 nm ZnS NPs under 4 psi (d).
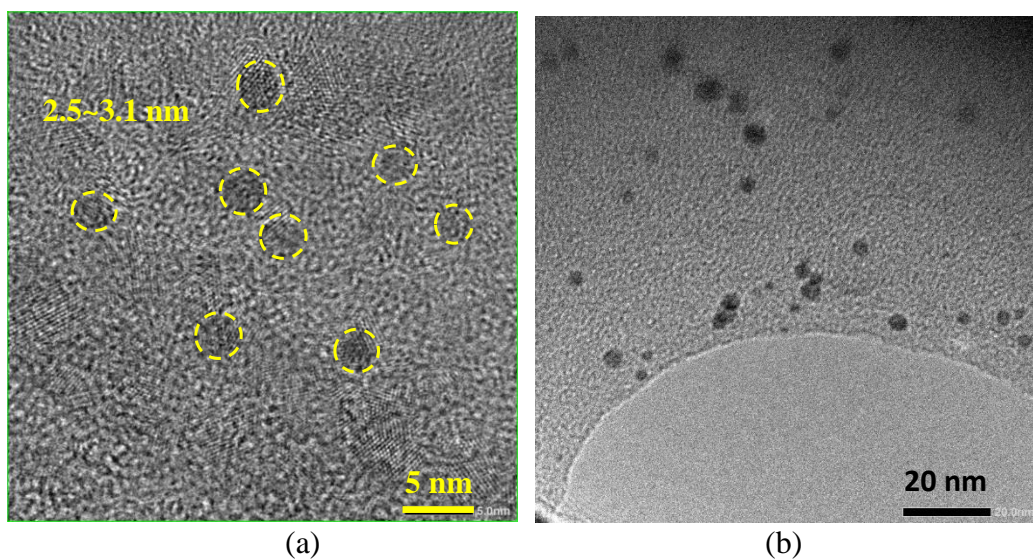
Figure 2.3. TEM images for a) 2.8 nm ZnS QDs and b) 5 nm Au NPs.

Besides, it was confirmed that the sizes of the ZnS before and after passing through the membrane remained unchanged (Figs. 2.4a and 2.4b), therefore, the obtained retention efficiency is reliable. Same results were seen for other three NPs (not shown).

(a)

	Number Particle Size	Diameter Particle Size	Surface Particle Size	Volume Particle Size
Median (nm)	2.88	2.92	3.04	18.7
Mean (nm)	3.00	3.80	7.53	14.7
Geo. Mean (nm)	2.89	3.19	4.95	11.4
Mode (nm)	2.94	2.94	2.94	19.1
Geo. St. Dev.	1.22	1.56	2.36	2.32
Total Conc.	2.18e+03(#/cm³)	6.54e-03(mm/cm³)	7.80e+04(nm²/cm³)	9.78e+04(nm³/cm³)
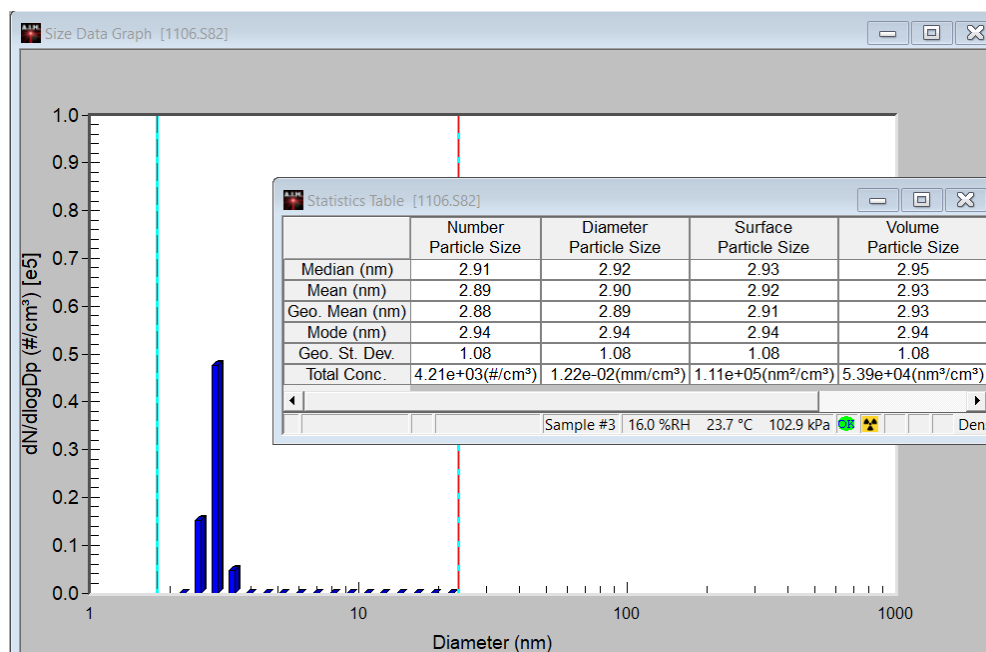
Sample #7   12.1 %RH   24.0 °C   102.8 kPa
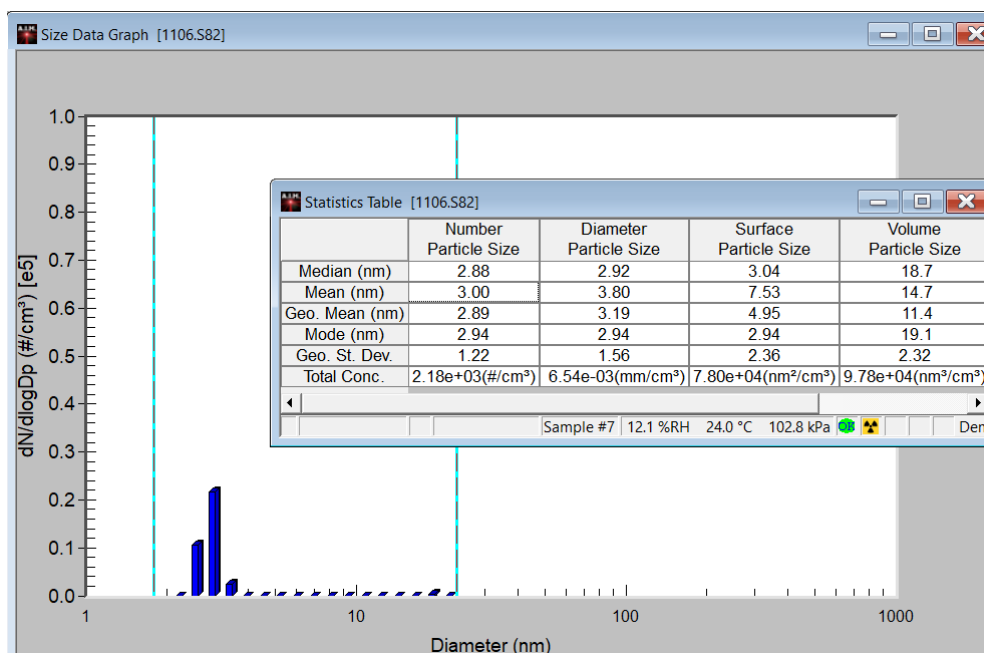
(b)

Figure 2.4. Upstream (a) and downstream (b) size distribution of 2.8 nm ZnS NPs of the membrane.

Fig. 2.5 shows the correlations of normalized concentration of prepared liquid-borne particles and aerosolized particles (by ES-SMPS). All the colloidal suspensions were diluted by 2 to 1000 times from their original concentrations to cover the potential low particle concentrations measured after the filter. It is seen that all the relationships are nearly linear with R-squared values at least 0.97. As the relationships are linear without an interception, the liquid-borne particle concentration can be simply obtained by directly using the measured airborne particle concentration to determine the retention efficiency using Eq. (1). The results also indicated that each droplet sprayed from the electrospray contained one seeding particle in it. Therefore, the particle size and concentration kept the same as the particles were in the liquid.

41
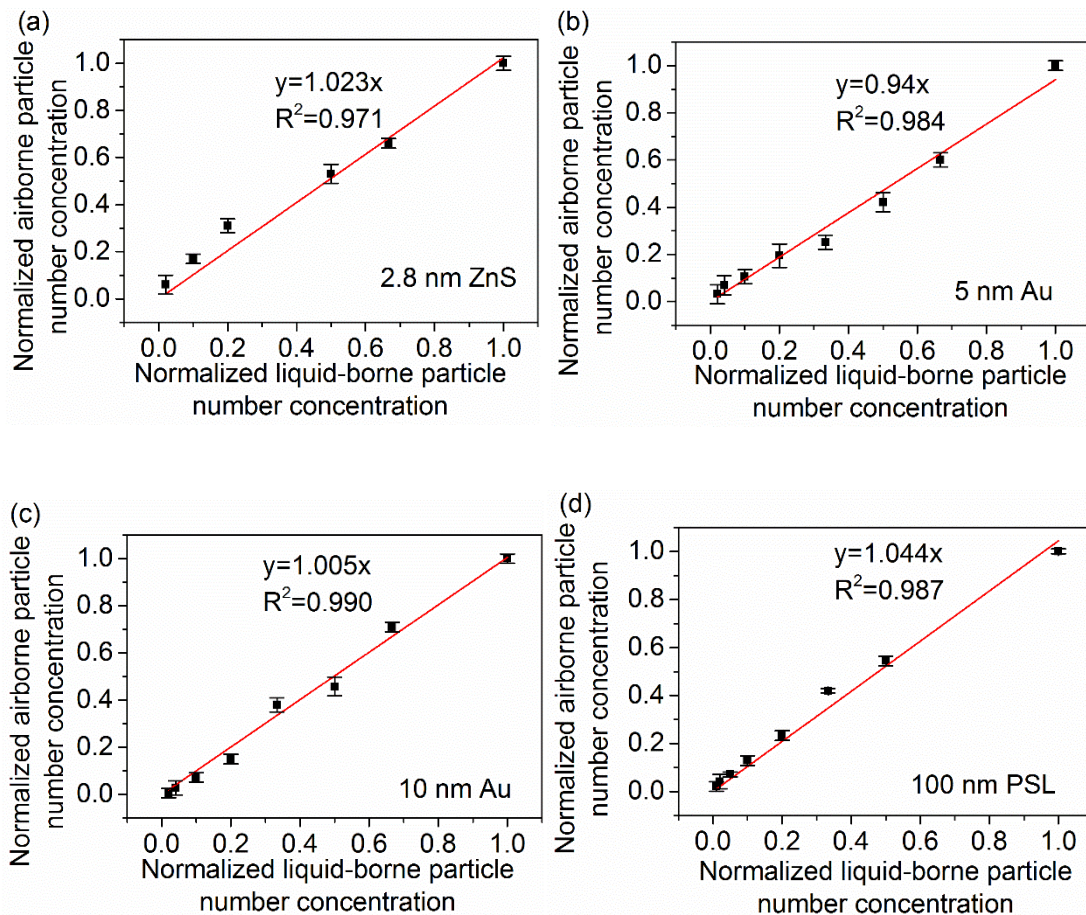
Figure 2.5. Relationship between liquid-borne and aerosolized number concentrations (a) 2.8 nm QDs, (b) 5 nm Au NPs, (c) 10 nm Au NPs, and (d) 100 nm PSL.

The above results show that ES-SMPS is a very reliable and fast method to measure particles down to 2.8 nm in liquid independent on the types of the particles. In addition, the ES-SMPS can detect relatively low colloidal concentration (~10^8 #/mL or ~23 ppt for the 2.8 nm ZnS) and show the results nearly in real-time.

2.3.2. Influence of IPA on NP retention efficiency

In order to understand the effect of liquid on retention efficiency, the retention efficiencies of the three membranes against 10 nm Au NPs (taken 10 nm Au NPs for example) in IPA and

water were summarized in Table 2.3. It should be noted that the structures of the membranes were assumed to be the same after feeding by IPA because of the short filtration time (2-6 minutes) for initial filtration. It is clearly seen that the efficiencies in IPA were higher than that in water regardless the types of the membrane. A theoretical explanation can be found in the next Chapter.

Table 2.3. Retention efficiency for 10 nm Au NPs by different membranes in IPA and water

	Water	IPA
PCTE	0.32±0.052	0.72±0.052
PTFE	0.35±0.035	0.76±0.035
PVDF	0.31±0.041	0.36±0.046

2.3.3 Effects of NP sizes and materials on retention in IPA

It is energy efficient to remove particles using membranes with PPDR<<1 if the retention efficiency is sufficient high. To investigate the filtration performance with PPDR<<1, this study challenged the three membranes with NPs of 2.8, 5 and 10 nm. For comparison purpose, the retention efficiency for 100 nm PSL NPs was also measured.

Table 2.4 listed the experimental retention efficiencies of different sizes NPs by the three membranes in IPA. It is seen the retention of the 100 nm PSL (PPDR ≈ 1) in the three membranes were mainly by sieving as ~100% of efficiency was obtained by the PCTE and PTFE and ~70% for the PVDF. The ~100% retention by PCTE was due to its majority of ~100 nm pores. For fibrous- and sponge-like membranes, i.e., PTFE and PVDF, there are many pores larger than their rated pore sizes. The presence of electrical attraction in PTFE (positively charged) facilitated the ~100% retention, however, the retention was only ~70% for the PVDF due to the lack of electrical attraction [7].

The sieving mechanism can be largely reduced when the particle size is very small, i.e., 2.8 nm (PPDR=0.028) and 5 nm (PPDR=0.05), and their efficiencies are expected to be extremely low, i.e., < 5% for PPDR of 0.028 and < 10% for PPDR of 0.05. Surprisingly, the experimental efficiencies reached up to 35% (PVDF) for the 2.8 nm ZnS QDs and 67% (PCTE) for the 5 nm Au NPs in IPA. It is believed that diffusion largely enhanced the transport coefficient and contributed to these efficiencies. A lower efficiency, reduced to 23% (PVDF vs. 2.8 nm ZnS) and 25% (PCTE vs. 5 nm Au), respectively, under ~10 times of higher flux (0.01 cm/s) proved the assumption. The diffusion efficiencies (or transport coefficients) based on the filtration models were higher than 85% for the 2.8 and 5 nm NPs in all three membranes. However, the experimental retentions yet showed lower values, which indicated that interactions between particles and membranes should be considered for small PPDR UF (see chapter 3).

Table 2.4. Retention efficiencies of different sizes NPs by the three membranes in IPA

Particles	PCTE		PTFE		PVDF	
	Low flux	High flux	Low flux	High flux	Low flux	High flux
2.8 nm ZnS	0.31±0.047	0.13±0.043	0.29±0.055	0.12±0.006	0.35±0.012	0.23±0.025
5 nm Au	0.67±0.039	0.25±0.022	0.56±0.031	0.24±0.024	0.24±0.052	0.07±0.039
10 nm Au	0.72±0.052	0.53±0.006	0.76±0.035	0.59±0.013	0.36±0.046	0.15±0.041
100 nm PSL	0.99±0.006	0.99±0.004	0.99±0.015	0.98±0.021	0.74±0.025	0.60±0.005

2.4 Conclusions

This study experimentally investigated the retention of 2.8, 5 and 10 nm nanoparticles in Milli-Q water and IPA by large-pored ultrafiltration (UF) membranes, including 100 nm rated PCTE and PVDF and 130 nm rated PTFE. The ES-SMPS successfully determined the retention

efficiency of NPs down to 2.8 nm (confirmed by TEM imaging) under an extremely low challenging concentration of $5x10^8$ p/mL or ~23 ppt.

It was found that the retention efficiencies in IPA were higher than that of water for all three membranes. The PTFE with 130 nm pore size had a comparable or greater efficiency for all four sizes of NPs than the PCTE. Unexpected but surprisingly high retentions were seen, up to 30, 60 and 75% for 2.8, 5 and 10 nm NPs, respectively, by the 130 nm rated PTFE. This indicated that UF under small PPDR (0.022~0.077) is feasible, and thereby the operation energy can be greatly reduced for future NF and UF related industries.

Chapter 3. Theoretical development for calculating retentions of sub-10 nm colloidal nanoparticles by large-pore ultrafiltration membranes in isopropanol and water

Abstract:

Ultrafiltration (UF) of very small particles in non-aqueous system is widely applied in many chemical, biopharmaceutical, food and manufacturing industries and it is very essential to build theoretical models to understand its performance. This study combined the hydrodynamic particle transport, extended Derjaguin-Landau-Verwey-Overbeek (xDLVO), and Maxwell models to calculate the NP retention. To verify the model results, the retention efficiencies of ~100 nm rated polyvinylidene fluoride (PVDF), polytetrafluoroethylene (PTFE), and polycarbonate track-etched (PCTE) (as a model filter) membranes against 2.8 nm ZnS quantum dot (QD), 5 and 10 nm Au and 100 nm PSL in water and isopropanol (IPA) were obtained using previously developed electrospray-scanning mobility particle sizer (ES-SMPS) method. Results showed that the data agreed with the theoretical model very well, and the NP retentions in IPA were higher than that in water due to a significant change of acid-base interaction from repulsion to attraction. The retention of the 10 nm Au NPs reached ~80% and the 2.8 nm NPs could be attained by ~35% in IPA by the PTFE. This study was the first to show the combined theoretical model can accurately predict the retention of sub-10 nm NPs by different membranes in an organic solvent and water. The model predicts the retention of 5 nm Au NPs can be increased to higher than 99% by increasing the zeta potential of the PTFE about 5 times, thus a sustainable UF cutting significant carbon footprint is foreseeable in near future.

3.1 Introduction

The pressure-driven membrane process is one of important separation processes in wastewater treatment [98-100], oil and petroleum [101], food [102], pharmaceutical [103, 104], biomedical [105], semiconductor [14, 19, 83, 106] etc., There are four main filtration processes, i.e., microfiltration (MF), ultrafiltration (UF), nanofiltration (NF) and reverse osmosis (RO), which are categorized based on the operation pressure (or transmembrane pressure, TMP) [107, 108]. Typically, the TMP for MF, UF, NF and RO are 1-10, 1-10, 10-30 and 35-100 bars, respectively [107]. It can be seen that the NF and RO is high pressure filtration and thus have high energy consumption. In order to achieve sustainable filtration, our previous research proposed to use UF replace NF. Experimental results demonstrated that efficiency could reach as high as ~80% when certain filtration conditions were chosen (Chapter 2). Although the result is very positive and the method is promising, a higher efficiency should be achieved for the proposed method to be applicable in industrial settings. In order to improve the efficiency, theoretical study to reveal the filtration mechanism and influencing factors is very important.

Challenges existed in developing the models that can quantitatively explain the filtration. The theoretical explanation of the UF for NPs down to 2~3 nm in IPA has not been elaborated and validated with experimental data. In liquid filtration, NPs experience two processes to result in the final attach or detach: transport to the vicinity of the membrane, surface interaction with the membrane and possibly detachment from the surface due to high kinetic energy or hydrodynamic drag [109]. Many studies ignored the transport and detachment, and just used Derjaguin-Landau-Verwey-Overbeek (DLVO)/extended DLVO (xDLVO) to explain the deposition of colloids onto the surfaces of porous media [110]. Consequently, their calculation results can only qualitatively agree with the experimental results [90, 91]. To be able to quantitatively predict retention

48

efficiency, filtration and Maxwell models need to be included [24, 42, 111]. In addition, the DLVO/xDLVO models need to be further modified for the non-aqueous system.

The DLVO or extended DLVO (xDLVO) models describe the total interaction energy between particles and collector surfaces as a function of separation distance [109, 110]. DLVO considers the superposition of van der Waals (VDW) and electrical double layer (EDL) interaction while xDLVO model includes additional non-DLVO effects, such as born repulsion and acid-base (AB) interaction compared to the DLVO model [109, 110]. In aqueous media (polar solvent), the xDLVO model with the consideration of AB interaction is usually used due to its higher qualitative agreements with the deposition behavior [28, 110, 111]. However, in organic solvents, which have vastly different properties than water, such as polarity and zeta potentials, the interactions between the colloids and the membranes can vary greatly. Therefore, the contributions of the constitutive interaction terms in the x-DLVO model are not clear. Yin et al. [18] studied the fouling behavior of colloidal particles in organic solvents and found that EDL interaction in apolar solvents was very low, but AB interaction was very important. Tanudjaja and Chew [32] and Trinh et al. [31] also reported that AB interactions are important. However, He et al. [112] stated that AB interaction was negligible due to the apolarity of crude oil. These differences indicate that models used to describe the behavior of colloidal particles in organic solvent systems need to be further studied and validated by experimental data. Moreover, the existing studies about theoretical colloidal particle deposition all focused on particles larger than 60 nm [18, 24, 31, 32, 112, 113]. The deposition behaviors for small NPs (< 10 nm) have not been elucidated.

Therefore, the aim of this study is to develop theoretical models that can quantitatively predict the retention efficiency for small nanoparticles in water and IPA.

3.2 Methods

3.1.1 Experiments

This study used the experimental data from chapter 2. The properties for the 2.8 nm ZnS quantum dot (QD), 5 and 10 nm Au and 100 nm PSL and PCTE, PTFE and PVDF membrane can be found in section 2.2.1 and 2.2.2. The description of the experimental system is shown in section 2.2.3. Electrospray-scanning mobility particle sizer (ES-SMPS) was used to measure the size distribution of these nanosized colloids before and after the membrane to determine the retention efficiency.

3.1.2 Filtration mechanisms

For liquid filtration, the filtration process includes two parts, i.e., transport and interaction (Fig.3.1). The transport is the basic for the filtration and the interaction between the particles and the membrane in boundary layer is essential to determine the efficiency. Transport refers that the particles are approaching the membrane surface. The mechanisms for this stage are similar to air filtration, mainly including interception, impaction, and diffusion (Fig.3.1). For fibrous membranes, single fiber theory can be applied.

For particle transport mechanisms for PTFE and PVDF membrane [114]

Diffusion

$$C_c = 1 + \frac{\lambda}{d}\left[2.34 + 1.05\exp\left(-0.39\frac{d}{\lambda}\right)\right] \qquad (3.1)$$

$$D = \frac{kTC_c}{3\pi\eta d} \qquad (3.2)$$

$$Pe = \frac{d_f U_0}{D} \qquad (3.3)$$

$$E_D = 2 Pe^{-2/3} \qquad (3.4)$$

where C_c is the slip correction factor, λ is the mean free path of the medium; d is the particle

diameter, D is the particle diffusivity, k is Boltzmann constant, T is absolute temperature, η is the

fluid viscosity, Pe is the Peclet number, d_f is the fiber diameter, U_0 is the face velocity; E_D is

the single fiber efficiency due to diffusion.

Interception

$$R = \frac{d_p}{d_f} \qquad (3.5)$$

$$Ku = -\frac{\ln \alpha}{2} - \frac{3}{4} + \alpha - \frac{\alpha^2}{4} \qquad (3.6)$$

$$E_R = \frac{(1-\alpha)R^2}{Ku(1+R)} \qquad (3.7)$$

where R is ratio of particle diameter to fiber diameter Ku is the Kuwabara factor; α is the fiber

solidity, E_R is the single fiber efficiency due to interception.

Total single fiber efficiency

$$E_\Sigma = 1 - (1 - E_D)(1 - E_R) \qquad (3.8)$$

where E_Σ is total single fiber efficiency

The overall filter efficiency

$$E_f = 1 - \exp\left(\frac{-4\alpha E_\Sigma t}{\pi d_f}\right) \tag{3.9}$$

where E_f is the overall filter efficiency for PTFE and PVDF, t is the filter thickness.

For PCTE membranes, the capillary tube model should be used.

Particle t ransport mechanisms for PCTE membrane:

Diffusion on the front surface of the PCTE membrane [115]

$$E_{DS} = 1 - \exp\left\{\frac{-a_1\Psi^{2/3}}{1+(a_1/a_2)\Psi^{7/15}}\right\} \tag{3.10}$$

(a_1 = 4.57-6.46P+4.58P^2, a_2 = 4.5, Ψ = $DP^{1/2}/a_{pore}U$, and $D = kT/6\pi\eta a_x$)

Interception efficiency on pore openings [116]

$$E_R = N_R(2-N_R) \text{ for } N_R < 1 \tag{3.11}$$

$$E_R = 1 \text{ for } N_R \geq 1 \tag{3.12}$$

($N_R = a_x/a_{pore}$)

Diffusion efficiency on pore walls [116, 117]

$$E_{DP} = 1 - 0.819\exp(-3.657N_{DP}) - 0.098\exp(-22.305N_{DP}) - 0.032\exp(-56.95N_{DP})$$
$$- 0.016\exp(-107.6N_{DP}) \text{ for } N_{DP} \geq 0.01 \tag{3.13}$$

$$E_{DP} = 2.56N_{DP}^{2/3} - 1.2N_{DP} - 0.177N_{DP}^{4/3} \text{ for } N_{DP} < 0.01 \tag{3.14}$$

$$\tag{3.15}$$

($N_{DP} = LPD/a_{pore}^2U$)
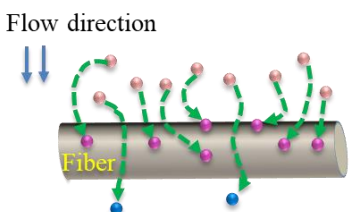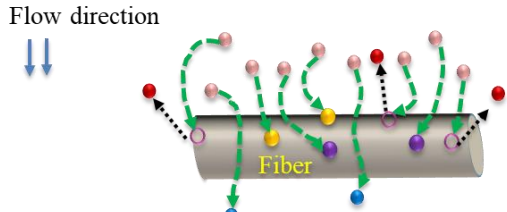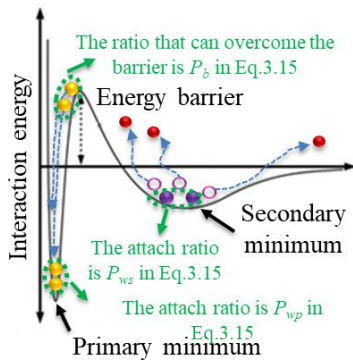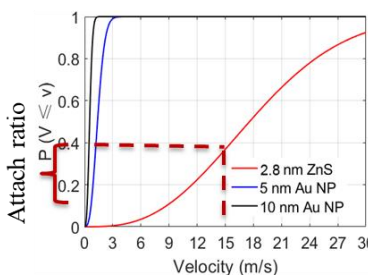
where P [-] is the porosity of the filter, a_{pore} is the pore radius, a_x is the particle radius, L is the thickness of the filter.

The overall filter efficiency

$$E_c = (E_{DS} + E_R) + fE_{DP} \qquad (3.15)$$

Where E_c is the overall filter efficiency for PCTE, f is the fraction of the particles that can pass the surface of the membrane [24].

After the particles are successfully transported to the vicinity of the membrane surface (only a certain fraction), different from air filtration, the surface interaction between the particles and the membrane takes place. The xDLVO theory was used to calculate the total interaction energy (Fig.3.1) (shown in section 3.1.3). The total energy combines particle Brownian kinetic energy (for particles less than 10 nm) determines the attachment/detachment (Fig.3.1). If the total energy is repulsive (positive value), colloidal particles must overcome an energy barrier to attach. The kinetic energy of the particles will determine if the particles can cross over the energy barrier. If the total energy is attractive (negative value), the depth of potential well indicates the strength of the attraction. When the kinetic energy of the particle is higher than the depth of the potential well, detachment can happen.

	Transport	Interaction	
Filtration process	Flow direction • Upstream particles (UP) • Particles reached the fiber surface (The ratio to UP is *E* in Eq.3.15) • Penetrated particles	Flow direction • Attached particles • Detached particles	
	Air filtration models	xDLVO theory	Maxwell models
Calculation models	• Fibrous membranes Single fiber theory [114] $$E_f = 1 - \exp\left(\frac{-4\alpha E_\Sigma t}{\pi d_f}\right)$$ • PCTE membranes Capillary tube model [46-48] $$E_c = (E_{DS} + E_R) + f E_{DP}$$	• Determine the total interaction energy Energy barrier The ratio that can overcome the barrier is P_b in Eq.3.15 Secondary minimum The attach ratio is P_{ws} in Eq.3.15 The attach ratio is P_{wp} in Eq.3.15 Primary minimum	• Compare total interaction energy with particle's kinetic energy. • Determine attach/detach ratio Cumulative Maxwell velocity distribution

* E_f is the overall filter efficiency for PTFE and PVDF, α is the fiber solidity, E_Σ is total single fiber efficiency, t is the filter thickness, d_f is the fiber diameter; E_c is the overall filter efficiency for PCTE, E_{DS} Diffusion on the front surface of the PCTE membrane, E_R is the interception efficiency on pore openings, E_{DP} is Diffusion efficiency on pore walls, f is the fraction of the particles that can pass the surface of the membrane

Figure 3.1. Schematic diagram of the liquid filtration processes and calculation models

Maxwell model describes the velocity distribution of the colloids in the energy well and has been validated to predict the probability of deposition [42]. The Maxwell approach can be applied to calculate the kinetic energy of particles so that the probability of the particles either overcoming the energy barrier or escaping from the potential well can be evaluated. The cumulative velocity distribution of the colloids in the primary or secondary minimum is:

$$f(v) = erf\left(\frac{v}{\sqrt{2}a}\right) - \sqrt{\frac{2}{\pi}}\frac{ve^{-v^2/(2a^2)}}{a} \tag{3.16}$$

where erf is the error function, $a = \sqrt{kT/m}$, m is the particle mass.

Define the dimensionless kinetic energy of the colloid at the primary or secondary minimum as:

$$x^2 = \frac{mv^2}{2kT} = \frac{v^2}{2a^2} \tag{3.17}$$

Therefore, the fraction of colloids that possibly overcome the energy barrier is:

$$P_b = 1 - f(\sqrt{2}ax_b) = 1 - erf(x_b) - \sqrt{\frac{4}{\pi}}x_b e^{-x_b^2} \tag{3.18}$$

The fraction of the colloids that possibly deposit at the primary minimum is:

$$P_{wp} = f(\sqrt{2}ax_{wp}) = erf(x_{wp}) - \sqrt{\frac{4}{\pi}}x_{wp} e^{-x_{wp}^2} \tag{3.19}$$

And the fraction of the colloids that possibly deposit at the secondary minimum is:

$$P_{ws} = f(\sqrt{2}ax_{ws}) = erf(x_{ws}) - \sqrt{\frac{4}{\pi}}x_{ws} e^{-x_{ws}^2} \tag{3.20}$$

The hydrodynamic drag causing the detachment was not considered as it was negligible for sub-10 nm NPs [8].

3.1.3. The xDLVO theory

The DLVO theory expresses total interaction energy between a colloid and a membrane as the summation of VDW and EDL interaction energies. However, the superposition of VDW and

55

the EDL energies gives rise to an infinitely deep primary minimum which is physically unrealistic. To obtain a finite potential at the primary minimum, Elimelech et al., [109] indicated that a short-ranged born repulsion, B, should be incorporated. Ruckenstein and Prieve [118] showed that Born repulsion severely influences the primary minimum and developed a widely used formula. Lee et al., [24] and Fan et al., [111] also their formula and demonstrated that Born repulsion is very important for expressing the value of the primary minimum. In addition to Born repulsion, it has been suggested by van Oss [110] that energy balances performed must also include the AB interaction energy, especially for aqueous systems. Adding B and AB interaction energies to DLVO theory results in the xDLVO theory [110]:

$$V_{total\_Water/IPA} = V_{VDW} + V_{EDL} + V_B + V_{AB} \tag{3.21}$$

where $V_{total\_Water/IPA}$ is the total interaction energy in water or IPA, J, V_{VDW} is the van der Waal interaction energy, J, V_{EDL} is the electrostatic double layer interaction energy, J, V_B is the born repulsion interaction energy, J, V_{AB} is the AB interaction energy, J.

For the van der Waal interaction energy, a sphere-plane Hamaker approximate expression for the retarded VDW energy was used [119]:

$$V_{VDW} = -\frac{Aa}{6h}\left(\frac{1}{1+14h/\lambda}\right) \tag{3.22}$$

where A is the Hamaker constant, a is the radius of the sphere, m, h is the separation distance, m, λ is the wavelength, 100 nm.

The Hamaker constant can be calculated using the following expression for colloids and membrane, 1 and 2, interacting across the liquid, 3 [120]:

$$A_{132} \approx \frac{3}{4}kT\left(\frac{\varepsilon_1 - \varepsilon_3}{\varepsilon_1 + \varepsilon_3}\right)\left(\frac{\varepsilon_2 - \varepsilon_3}{\varepsilon_2 + \varepsilon_3}\right)$$
$$+ \frac{3h_p\nu_e}{8\sqrt{2}} \frac{\left(n_1^2 - n_3^2\right)\left(n_2^2 - n_3^2\right)}{\left(n_1^2 + n_3^2\right)^{1/2}\left(n_2^2 + n_3^2\right)^{1/2}\left\{\left(n_1^2 + n_3^2\right)^{1/2} + \left(n_2^2 + n_3^2\right)^{1/2}\right\}} \quad (3.23)$$

where k is Boltzmann constant, T is the absolute temperature, 298K, kT is 4.11 x 10^{-21} J, ε is

dielectric permittivity, h_p is Plank constant, 6.626 x 10^{-34} J·s, ν_e is electronic absorption frequency,

3 x 10^{15} s^{-1}, n is the refractive index.

For the electrostatic double-layer interaction energy, this study applied the constant potential

approximation method because the potentials in IPA were very low [31, 109]:

$$V_{EDL} = \pi\varepsilon_0\varepsilon_l a\left(2\psi_m\psi_c \ln\left(\frac{1 + e^{-\kappa h}}{1 - e^{-\kappa h}}\right) + (\psi_m^2 + \psi_c^2)\ln\left(1 - e^{-2\kappa h}\right)\right) \quad (3.24)$$

where ε_0 is the relative permittivity of vacuum, 8.854 x 10^{-12} C^2/(J·m), ε_l is the relative

permittivity of IPA or water, 19.92 or 80 at 25 °C, κ is the inverse of Debye length, ψ_m is the

surface potential of the membranes, ψ_c is the surface potential of the colloids. In our study, the

zeta potentials (Table 1 for the colloids and Table 2 for the membranes) were used as

approximations for surface potentials.

For the born repulsion, the sphere-plate born repulsion developed by Ruckenstein and Prieve

[118] is:

$$V_B = \frac{A\sigma_c^6}{7560}\left[\frac{8a + h}{\left(2a + h\right)^7} + \frac{6a - h}{h^7}\right] \quad (3.25)$$

where σ_c is the collision diameter, typically 0.5 nm.

For the AB interaction energy, the expression for the interaction of a membrane and a colloid in an aqueous environment as a function of separation distance is [28, 31]:

$$V_{AB} = 2\pi a \lambda_{AB} \Delta G_{h_0}^{AB} \exp\left(\frac{h_0 - h}{\lambda_{AB}}\right) \tag{3.26}$$

where λ_{AB} is the characteristic decay length of AB interactions in water, whose value is between 0.2 and 1.0 nm [110]. A commonly used value for aqueous system is 0.6 nm [121, 122]. h_0 is the minimum equilibrium cut off distance and is usually assigned a value of 0.158 nm [121, 123]. $\Delta G_{h_0}^{AB}$ is the AB free energy at the minimum distance, which can be determined by [124]:

$$\Delta G_{h_0}^{AB} = 2\sqrt{\gamma_l^+}\left(\sqrt{\gamma_m^-} + \sqrt{\gamma_c^-} - \sqrt{\gamma_l^-}\right) + 2\sqrt{\gamma_l^-}\left(\sqrt{\gamma_m^+} + \sqrt{\gamma_c^+} - \sqrt{\gamma_l^+}\right) - 2\left(\sqrt{\gamma_m^+\gamma_c^-} + \sqrt{\gamma_m^-\gamma_c^+}\right) \tag{3.27}$$

where the subscripts l, m and c represent liquid, membrane and colloid respectively, γ^+ and γ^- are the electron acceptor component and electron donor component of polar AB surface tension. The values for the membranes, colloids and liquids used in our study are listed in Table 3.1.

Table 3.1. Surface tension components for membranes, colloids and liquids.

		γ^+	γ^-
Liquid	Water[a]	25.5	25.5
	IPA	0	0
Membrane	PCTE[b]	0.1	5.8
	PTFE[b]	0	0.9
	PVDF[b]	0	0.1
Colloid	Au NP[c]	0.58	25.7

[a] Data taken from Brant and Childress [28], [b] Data taken from Cornelissen et al. [125], [c] Data taken Sood et al. [126].

58

As IPA is a weak polar solvent, this study assumed it as an apolar solvent. Therefore, the surface tension components are zero for IPA. For colloids, the surface tension decreases significantly as the particle size decreases [127]. This study assumed the surface tension components for 1.7 nm ZnS were negligible.

3.1.4 Total retention efficiency

Considering all three stages in liquid filtration, the total retention (deposition) efficiency, E_T, can be calculated as follows:

$$E_T = EP_b P_{wp} + EP_{ws} \tag{3.28}$$

where E is the transport coefficient calculated based on filtration models [114-117] (Eq.3.1-3.15) as explained in Fig.3.1, P_b is the fraction of the colloids that can overcome the energy barrier if it applies [24, 42] (Eq.3.16-3.20) as explained in Fig.3.1. P_{wp} is the fraction of the colloids that can stably deposit at the primary minimum potential well [24, 42], P_{ws} is the fraction of the colloids that can stably deposit at the secondary minimum potential well if it applies (P_{wp} and P_{ws} are also called collision efficiency, refer to Eq.3.16-3.20) as explained in Fig.3.1. Therefore, when only the primary minimum exists, the total retention efficiency equals to the fraction of particles deposits at the primary minimum. When a secondary minimum potential coexists with the primary minimum, the total retention efficiency equals to the fraction of particles deposits at the secondary minimum and the fraction of particles that overcomes the energy barrier and deposits at the primary minimum.

3.3 Results and Discussions

3.3.1 Retention efficiency in IPA and water

Fig. 3.2 compares the experimental and theoretical efficiencies of the three membranes against 10 nm Au NPs (taken 10 nm Au NPs for example) in IPA and water. It shows that the calculation results agreed with the experimental results except the one for PTFE in water. Theoretical explanations for efficiency on each membrane are as follows.
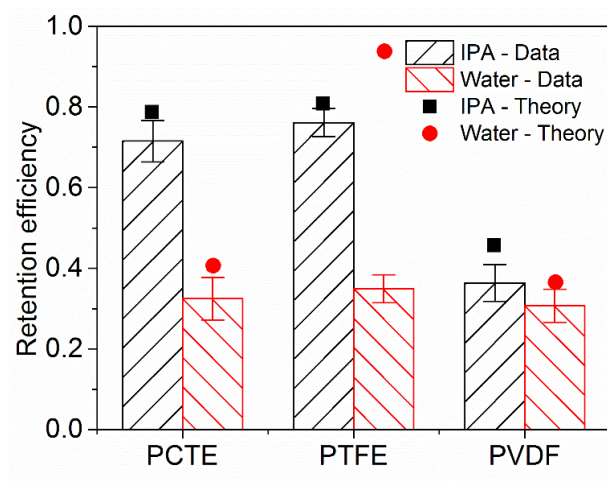
Figure 3.2. Retention efficiency for 10 nm Au NPs by different membranes in IPA and water.

For the PCTE membrane, the transport coefficient of 10 nm Au was 78.8% and 86.7% in IPA and water, respectively. However, due to the interactions between the 10 nm Au and PCTE after they transported to the vicinity of the membrane, the efficiency in IPA could maintain around 70% while that in water dropped significantly to 32%. Fig. 3.3 shows the comparison of xDLVO profiles between IPA and water for the 10 nm Au NPs. It is seen the VDW and AB interactions dominated the total energy. The IPA slightly decreased the VDW interaction energy compared to water (Fig. 3.3a), but totally changed the AB interaction (Fig. 3.3c). It is concluded that the difference of liquids can cause an opposite result of the overall interaction energy (Fig. 3.3d). That is, a deep primary minimum (-41 kT) in IPA and a high barrier (37 kT) in water was obtained. The

deep primary minimum for IPA could completely trap the particles that were transported to the surface of the membrane, and no particles could further detach from the PCTE due to the deep well. Therefore, the retention efficiency in IPA was close to the transport coefficient (calculation from the filtration model) as the collision efficiency was unity (Eq. 3.28).

However, when the UF was performed in water, other than the high energy barrier, a shallow secondary minimum of -1.2 kT existed (Fig. 3.3d) due to the EDL interaction (Fig. 3.3b), which resulted in a long-range attraction interaction. Different from primary minimum for IPA, the collision efficiency at this secondary minimum was less than unity as the attraction energy was very weak (1.2 kT). Based on the Maxwell velocity distribution (refer to Eq.3.16-3.20), 60% of 10 nm Au NPs would have a higher kinetic energy than the secondary minimum energy of 1.2 kT, which means these NPs were capable to escape from the weak attraction by the secondary minimum. Besides, due to the high energy barrier, there were no chances for these NPs to overcome and get deposited. Therefore, the overall retention efficiency was calculated to be ~40% which was in good agreement with the data (Fig. 3.2).
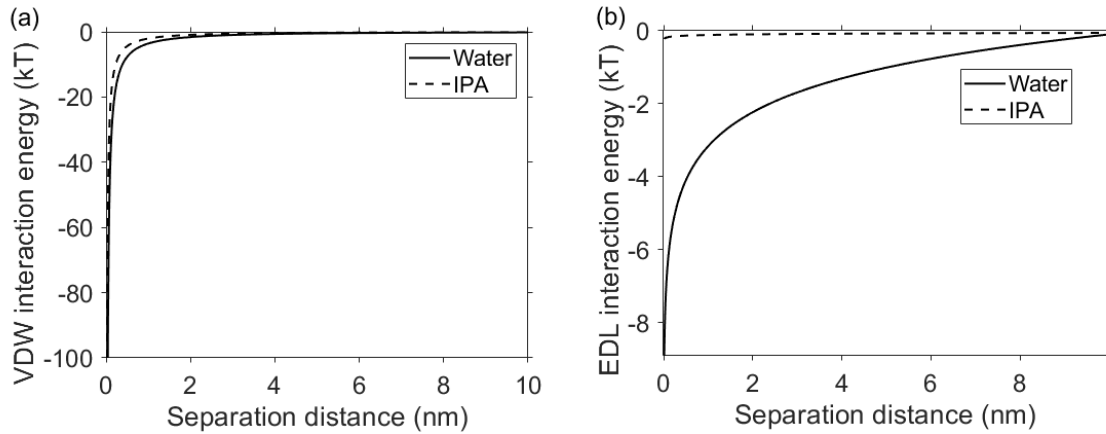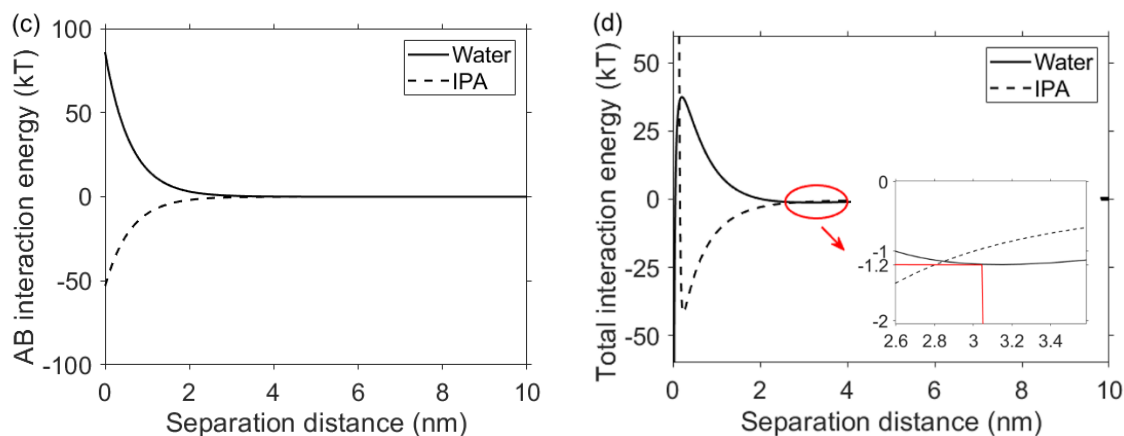
Figure 3.3. xDLVO energy profiles for 10 nm Au NP on PCTE membrane in water and IPA: (a) VDW, (b) EDL, (c) AB, and (d) total interaction energy.

For the PTFE, both experimental and calculation results showed that the NP retention efficiency in IPA was higher than that of water (Fig. 3.2) due to the same reason as PCTE (mainly because of the higher AB attraction energy in IPA, Fig 3.4 (a-c) and Fig 3.5 (a-c). However, an obvious discrepancy between the experiment and calculation in water existed. Fig. 3.4 (d) illustrates the total energy for the PTFE membrane, and it shows a deep secondary minimum (-23 kT) in water because the PTFE membrane has been modified to be positively charged to enhance its attraction to negatively charged NPs (Fig.3.4(b) shows deeper attraction than Fig. 3.3(b)). This deep well having a strong attractive energy should result in a decent deposition efficiency. However, the deposition by this deep secondary minimum (Fig. 3.4d vs. Fig. 3.3d) was not as significant as expected. As the surface of the PTFE is specially treated according to the manufacturer, it is likely that other repulsive forces, e.g., steric repulsive force, exist on the surface typically in water. Further analysis of interaction forces using an atomic force microscope (AFM) to confirm this speculation is needed in the future [128, 129].

For the PVDF membrane, when the UF was performed in water, the result was similar to that of PCTE (refer to the solid lines as the VDW, EDL and AB interaction energy profiles in water in Fig. 3.4 (a-c) and Fig. 3.5 (a-c)), i.e., the shallow secondary minimum (Fig.3.4d) resulting in a 36% deposition. However, a significantly lower retention efficiency compared to PCTE and PTFE was seen when it was in IPA although the transport coefficient (83.1%) in PVDF membrane was as high as that of the PCTE (78.8%) and PTFE (80.8%). Fig. 7 (b) reveals that the lower retention efficiency for PVDF was due to a small energy barrier (0.3 kT, the enlarged figure in Fig. 3.5d) which repulsed ~10% (P_b=0.9) of the transported particles and then the shallow primary minimum (caused by AB interaction, refer to Fig.3.5(c)) resulted in a ~60% of deposition (Maxwell models in Eq. 3.16-3.20) of the 90% particles reached the energy well. Therefore, the total estimated deposition was ~45% (0.83x0.6x0.9), slightly higher than the experimental result of ~36%. It should be noted that the secondary minimum was ignored as the depth was very small.
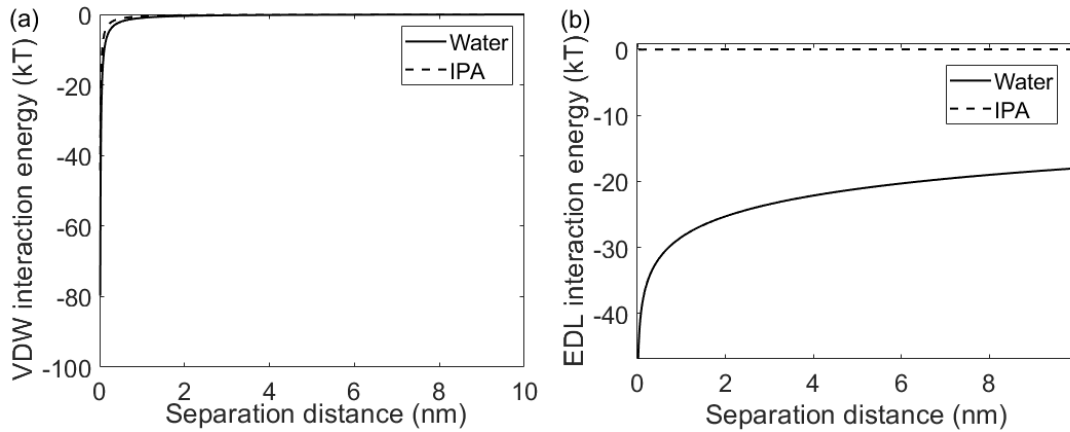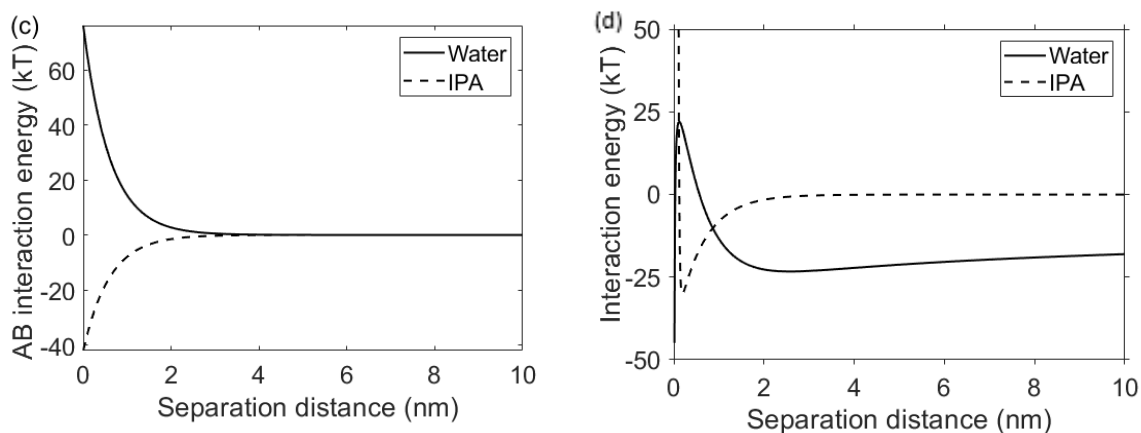
Figure 3.4. xDLVO energy profiles for 10 nm Au NP on PTFE membrane in water and IPA: (a) VDW, (b) EDL, (c) AB and (d) total interaction energy.
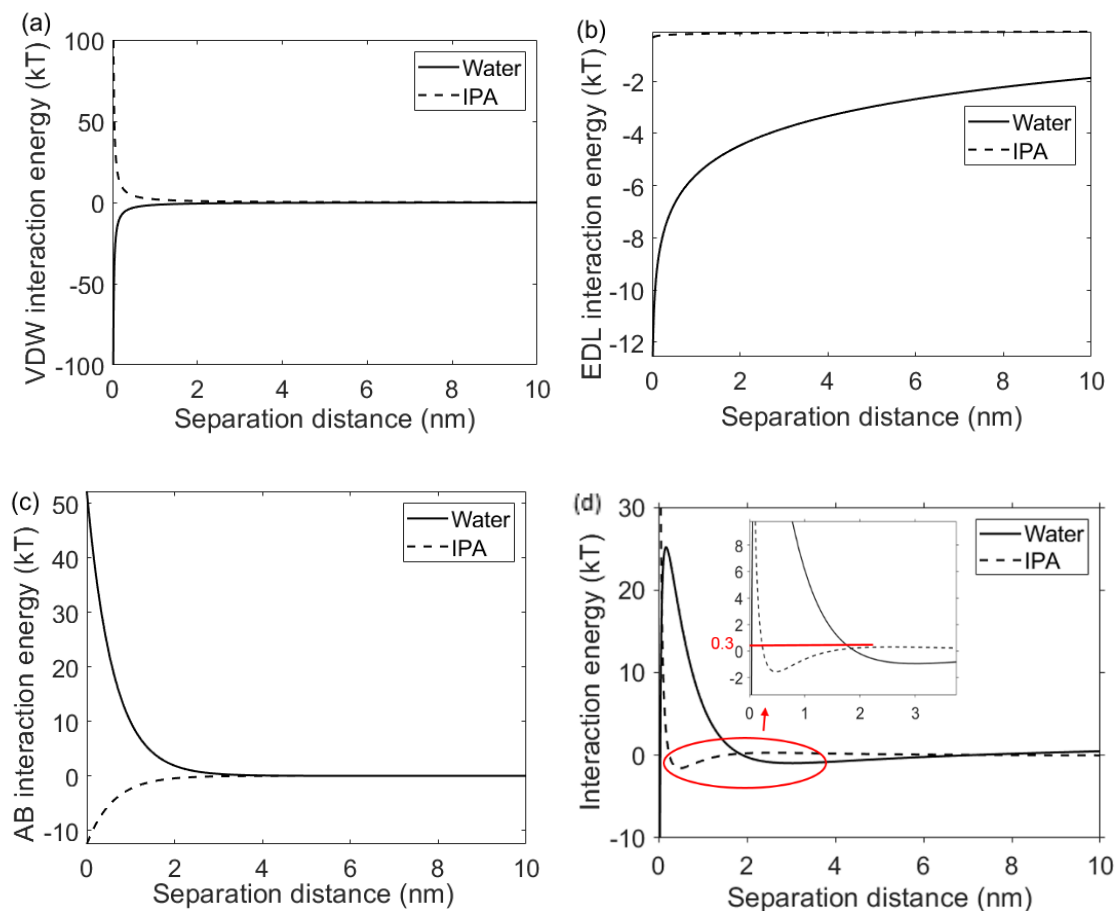
Figure 3.5. xDLVO energy profiles for 10 nm Au NP on PVDF membrane in water and IPA: (a) VDW, (b) EDL, (c) AB, and (d) total interaction energy.

These findings indicate apolar or low polar liquid can change the AB interaction and increase attraction greatly if there is no long-range repulsion. To weaken the long-range repulsion, enhancing the electric attraction is an option. In addition, the material of the membrane and the surface treatment can also largely affect the UF performance.

3.3.2 Retention efficiency for different particles and membranes in IPA

Fig. 3.6 compares the experimental and theoretical retention efficiencies of different sizes NPs by the three membranes in IPA. It clearly shows that the model had a good performance in predicting the retention efficiency for different sizes of particles on different type of membranes in IPA. The theoretical explanations are discussed as follows.
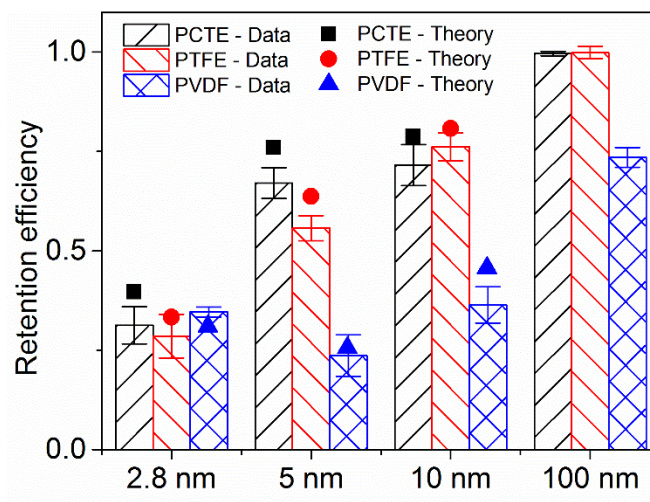
Figure 3.6. Experimental and theoretical retention efficiency of different sizes NPs by the PCTE, PTFE and PVDF membranes in IPA at low flow flux (1.8 mL/min, or 0.0018 cm/s).

Fig. 3.7 depicts the interaction energy curves for the 2.8, 5 and 10 nm NPs against the PCTE in IPA. Fig. 3.7 (d) clearly shows that no energy barriers existed for all three sizes of NPs in the PCTE membrane. However, the depth of the primary minimum for 5 nm Au and 2.8 nm ZnS was much shallower compared to that of the 10 nm Au NPs. This was attributed to the decline of all

attractions, i.e., VDW, EDL, and AB, with decreasing particle sizes (refer to Fig.3.7 (a-c)). The VDW is proportionally associated with Hamaker constant which has been reported to reduce with decreasing particle sizes [130]. EDL was weakened because smaller particles can carry less charges. For AB attraction in IPA, particle size is also an essential factor that significantly influences the strength of the attraction [127, 131]. As a result, the depth of the primary minimum for the 2.8 nm ZnS and 5 nm Au NPs were only 1.0 and 2.9 kT respectively. However, a 5 kT energy is required for the 2.8 and 5 nm NPs to stay deposited on the PCTE membrane. Therefore, the 1.0 and 2.9 kT resulted in the 40 and 76% deposition for the 2.8 nm ZnS and 5 nm Au based on the Maxwell model. If the particle size increased to 10 nm, the attractive energy was calculated to be 41.8 kT and the retention reached 78%. In comparison with the theoretical retentions of 40, 76 and 78% for the 2.8, 5 and 10 nm NPs, respectively, through the PCTE in IPA, the experimental efficiencies were about 31, 67 and 72% (Fig.3.6). The calculated efficiencies were close to the experimental results, where the Maxwell models slightly overestimating the detachment [42].

(d)

66
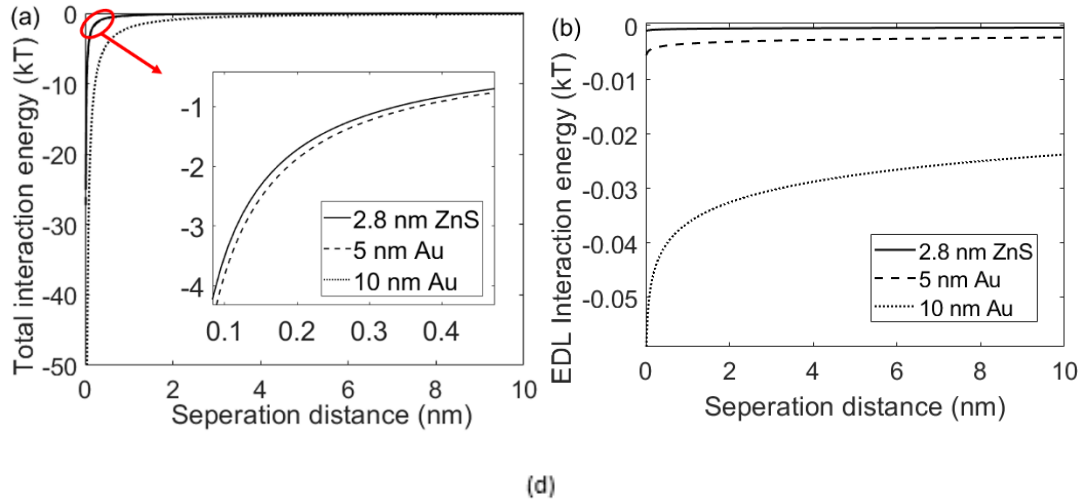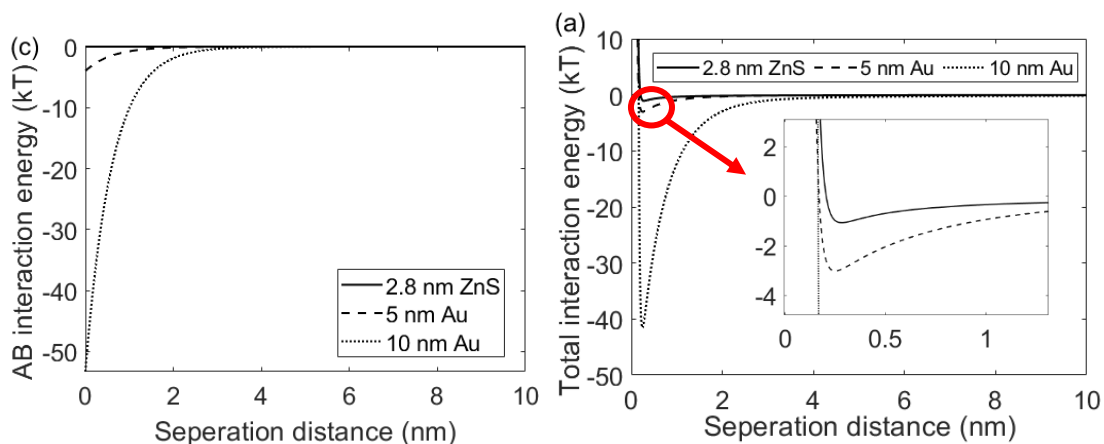
Figure 3.7. xDLVO energy profiles for different sizes of NPs on PCTE in IPA (a) VDW, (b)EDL, (c) AB and (d) total interaction energy.

The trend of the curves and the mechanisms for the PTFE were similar to that of PCTE (Fig.3.8) but with a little shallower primary minimum well (Fig.3.8(d)). The depth of the primary minimum for the 2.8 nm ZnS, 5 and 10 nm Au NPs were 0.8, 1.8 and 30 kT respectively, which resulted in a theoretical retention of 33, 64 and 80% respectively. The experimental efficiencies were about 28, 56 and 76% (Fig.3.6). Maxwell models slightly overestimating the detach ratio [42].
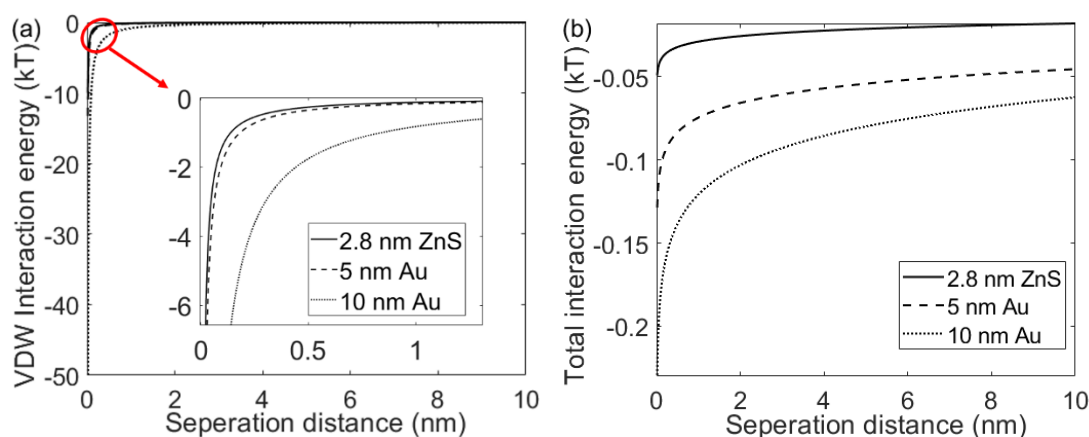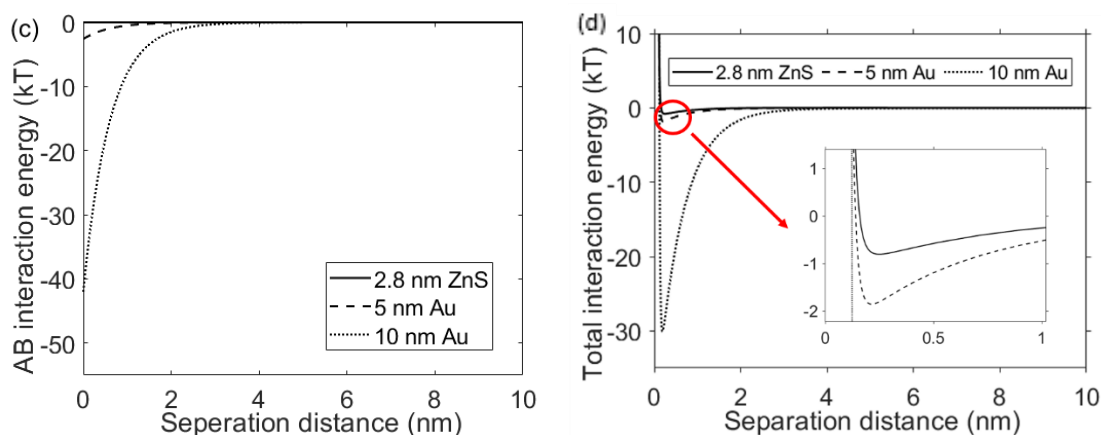
Figure 3.8. xDLVO energy profiles for different sizes of NPs on PTFE in IPA (a) VDW, (b)EDL, (c) AB and (d) total interaction energy.

For the PVDF, the efficiencies were lower than that of PTFE due to different features of the membrane, such as different Hamaker constants (Fig.3.9(a)) and surface tension components (Fig.3.9(c)). The energy wells for the 5 nm Au NPs (0.6 kT) were shallower than the 2.8 nm ZnS QDs (0.7 kT) due to material features. Moreover, a minor energy barrier for the 5 nm Au NPs presented, which further decreased the deposition for the 5 nm Au NPs. Nevertheless, the retentions were still 35% and 24% for the 2.8 nm QDs and 5 nm NPs, respectively. Calculation results also show the same trend (Fig. 3.6).
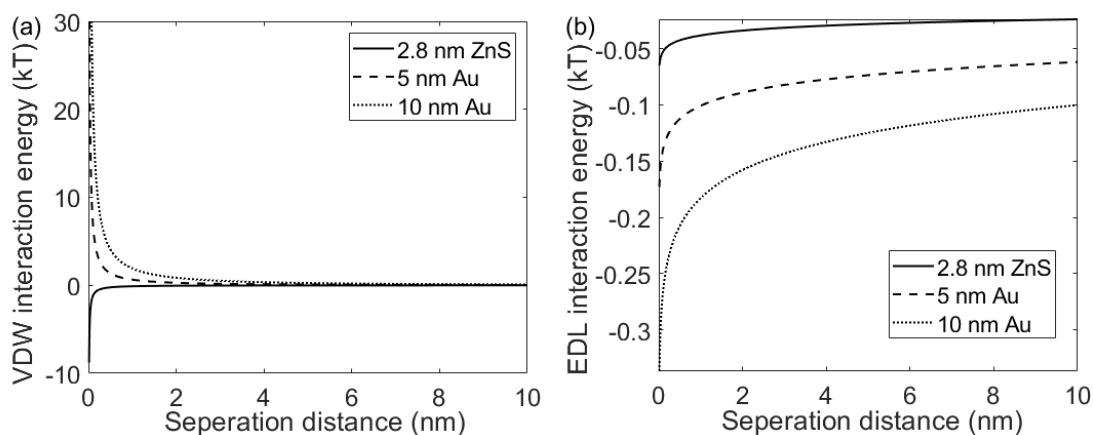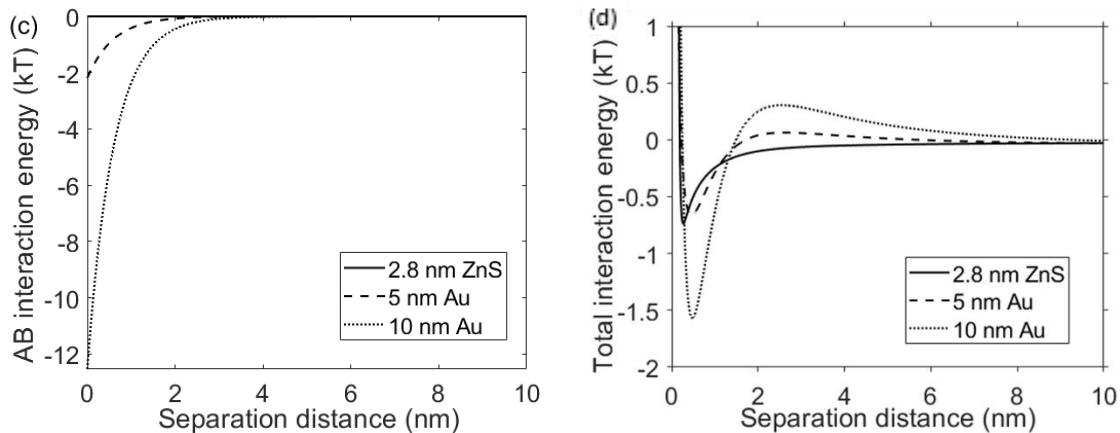
Figure 3.9. xDLVO energy profiles for different sizes of NPs on PVDF in IPA (a) VDW, (b)EDL, (c) AB and (d) total interaction energy.

These findings indicated changing membrane material, particle size and material, and charges on the particles and membranes all possibly can increase the retention efficiency for filtration under PPDR<<1 condition. The highest retention in our study was 76% for 10 nm Au NPs through 130 nm positively charged PTFE (PPDR=0.1). It is very promising to obtain higher retention by using a membrane material with a high Hamaker constant, opposite charges, or changing the polarity of the membrane. Based on the current theoretical model, for example, the retention efficiency can be increased to more than 99% by tripling the thickness of the current PTFE membrane (transmembrane pressure, TMP, ~0.15 bar only) for the 10 nm NPs or by increasing the zeta potential of the PTFE to ~5 and ~10 times for the 2.8 and 5 nm NPs, respectively. In conclusion, it is feasible to use UF membrane to effectively collect sub-10 nm NPs to achieve an energy-efficient and sustainable liquid filtration.

3.4 Conclusions

This study investigated the retention of 2.8, 5 and 10 nm nanoparticles in Milli-Q water and IPA by large-pored ultrafiltration (UF) membranes, including 100 nm rated PCTE and PVDF and

130 nm rated PTFE. xDLVO theory was modified for calculating the interaction energies between the three sizes NPs and different membranes in IPA and water. Combining the filtration models, modified xDLVO theory and Maxwell model, the theoretical retention efficiencies were in good agreement with the experimental data.

It was found that the change of AB interaction from repulsion to attraction resulted in higher retention efficiencies in IPA than that of water for all three membranes. A modification of positive charge on the membrane surface could also contribute to a higher efficiency, i.e., the PTFE with 130 nm pore size had a comparable or greater efficiency for all four sizes of NPs than the PCTE. In addition, enhancing electric attraction could form a secondary minimum which promoted the NP deposition (PCTE and PVDF for 10 nm Au NPs in water). Although efficiencies up to 30, 60 and 75% for 2.8, 5 and 10 nm NPs, respectively, by the 130 nm rated PTFE were observed, further improvement is needed based on the restrict removal requirements. According to the developed models, the retentions of 2.8 and 5 nm NPs can be further increased to 99% by increasing the zeta potential of the PTFE about 10 times for the 2.8 nm NPs and about 5 times for the 5 nm NPs without changing the pore size, which remains a need for future study on modifying the membranes.

Chapter 4. Modeling and optimizing for sustainable design of ultrafiltration system using artificial neural network and particle swarm optimization

Abstract

Ultrafiltration (UF) or nanofiltration (NF) are important processes in many industries for various purposes such as separation, concentration, purification, and waste treatment. As both UF and NF are pressure-driven filtration, a large amount of energy was consumed annually. One potential solution to reduce energy consumption is to use membranes with large pores to filter smaller particles. However, retention efficiency for this type of filtration needs to be increased. This study combined artificial neuron network (ANN) model with particle swarm optimization (PSO) algorithm to optimize filtration conditions for achieving sustainable and high efficiency UF. The optimal parameters included membrane zeta potential, pore size, particle size, particle zeta potential and Hamaker constant which can further determine the type of membrane or particle. Three cases were performed with predetermined input parameters of polycarbonate (PCTE) or polytetrafluoroethylene (PTFE) and without any predetermined parameters. Both Experimental and validated theoretical data were used to train the model. Results showed that ANN models using Levenberg–Marquardt algorithm had best performance, with R2 higher than 0.96. PSO integrated data from ANN and indicated that 45.2 nm PCTE (-14 mV) combined with 3.4 nm Si3N4 (36.5 mV), or 100 nm PTFE (-40 mV) combined with 28.4 nm ZnS (-20.8 mV) can result in a retention efficiency of 99.9%. If membrane type was not predetermined, 52.2 nm fibrous filter with -20.3 mV zeta potential, 5.5 nm nanoparticles with 41.4 mV zeta potential, and a combined Hamaker constant of 0.09 should be chosen. These optimized results were validated by theoretical calculation, providing an effective method to achieve sustainable UF.

4.1 Introduction

Membrane filtration technology is an essential technology that has increasingly been employed in various industries including wastewater treatment plant [132, 133], water desalination

72

and purification [134, 135], food [136], pharmaceutical [137] and semiconductor manufacturing [14, 19, 83, 138]. Membranes with small pore size are usually applied to filter larger particles to obtain a high filter efficiency. However, although this sieving effect can achieve the high efficiency, the pressure drop is normally very high (1-20 bars for ultrafiltration (UF) and 20-100 bars for nanofiltration (NF), which are two commonly used filtrations in those industries) and significant of energy is needed to drive the pumps [107].

In order to reduce the energy consumption, our previous research proposed to use large pore size membranes to filter small particles [111, 139]. The highest retention efficiency based on the available experimental conditions in our lab was up to ~80%. The theoretical analysis indicated that it is possible to improve the retention efficiency to 99.99%. However, it is very difficult to use the theoretical models to determine the precise filtration conditions that can have a 99.99% retention. To begin with, detailed physicochemical properties for particles, membranes, and liquids are needed to run the model. Since many of the parameters are not available from literatures, extensive experimental measurements are still not avoidable (such as fiber diameter, membrane roughness, steric feature of particles, Debye length, zeta potential for particles and membranes, and electron acceptor and electron donor component of surface tension for particles, membranes, and liquids). Second, interrelated relationships exist between different parameters, so it is inappropriate to obtain the filtration conditions for 99.99% retention by changing one parameter while maintaining the same for others, which results in failure of finding the best filtration conditions via theoretical models. Third, a good understanding of filtration process is required to use the model correctly. Three sets of models, i.e., transport models, xDLVO models and Maxwell models, need to be combined to calculate overall the retention efficiency. Appropriate formulas in transport and xDLVO models need to be chosen based on the physical filtration processes. In

73

general, the theoretical models were demonstrated as a very useful method to predict the retention efficiency when all the parameters were known, however, a better and easier method needs to be developed for determining the filtration conditions that can lead to 99.99% retention efficiency.

Machine learning has been applied progressively during the years for simulation and optimization of membrane separation processes [47, 140, 141]. One such example is the use of artificial neural network (ANN), which is a data-driven method and can predict outputs without the need for knowing detail information of each input (detailed features for particles, membranes, and liquids) or a comprehensive understanding of filtration mechanisms [142-144]. Dornier et al. [145] introduced multilayer perceptron (MLP) ANN to dynamically model membrane fouling in a crossflow microfiltration (MF) system for the first time in 1995. Results showed that the MPL ANN model had a satisfactory prediction of the evolution of the total hydraulic resistance during filtration for both constant and variable operating conditions. Inspired by this successful case, a growing number of studies have applied ANNs for predicting and better control membrane fouling for different pressure driven membrane filtrations. Researchers applied different ANN models to study transmembrane pressure, hydraulic resistance or permeate flux for UF [146-148]. The ANN models were demonstrated to have good performance in predicting the parameters and outperformed other conventional models. ANN models were also utilized to predict ion rejections for NF [149-151]. Results showed that the models were able to accurately compute the rejections with the absolute deviation less than 5%. For RO process, the ANN models were relatively more complicated than that of MF, UF and NF [152-154]. However, the prediction results still showed good agreement with experimental results. Moreover, in the analysis of the application of ANN on membrane filtration, it was discovered that the majority of the studies (9 out of 10, 18 out of 19, 10 out of 12, and 18 out of 20 for MF [155-164], UF [51, 52, 54, 56, 58, 165-175], NF [55, 59,

176-182], and RO [183-199] applications, respectively) utilized MLPANN, which proved to be effective in producing accurate outcomes. However, most of these studies focused on predicting the filtration performance, limited studies extended their research to optimize performance [56, 154, 175].

To conduct optimization, an appropriate optimization algorithm needs to be chosen. It has been reported that meta-heuristic algorithms are widely used to handle real-life and hard nonlinear engineering problems [200, 201]. Meta-heuristic algorithms are population-based artificial methods that have many advantages compared with the conventional methods, such as their ability to handle complex problems, shorter running time, reduced susceptibility to local optima and minimal tuning requirements [202]. Among heuristic algorithms, particle swarm optimization (PSO) algorithm and genetic algorithm (GA) were most popular. A common application is to employ the algorithms to optimize architecture of ANNs, with the aim of achieving higher prediction accuracy [52, 203, 204]. PSO model was also found to be used as an intelligent controller to monitor permeate flux in preventing flux decline from membrane fouling [74, 205]. For performance optimization, Soleimani et al. [175] coupled ANN with GA to optimize TMP, cross-flow velocity, feed temperature and PH to obtain maximum permeation flux and minimum fouling resistance for oily wastewater treatment. Badrnezhad and mirza [56] did a follow up research by adding filtration time as fifth optimization parameter and using maximum permeation flux as the optimization objective. In addition, Madaeni and Kurdian [154] applied ANN-GA model to optimize control strategies for a water treatment plant with RO filtration. These three literatures are the only ones that studied optimum operating parameters for membrane filtration using optimization algorithms so far. To our best knowledge, PSO has not been used to investigate optimized filtration conditions. It was observed that PSO has a very high computational speed

compared to GA, which have relatively complicated algorithmic structures and should activate so many exploration/exploitation operators at each iteration. In addition, PSO showed much robust optimization results, and was easier to converge [67]. Therefore, studies using PSO method to optimize the operation conditions are needed.

In this study, a hybrid machine learning model, ANN-PSO model, will be established to predict the retention efficiency and optimize the operation conditions for the sustainable ultrafiltration. This model is to provide a convenient and effective method for researchers or engineers to design sustainable filtration.

4.2 Methods

4.2.1 Filtration mechanisms

This study focused on filtering NPs using ultrafiltration membranes with pore size at least 5 times larger than the particle size. The initial retention efficiency was studied by a dead-end filtration system (left side of Fig.4.1). The influent with the colloidal particles were pumped through the peristaltic pump to the filter holder where an ultrafiltration membrane was fixed inside. With a constant filtration velocity of 0.0018 m/s, the NPs were filtered by the membrane and the effluents were collected. The filtration happened in the filter holder is illustrated in the right side of Fig.4.1. It can be considered as two stages. First, the NPs were transported to the vicinity of the membrane. Due to the small size (smaller than 10 nm), the main transport mechanism is diffusion. After the NPs reach the surface of the membrane, the interactions between the particle and the membrane will occur due to Van del Waals force, electrostatic force, and other physicochemical forces (such as acid base interaction force). Based on the total interaction energy, particles with lower energy will attach to the membrane while some other particle with higher energy will escape.

76

Retention efficiency is defined as the ratio of particles that are not penetrated to the total particles.
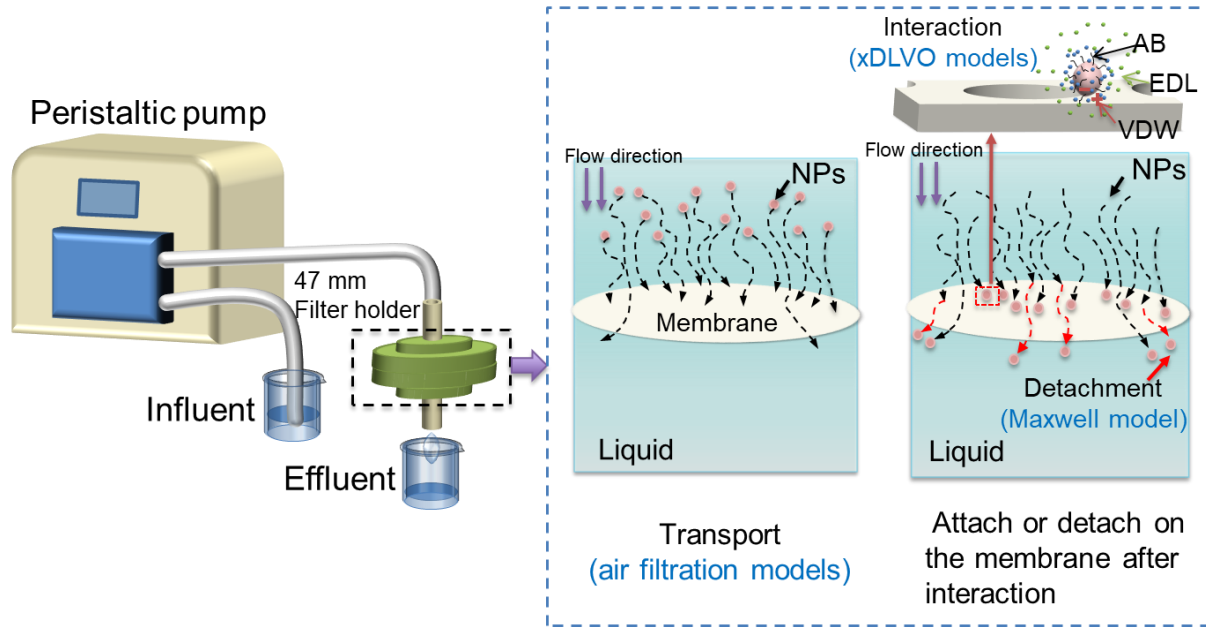
Figure 4.1. Schematic of ultrafiltration for nanoparticles smaller than 10 mn. VDW is the Van del Waals interaction, which is cause by correlations in the fluctuating polarizations of nearby particles. EDL is the electrostatic double layer interaction. The blue dots and the green dots in the figures represent the first and the second electric layer respectively. AB is the acid base interaction, which is caused by the hydrophilic/hydrophobic groups.

4.2.2 Measurement method

To obtain the penetrated and original concentrations, ES-SMPS system was extended to use to measure particle size distribution and concentration in both influent and effluent. The schematic of measuring system and a detailed description can be found from Chapter 2. It has demonstrated that this method can effectively measure particles down to 2.8 nm and has low requirement on colloidal concertation (10^7 p/ml) in the liquid [22, 139].

In this study, the ES-SMPS was applied to measure the retention efficiency for Au and PSL NPs on PCTE, PTFE and PVDF membranes respectively in water. The properties can be found from chapter 2 [139].

4.2.3 Theoretical models

To explain the retention efficiency, theoretical models need to be developed. It has been reported that DLVO/xDLVO theory can predict the deposition trend for either particle-particle or particle-surface problems. However, one theory alone is not capable of predicting the efficiency quantitatively. Lee et al. [24] and Fan et al., [111] added transport functions and hydration equations to calculate the retention efficiency for particles larger than 40 nm in water. Results showed that their models agreed with the experimental data very well. However, the properties of IPA differ from those of water, including electrokinetic properties that can substantially impact particle-membrane interactions and, consequently, alter retention efficiency. In addition, very small particles (down to 2.8 nm) needed to be considered in our study, which might be beyond the applicable range for some equations in the xDLVO theory. Therefore, a modified set of the models were developed (Chapter 3). Overall, three models were integrated to cover the entirety of the filtration processes. To account for the transport process, capillary tube models and single fiber theory were utilized for PCTE and fibrous membranes, respectively. In the interactions process, xDLVO models were employed, using a modified Hamaker constant and a constant potential EDL equation, found to be appropriate for small particles and organic solvents, respectively. Lastly, to calculate detachment ratio, the Maxwell model was applied since high kinetic energy is the primary reason for small particles to escape from the membrane.

After the models are validated by experimental results, they are further used to predict the retention efficiency for other particles (ZnS, SiO_2, Al_2O_3, and Si_3N_4) which are most used in

semiconductor factories (Table 4.1) [9]. The combined experimental and calculation data were used as the input for the ANN model due to limited experimental condition. It is worth noting that a total of 24 parameters (Table 4.2) needs to be known to obtain the retention efficiency from the models.

Table 4.1 Summary of experimental and calculation conditions

	Experiment	Calculation
Membrane type	PCTE, PTFE, PVDF	PCTE, PTFE, PVDF
Pore size	100	50, 100, 150, 200
Particle type	Au, PSL	ZnS, SiO2, Al2O3, Si3N4
Particle size	5,10,30,50 for Au; 100 for PSL	5, 10, 30, 50,100

Table 4.2. Input parameters for theoretical models

	Input for the theoretical model
Particle	Diameter
	Zeta potential
	Dielectric permittivity
	Refractive index
	Electron acceptor component surface tension
	Electron donor component surface tension
	Fiber diameter
	Solidity
	Thickness
	Zeta potential
Membrane	Dielectric permittivity
	Refractive index
	Electron acceptor component surface tension
	Electron donor component surface tension
	Pore radius

	Porosity
	Viscosity
	Dielectric permittivity
	Refractive index
liquid	Electron acceptor component surface tension
	Electron donor component surface tension
	Debye length
Temperature	Temperature
Face velocity	Face velocity

4.2.4 ANN model

Although the theoretical model can predict the retention, it requires the information for a lot of parameters in the models and the calculation process is very complicated and tedious. In contrast, ANN can map and predict continuous relationship between inputs and outputs by developing a gain term to connect target variables with necessary sets of input variables. Physical–chemical relationships between input variables and output variables are not necessarily known.

Multilayer perceptron (MLP) is the most common type of neural network used for supervised prediction. The MLP-ANN consisted of three layers including input layer, hidden layer, and output layer. Each input parameter is represented as a neuron in the input layer. In order to increase the model's applicability in selecting different types of membranes or particles, this study employed the Hamaker constant as one input instead of membrane type and particle type. Hamaker constant is determined together by material properties of membrane and particle in water system, therefore, a determined Hamaker constant allows optimizers to choose any kind of membrane or particle based on the available information, such as pre-determined membrane or particle or neither. To explain the application, this study run three cases: predetermined PCTE, predetermined PTFE and

non-predetermined parameter cases, respectively. As the principles are the same but with less input

paraments for the predetermined cases, the elaboration is focused on the last case. However, the

results from PSO optimization included all the three cases.

In addition to Hamaker constant, pore size, particle size, and zeta potentials for the

membranes and particles, respectively, are independent other input parameters that optimizers can

chose to achieve their optimization objective. Therefore, the input layer comprised five neurons

with detailed information listed in Table 4.3. In the hidden layer, the number of neurons was

determined by minimum error value to obtain the best performance of the model. This study only

set one output neuron (retention efficiency) in the output layer. The structure of the developed

ANN used for prediction of the efficiency is shown in Fig. 4.2.

Table 4.3. Summary of input parameters

Input parameter	Range
Membrane zeta potential (mv)	(-40)-(-14)
Hammaker constant	0.02-4.77
Pore size (nm)	50-200
Particle size (nm)	5-100
Particle zeta potential (mv)	(-63.5)-(42)
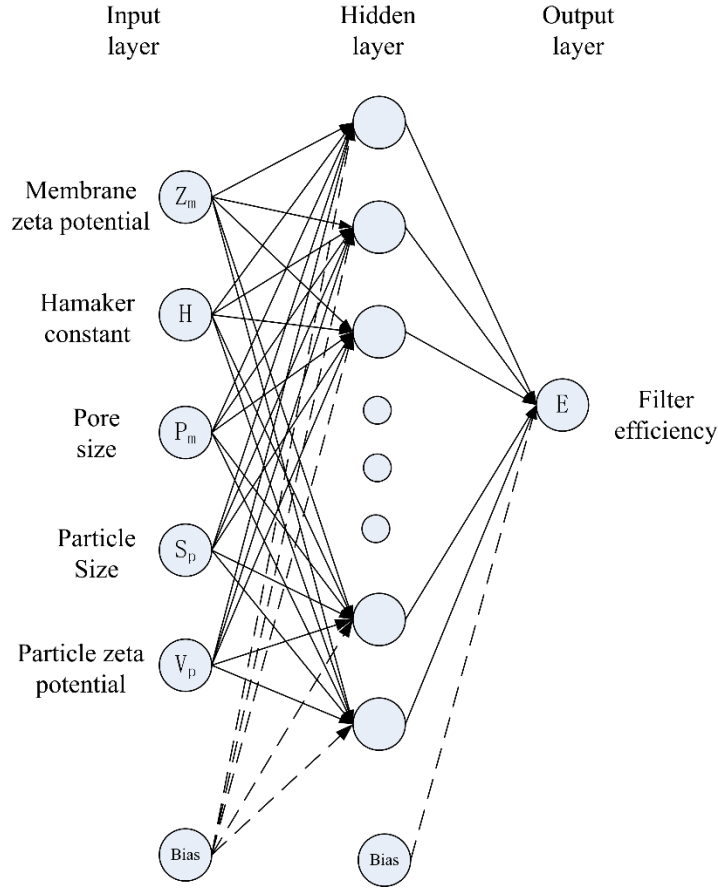
Figure 4.2. Architecture of the multilayer perceptron artificial neural network (MLP-ANN) model

The MLP-ANN needs to be trained and validated. The training process includes three stages:

(i) Feedforward of the input training pattern.

The data flows in the forward direction from input to output layer. In the input layer, the numerical parameters were normalized to the range of (-1,1), which is good for stability and convergence of the ANN model. The normalization method is as follow [46]:

$$M = \frac{M_{max} - M_{min}}{X_{max} - X_{min}} \times \left(X - X_{min} \right) + M_{min} \tag{4.1}$$

where M is the normalized input vector, X is the original input vector, M_{max} is the set to +1 and M_{min} is the set to -1, X_{max} is the maximum value of the input, X_{min} is the minimum value of the input.

(ii) Calculation and back propagation of the associated error

The neurons in the MLP are trained with the back propagation learning algorithm. All the neurons were summed up with weights and bias. Transfer function determines the input–output behavior and adds nonlinearity and stability to the network [206]. Hyperbolic tangent sigmoid activation function was employed in both the hidden and output layers respectively. Assume there are two neurons in the hidden layer, the calculation can be expressed through eq. (4.2) - (4.5)

$$H_{11} = \tanh\left(b_{h11} + \omega_{h11}Z_m + \omega_{h12}H + \omega_{h13}P_m + \omega_{h14}S_p + \omega_{h15}V_p\right) \tag{4.2}$$

$$H_{12} = \tanh\left(b_{h12} + \omega_{h21}Z_m + \omega_{h22}H + \omega_{h23}P_m + \omega_{h24}S_p + \omega_{h25}V_p\right) \tag{4.3}$$

$$\tanh(x) = \frac{e^x - e^{-x}}{e^x + e^{-x}} \tag{4.4}$$

$$g_0^{-1}(E) = b_o + \omega_{o1}H_{11} + \omega_{o2}H_{12} \tag{4.5}$$

Where H_{11} and H_{12} are the neurons in the hidden layer. b_{h11}, b_{h12} are the bias in hidden layer, and b_o is the bias in the output layer. ω_{h11}, ω_{h12}, ω_{h13}, ω_{h14}, ω_{h15} are the weights in the hidden layer, and ω_{o1} and ω_{o2} are the weights in the output layer. Z_m, H, P_m, S_p and V_p are the input parameters. $g_0(E)$ is the transformation of the expected target (E, efficiency) as the inverse of output transfer function.

The model was trained by different learning algorithms (gradient descent algorithm GDA, incremental back propagation, IBP, Levenberg–Marquardt algorithm, LM)

(iii) The adjustment of weights.

The weights were initialized with random values and then the ANN output corresponding to the input patterns were compared with the target values and the weights were adjusted to minimum the errors. root mean squared error (RMSE) and coefficient of determination (R^2) were used. Each network was trained until the network average RMSE was minimum and R^2 was close enough to 1. Other parameters for network were chosen as the default values of the software (learning rate = 0.1 and momentum = 0.4).

$$RMSE = \sqrt{\frac{\sum_{i=1}^{n}\left(x_c^i - x_t^i\right)^2}{n}} \qquad (4.6)$$

$$R^2 = 1 - \frac{\sum_{i=1}^{n}\left(x_c^i - x_t^i\right)^2}{\sum_{i=1}^{n}\left(x_t^i - x_m\right)^2} \qquad (4.7)$$

where x_c^i is the predicted value of the output, x_t^i is the target value of the output, x_m is the mean value of all of the output, and n is the number of data points in the training or validation data set.

After the model was trained, a second set of validation data was used to evaluate the quality of the network during training. This study used 6-fold cross validation. Five folds as the training set and the rest one-fold as the testing set to validate the model. An additional unseen dataset of used to test the validated model. A set of 360 of experimental data and theoretical calculation data were used for the network. ANN modeling was performed using the neural network toolbox of Matlab 2021b (Mathworks Inc., USA).

4.2.5 PSO model

The PSO algorithm is a population-based search algorithm, which has been prevalently applied to solve engineering optimization problems. This algorithm is inspired by the behavior of

a swarm of ants, a flock of birds, or a school of fish when they are finding food or encountering danger. The evolutionary algorithm was developed by Kennedy and Eberhart [207] in 1995 and they mentioned that when birds are searching randomly for food in a flock, all birds in the flock can share their discovery and help the entire flock get the best hunt. This process is called exploration and exploitation.

In PSO algorithm, ants/birds/fish are represented by volume-less particles in the optimization algorithm. A swarm of particles located randomly in the searching domain is initially selected. These particles update their position with some velocity (movement of the ants/birds/fish) until the best position (best hunt) is found. For computationally implement, each particle is presented by its position vector as:

$$X_i(t) = [x_{i1}, x_{i2}, ..., x_{iD}], i = 1, 2, ...N \tag{4.8}$$

where t is the generation time, N is the swarm size, and D is the dimension of the searching domain. $x_i(t)$ is the solution of the optimization problem, and the swarm is a set of swarm = {x_1, x_2, . . ., x_N}.

To formulate the evolutionary mechanism, a velocity vector is assigned to each particle as follows:

$$V_i(t) = [v_{i1}, v_{i2}, ..., v_{iD}], i = 1, 2, ...N \tag{4.9}$$

where $v_i(t)$ is the velocity of the ith particle.

In a classic variant of the PSO, the updating rule is mathematically expressed as follows:

$$v_i(t+1) = w \cdot v_i(t) + c_1 \cdot r_1 \cdot (p_i(t) - x_i(t)) + c_2 \cdot r_2 \cdot (p_g(t) - x_i(t)) \tag{4.10}$$

where w is the inertia weight constant. Higher values of w result in more exploration behavior, whereas a lower value increases the exploitation performance. c_1 and c_2 are the cognitive and the social acceleration coefficients, respectively, and r_1 and r_2 are the two random numbers uniformly distributed within [0,1]. $P_i(t)$ is the best previous position of particle i, and $P_g(t)$ is the best position of all the particles. $P_g(t)$ is called the global best solution of the minimization/maximation problem, the position of $P_g(t)$ has the lowest fitness function value.

After updating the velocity of the particle, each particle adjusts its current position using the following relation:

$$x_i(t+1) = x_i(t) + v_i(t+1), i = 1, 2, ... N \qquad (4.11)$$

The particles will move iteratively to update the position until the optimal solution is found.

In this study, the ANN output (filter efficiency) is the particles in the PSO model. The flowchart is shown as Fig. 4.3.
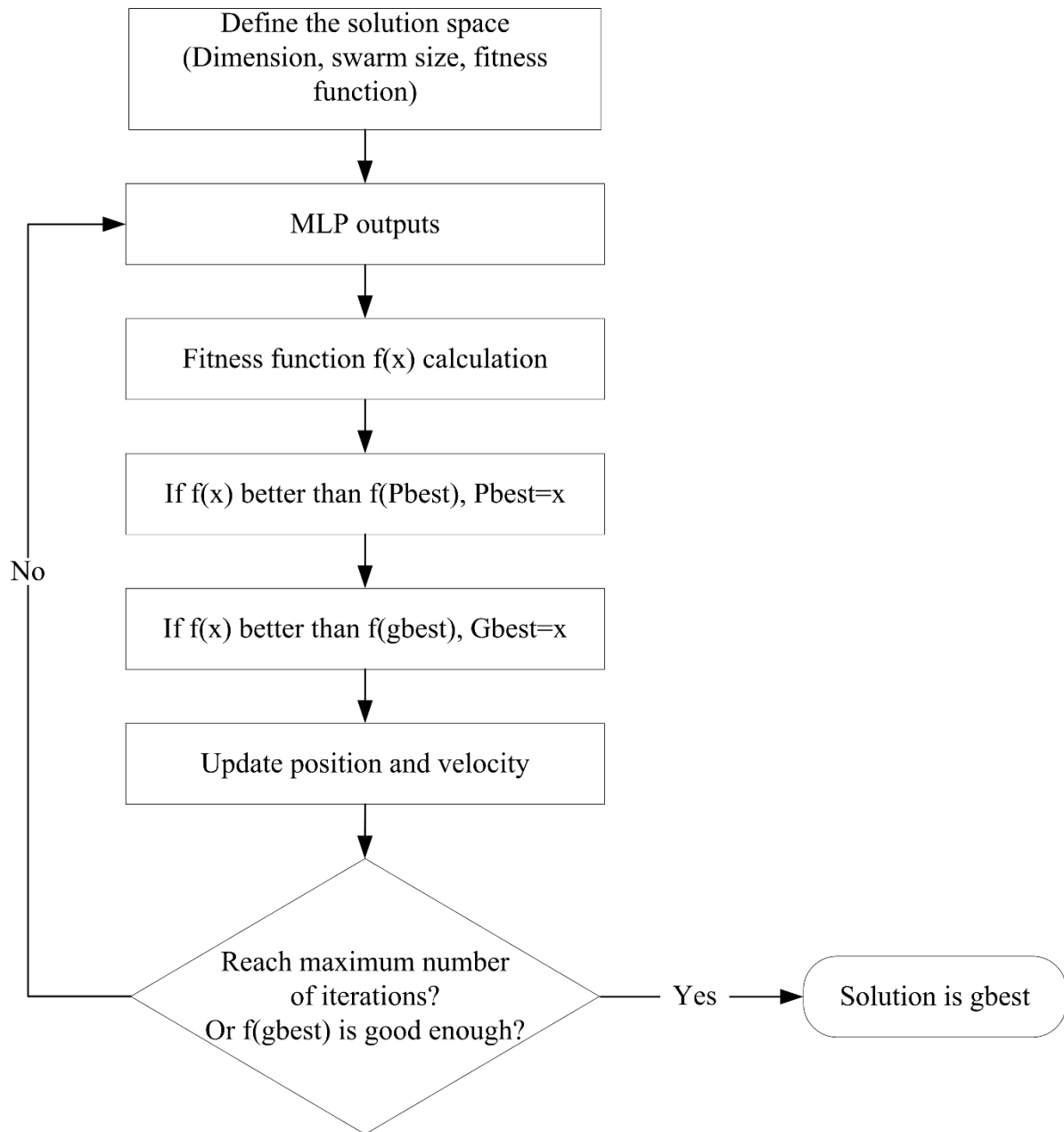
Figure 4.3. Flowchart of the PSO algorithm

4.3 Results

4.3.1 Experimental and theoretical results

This study used experimental data combined with theoretical calculation data to train the ANN model. To ensure the data is reliable, the theoretical models need to be validated. After the validation, the theoretical models were used to generate more data.

4.3.1.1 Validation of theoretical models

Experimental data were compared with theoretical data in Fig.4.4. The experimental data covers a wide range of efficiency from 3% to 98.5% and experimental conditions included various influencing factors, including different kinds of membranes, different sizes of particles and different kinds of particles. As shown in Fig.4.4, the calculated data agreed with all the experimental data satisfactorily. Although some of the calculated results were slightly higher than experimental results, it attributed to overestimation of deposition ratio from Maxwell model. As the deviations were acceptable, the models were considered to have good performance and further used to generate more input data. It should be noted that the pore sizes of the membranes were 100 nm, so the retention efficiencies for the 100 nm PSL were mainly due to sieving, which was not included in the input dataset.
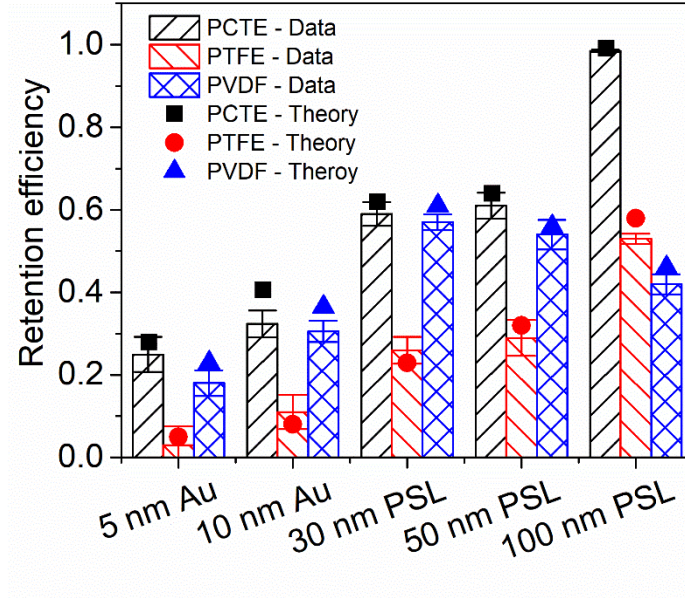
Figure 4.4. Experimental and theoretical retention efficiencies of different sizes NPs by the

PCTE, PTFE and PVDF membranes in water

4.3.1.2 Influencing factors on retention efficiency

Based on the model, retention efficiencies for the other particles (Table 4.1) were calculated. In Fig.4.5(a) and Fig.4.5(c), there are overlapped points, i.e., points represented SiO_2 and Al_2O_3 particles are overlapped with points represented Si_3N_4. This is because the overall interactions were all strong attractive and thus the total retention efficiency was the transport efficiency which is independent with particle material.

Compare the retention efficiencies on three membranes, Fig.4.5 shows that PCTE and PTFE membrane had more high efficiency points. Two possible reasons can be: the transport efficiency for PCTE and PTFE membrane were higher than that of the PVDF when the total interaction was attractive, or repulsive interactions between the particles and PVDF occurred and stronger than the other two membranes. Therefore, in order to obtain high retention efficiency for the particles in Table 4.1, it is suggested to use PCTE or PTFE membrane. For PCTE membrane, the high

efficiency happened when Si₃N₄ nanoparticles were used. For PTFE membrane, the high

efficiency could be obtained when ZnS nanoparticles were challenged.
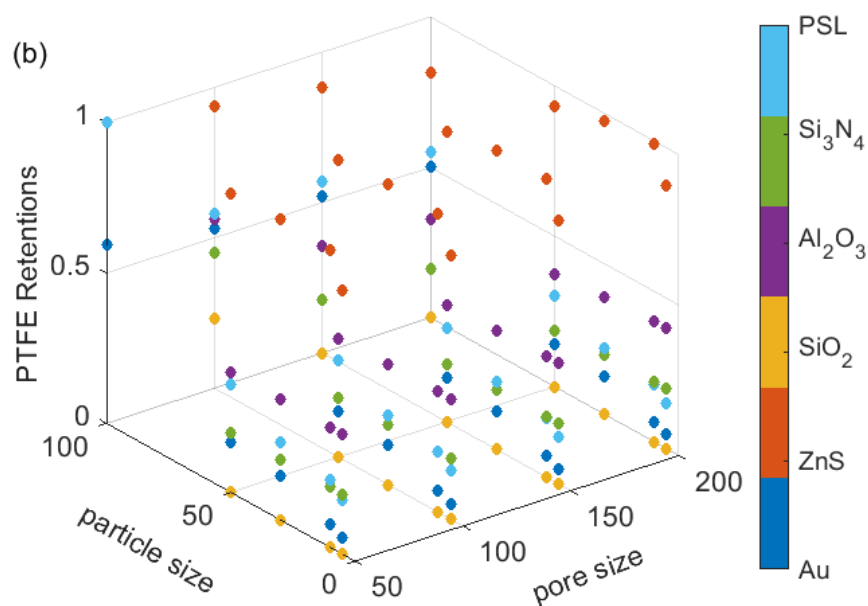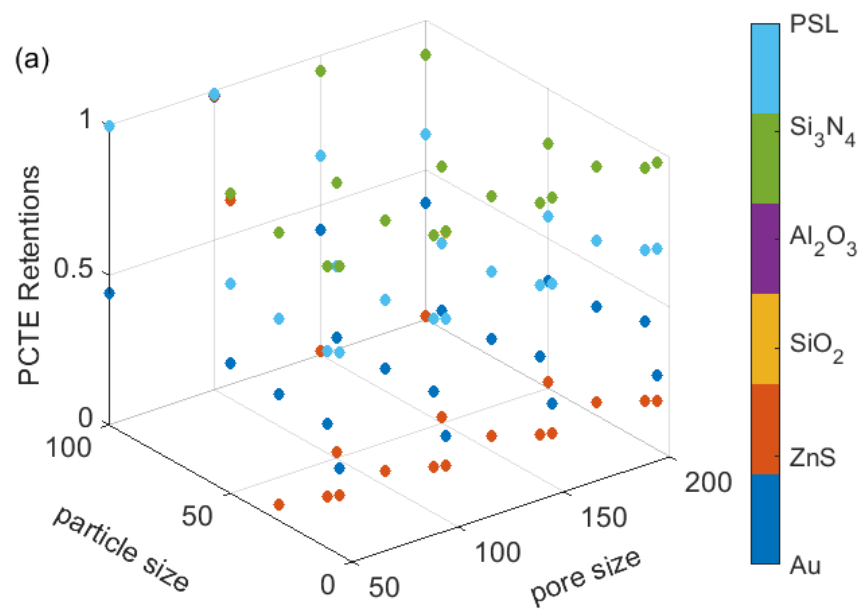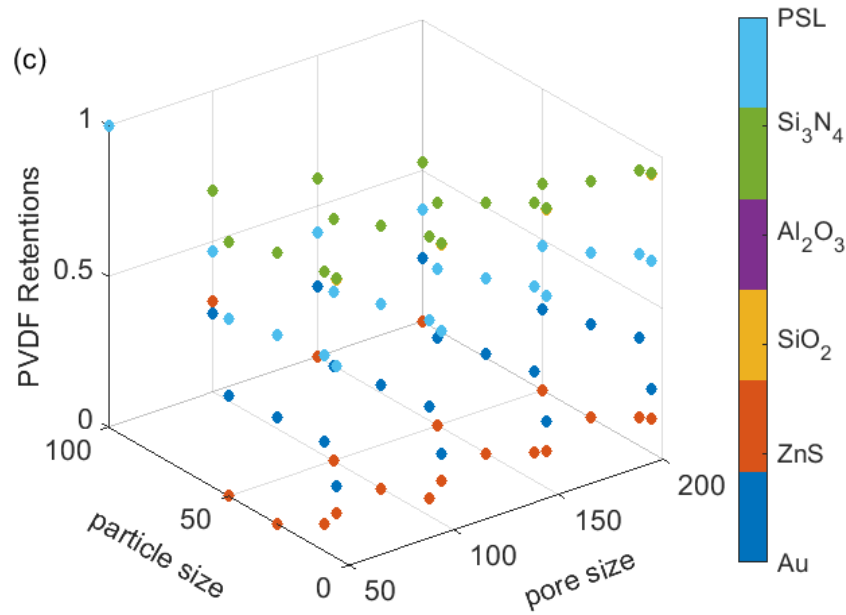
Figure 4.5. Distribution of retention efficiencies under different input parameters for (a) PCTE, (b) PTFE and (c) PVDF membrane

4.3.2 Performance of ANN model

In order to accurately predict the retention efficiency, different ANN structures were applied. It was found that one hidden layer was sufficient which agrees with the universal approximation theory [208]. The neurons in the hidden layer were determined by the RMSE value. As depicted in Fig. 4.6, the error initially decreased due to increasing number of weights and later increased probably because of overfitting. When the number of neurons were 18, the RMSE values for all datasets were the lowest. Therefore, the architecture of the ANN model was chosen to be 5-18-1. The learning algorithm were determined through trial-and-error method, and LM was found to have the best performance.
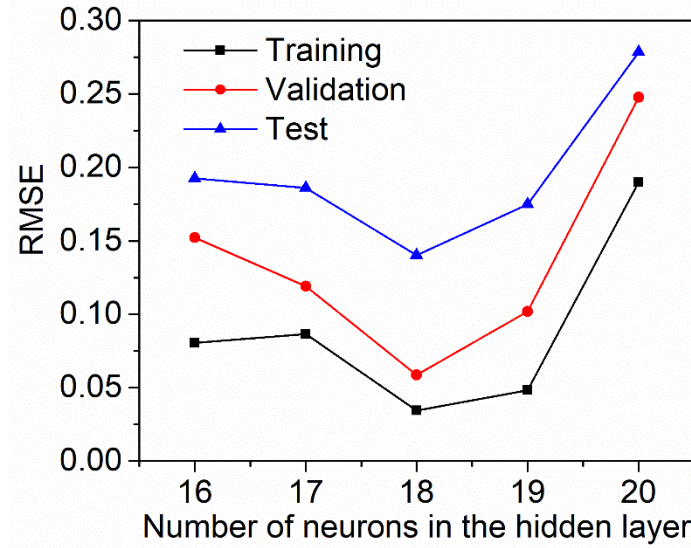
Figure 4.6. Effect of number of neurons in the hidden layer on predicting accuracy of retention efficiency

Fig. 4.7 illustrates the regression plots of normalized predicted value against normalized target value. The lines in the figures have an intersection of 0 and a slope of 1. If the datapoint lies on the line, it means the predicted value exactly equals to the target value. R^2 would be 1 if all the datapoints lie on the line, which is the ideal result. It can be observed from Fig. 4.7 that the R^2 values for training and validation datasets were both higher than 0.99 and the R^2 value for test dataset was also as high as 0.96. The results indicate that the model had good performance in predicting the retention efficiency.

It should be mentioned that a high ratio of extreme values (0 and values near to 1) exists in the input data and predictive performance for all models decreases when attempting to predict extreme values [209, 210]. Kovacs et al. [211] compared the model performance in predicting extreme values for random forest (RF), ANN and long short-term memory (LSTM) models. They reported that ANN model predicted higher values than the experimental values. In Fig.4.7, the

outliers near to 0 and 1 were all higher above the fitting line, which agrees with results from other researchers [211].
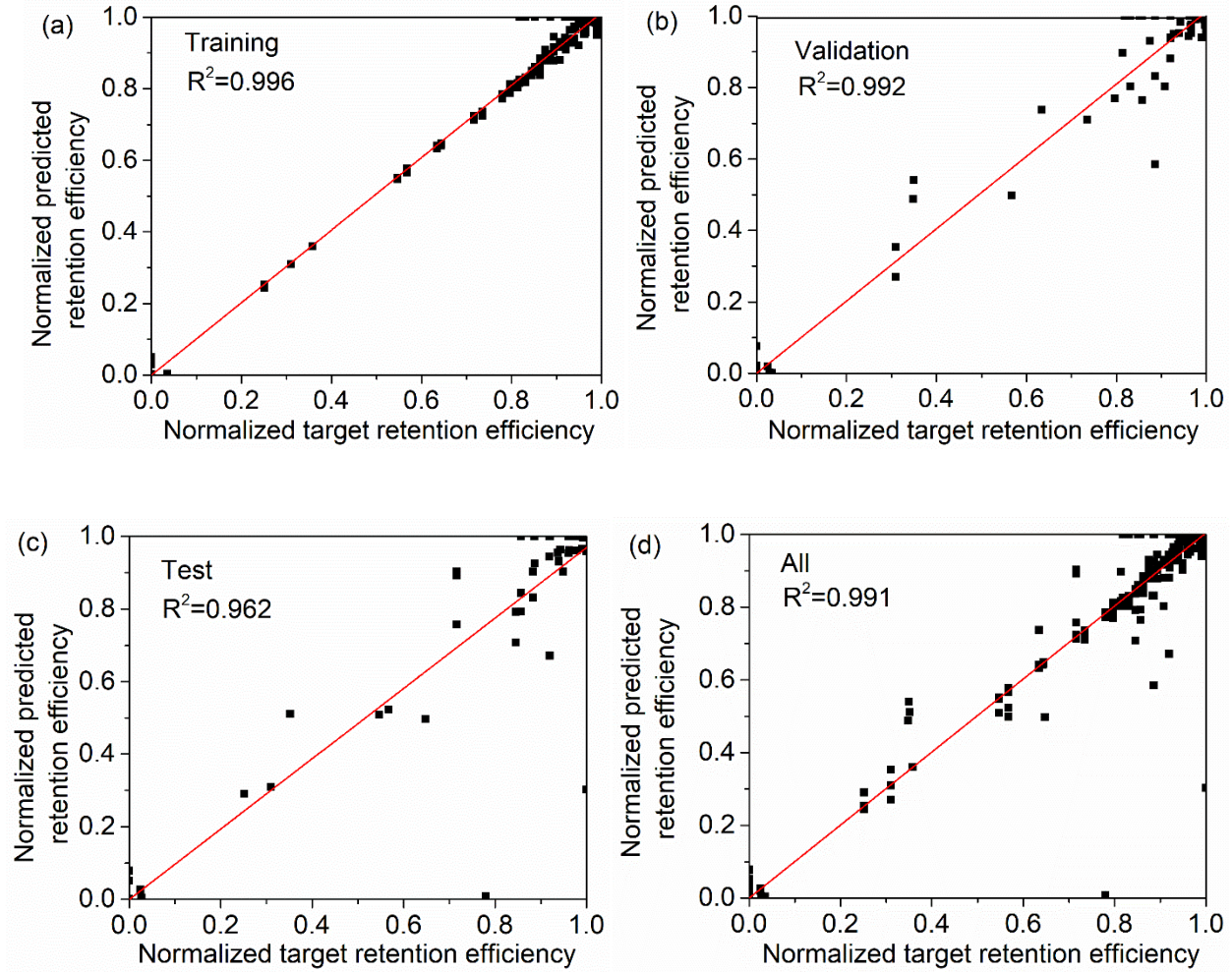
Figure 4.7. Comparison of normalized ANN predicted values and normalized target values for (a) training, (b) validation, (c) test and (d) total dataset

4.3.3 Optimization of filtration condition

After the ANN model was well trained, this study integrated the results to PSO model to find the filtration condition that has highest retention efficiency. ANN-PSO were run for three cases: one was to find the best filtration condition for PCTE membrane (case 1); the second was to find

the best filtration condition for PTFE membrane (case 2); the last one was to find the optimal condition for all five inputs without restrictions (case 3). Table 4.4 listed the optimized results.

Table 4.4 Optimal solutions for highest retention efficiency

	Membrane type (Zeta potential, mV)	Pore size (nm)	Zeta potential for the particle (mV)	Particle size (nm)	Particle type (Hamaker)	Efficiency from theory	Efficiency from PSO
Case 1	PCTE	45.2	36.5	3.4	Zi_3N_4 (2.386)	99.5%	99.9%
Case 2	PTFE	100	-20.8	28.4	ZnS (0.086)	99.7%	99.9%
Case 3	Fibrous (-20.3)	52.2	41.4	5.5	0.09	99.9%	99.9%

In Table 4.4, when the membrane was PCTE, a 45.2 nm pore size and 3.4 nm Zi_3N_4 NPs with zeta potential of 36.5 should be chosen to reach an efficiency of 99.9%. Compared with the results in Fig.4.5(a), it can be observed that optimized the condition lies within the high efficiency region (top green points). In fact, theoretical calculation result indicated that the efficiency was 99.5% under this condition, which was very close to the result optimized by PSO. Similarly, when the membrane was PTFE, the chosen condition is in the high efficiency region (top red points) based on Fig. 4.5(b) and the theoretical result (99.7%) was very close to 99.9%. For the third case, the optimal solution is more unrestrained. To reach a retention efficiency of 99.9%, the designer can choose a fibrous filter with -20.3 mV zeta potential and 52.2 nm pore size and particles with 5.5 nm in size and 41.4 mV zeta potential as long as their Hamaker constant is 0.09.

The result of the ANN-PSO models showed that machine learning method is an effective method to estimate retention efficiency with great accuracy and generalization ability. The models can provide an ultrafiltration strategy with high filter efficiency but low energy consumption. The

simple input parameters facilitate researchers to design sustainable ultrafiltration system without using the complicated theoretical models.

4.4 Conclusions

This study proposed optimal strategy for designing energy saving ultrafiltration system using machine learning technique. Filter efficiencies were experimentally and theoretically collected as input data for ANN-PSO model. Input parameters included zeta potential for the membrane, Hamaker constant, pore size, particle size and zeta potential for the particles. ANN model with an architecture of 5-18-4 and LM learning algorithm was found to have the best performance. The predicted values were highly correlated with the target values, with R^2 of 0.996, 0.992 and 0.962 for training, validation, and test dataset, respectively. ANN was also further applied to calculate filter efficiency when the membrane type (PCTE or PTFE was chosen) was predetermined.

Based on the ANN results, PSO showed that high retention efficiency ultrafiltration could be achieved with the following filtration conditions: a 45.2 nm PCTE membrane combined with 3.4 nm Zi_3N_4 with 36.5 mV zeta potential; a 100 nm PTFE membrane combined with 28.4 nm ZnS with -20.8 mV zeta potential; a 52.2 nm fibrous filter with -20.3 mV zeta potential, 5.5 nm nanoparticles with 41.4 mV zeta potential, and a combined Hamaker constant of 0.09.

Chapter 5. Conclusions and Future Directions

5.1 Conclusions

This research proposed a sustainable filtration strategy to mitigate the high energy consumption from UF system in various industries such as water treatment, food, biomedicine, pharmaceutical, and semiconductor manufacturing. To verify the feasibility, ES-SMPS method was extended to measuring retention efficiency for small nanoparticles in IPA. Theoretical models were then developed to understand ultrafiltration with nanoparticles down to 2.8 nm in organic solvent. The theoretical models were verified by experimental results and could predict retention efficiency very well. Furthermore, to optimize the filtration conditions to obtain the highest efficiency, ANN combined with PSO models were established. The model provides a convenient and effective way for researchers or engineers to design the sustainable filtration system. The detailed conclusions from this dissertation are listed below.

5.1.1 Experimental results

The ES-SMPS system was then used to measure the retention efficiency of ZnS, Au, and PSL particles challenged on different pore sizes of PTFE, PVDF, and PCTE membranes. According to the findings, the retention efficiencies of all three membranes were greater in IPA than in water. Furthermore, the surface electrical enhancement of PTFE demonstrated a comparable or greater efficiency for all four nanoparticle sizes compared to PCTE. Additionally, under all experimental conditions, the highest efficiency was observed with 10 nm Au nanoparticles challenged on a 100 nm rated PTFE membrane, demonstrating the feasibility of the proposed sustainable UF.

5.1.2 Theoretical development

Modifications were made to the filtration models for each specific process. To consider transport efficiency, air filtration models were added. In xDLVO models, Hamaker constant was adjusted to be appropriate for small particles, and the electrical double layer equation suitable for

97

organic solvents was applied. Additionally, the Maxwell model was used to account for detachment due to the high kinetic energy of small particles.

The new models provided insights into the reasons behind the experimental results. Based on the calculation results, it was found that the high efficiency was due to membrane surface electrical enhancement, or an alteration of AB interaction caused by changes of liquid. These findings suggest a potential direction for increasing the retention efficiency.

5.1.3 Machine learning models

This study combined multilayer perceptron artificial neural network (MLP-ANN) with particle swarm optimization algorithm (PSO) to optimize the UF performance. Membrane zeta potential, pore size, particle size and particle zeta potential and Hamaker constant were inputs, and retention efficiency was the output. In addition to the data obtained from the experiments, retention efficiencies for Au, ZnS, SiO_2, Al_2O_3, Si_3N_4, and PSL NPs (Particles commonly found in semiconductor factories) with 5-100 nm in size against 50-200 nm PTFE, PVDF and PCTE membranes were also calculated and used to train, teste and validate the model. The predicted values from ANN model were highly correlated to the target values with R^2 values for training, validation and test dataset were 0.996, 0.992 and 0.962 respectively. PSO model then applied the ANN results to find the optimized combination of the inputs that has highest retention efficiency and lowest energy use. Results showed that an efficiency of 99.9% could achieve by using 3.4 nm Si3N4 (36.5 mV) on the PCTE membrane and 28.4 nm ZnS (-20.8 mV) on the PTFE membrane, respectively. If the membrane or particle type is not pre-determined, the conditions to have a filtration efficiency of 99.9% were 52.2 nm filter with -20.3 mV zeta potential, 5.5 nm nanoparticles with 41.4 mV zeta potential, and a combined Hamaker constant.

5.2 Future Directions

Despite the demonstrated breakthroughs and the contributive work reported in peer-reviewed journals, further work is required with respect to the following aspects:

5.2.1 Fouling experiment

Initial filtration can remove a significant portion of the contaminants, the remaining particles can accumulate on the membrane surface over time, leading to fouling. Membrane fouling is a challenge in the operation and maintenance of membrane-based filtration systems. It has a significant impact on the performance and longevity of the filtration system. Therefore, it is important to study membrane fouling in addition to initial filtration. By understanding the causes and mechanisms of membrane fouling, effective mitigation strategies can be developed to prolong the life of the membrane and improve the efficiency of the filtration process.

Although this research focused on initial filtration, the methodology is very easy to extend to membrane fouling. For the experiment part, it just requires running the experiment longer to ensure particles are loaded on the membrane. For the theories, the interactions will be between particles to particles in the fouling stage instead of particles to membrane in the initial stage. Modifying the parameters of the membrane to the particles can result in changes to the fouling models. With the data from fouling experiments or models, the ANN and PSO models are readily to perform prediction and optimization.

5.2.2 UF in other liquids than water and IPA

Although UF is widely used for water treatment IPA purification applications, it can also be applied to other liquids. For example, in the electronics industry, UF has been used for the recovery of acids and bases from etching solutions, which contain metal ions and other impurities that can

negatively affect the performance of electronic components. By removing the impurities and metal ions, the recovered acids and bases can be reused, reducing waste and cost. However, studies on the retention efficiency of UF under such conditions are relatively scarce. It is relatively straightforward to extend our theoretical or machine learning models to apply to acid or base filtration by utilizing the relevant parameters of the acid or base. The main challenge lies in conducting the necessary experiments to validate the models. Although UF membranes with acid- and base-resistant properties have been developed to withstand the harsh conditions of these solutions. However, the performance of the UF membranes can still be affected by the high acidity or alkalinity of the solutions, and careful consideration must be given to the selection of other experimental components to ensure stability of the UF system.

Appendix I. Additional research on indoor air quality control – Emissions from 3D printing

Chapter A1 A Review of Emission Characteristics and Control Strategies for

Particles Emitted from 3D Fused Deposition Modeling (FDM) Printing

A1.1 Introduction

Due to the increasing cost of making protypes (primarily on labor cost) in traditional machine shops, three-dimensional (3D) printing is being considered to be an alternative to fulfill the task in the consumer and industrial settings [212-215]. The market value for 3D printers has been increased from \$4.4B USD in 2013 to ~\$15B USD in 2021 [216] and is estimated to achieve \$63.46B USD by 2026 [217]. Among various types of 3D printing technology, fused deposition modeling (FDM) owns a lion's share of 3D printing market [218, 219]. FDM 3D printers melt a solid thermoplastic filament by passing it through a heated nozzle and deposit melted filament layer by layer to form a 3D object [220]. During the heating and extrusion, particles in ultrafine ($<$ 100 nm) and fine (< 2.5 μm) sizes and vapors (e.g., semi-volatile organic compounds, SVOCs, and VOCs) are emitted as byproducts [221-223]. The quantity of vapor and particle emissions are depended on the printing conditions and filament materials. The most common filament materials are acrylonitrile butadiene styrene (ABS) and polylactic acid (PLA). Additives are also blended into raw filaments in order either to equip new functions or to enhance the functionality of final objects. Examples of additives include dyes, plasticizers, stabilizers, carbon allotropes, woods, metals, and many others. For instance, metal particles are added in filaments for aesthetic and practical purposes. However, transition metals, e.g., copper and iron, could catalyze the thermal degradation of organic compounds during the printing which contributes to the emission of VOCs and SVOCs [224, 225]. It has been reported that the primary nanoparticles are formed due to homogenous nucleation of the SVOCs and then grow into larger particles through agglomeration and/or the condensation of SVOCs on the surface of primary particles [226, 227]. Therefore, the amount of emitted SVOCs play an essential role in the particle emission of 3D printing.

Particles and VOCs produced in the 3D FDM printing could potentially cause adverse effects on respiratory systems [228-232], stimulate acute hypertension and microvascular dysfunction [233], affect neuroendocrine function [234] and induce toxicological effects of the cells [235]. For example, House et al. [228] reported that a worker experienced heavy chest, shortage of breath and coughing after working with 10 FDM 3D printers in a limited work area of around 3,000 m^3 for 10 days. Farcas et al. [235] found that several serum biomarkers of hepatic and kidney functions in the rats were significantly higher at Day 1 after 4 hours of exposure to ABS-emission. Joob and Wiwanitkit [236] indicated that the risk for carcinogenesis due to the exposure to the emission of 3D FDM printers would be 3.44 times higher than the exposure to urban air pollution. Moreover, Byrley et al. [223] evaluated the deposition of inhaled particles in different regions of the respiratory tract for people at the ages ranging from 3 months to 18 years. Their result suggested that 9-years-old children had an overlap of the highest exposure risk considering total mass deposition and surface deposition by pulmonary surface area. Azimi et al. [221] studied the impact of the emitted VOCs to human health and reported that high lifetime cancer risks could be yielded from the exposure to styrene which was emitted largely by all ABS filaments and the HIPS filament. Davis et al. [222] identified 216 individual VOCs emitted from different filaments including some possible carcinogenic VOCs, such as formaldehyde, styrene, methylene, acetaldehyde and ethylbenzene, reproductive toxic VOC, toluene, respiratory toxic VOCs, such as caprolactam, acetic acid, lactide and methyl methacrylate.

Despite potential evidence of adverse health effects of emitted particles and VOCs during the 3D FDM printing, conclusive solutions to effectively remove the emissions and reduce the emission exposure remain at large. One of the reasons is due to the inconsistency and uncertainty of the emission data reported in literatures. Nevertheless, researchers have all agreed cautions

should be paid to the emission from the 3D printing. Since the first publication revealing that nonnegligible amount of particles and VOCs could emit from the 3D printing in 2013 [237], researchers have been using various methods to characterize the total concentration and size distribution of particles, and concentration and species of VOCs emitted from the 3D FDM printing [238-242].

Up to the present, there are more than one hundred journal articles have mentioned the emissions of the 3D FDM printing. The key words to search these literatures include 3D printing, particle emission from 3D printing, characterizations of particles and VOCs from 3D printing, and exposure from 3D printing. These journal papers were published by Elsevier, ACS publications, Taylor and Francis, Wiley online library, Procedia manufacturing, Springer, Royal society of chemistry, Emerald insight, MDPI, and Bioresources. As our research objectives are to investigate the emission characteristics and effective control methods, seventy-three peer-reviewed papers focused on these two objectives that have reliable measurement results and detailed analysis in major journals were finally chosen.

Fig. A1.1 shows the number of publications by years. The number was increasing from 2013 to 2017 with a short decrease in 2018, but the number was rapidly picking up again after 2018 (Data for 2021 was summarized by August). It is found that studies done prior to 2018 were primarily showing their data using their own measurement methods (i.e., not paying much attention on the standardization of the characterization methods). The intercomparison of reported emission data from different research groups was not possible without having a standard method for the emission characterization. Starting from 2019, researchers realized the above issues and paid their attentions on the development of standard characterization methods (triangle symbol in Fig. A1.1 represents the number of papers) [239-242]. The Underwriters' Laboratories (UL)

published the standard method for assessing particle and vapor emissions from 3D Printers in 2019 [239]. In addition, Chýlek et al. [240] and Sittichompoo et al. [241] proposed the thermogravimetric analysis (TGA) method to characterize the original emission from the filament attempting to validate the data obtained by the conventional chamber methods. Ding et al. [242] noticed the occurrence of measurement error in the chamber measurement was due to the heat accumulation in test chambers and proposed conducting the emission measurement in flow tunnels (overcoming the heat accumulation issue by significantly increasing the air change rate). Unfortunately, these newly proposed methods remain unable to regulate researchers to normalize their measurement data due to built-in variables. For example, the UL standard allows the differences on multiple environmental factors. The measurement by the TGA method cannot represent the emission in real printing. The tunnel method ignored the effect of temperature distribution around a printing nozzle on the emissions.
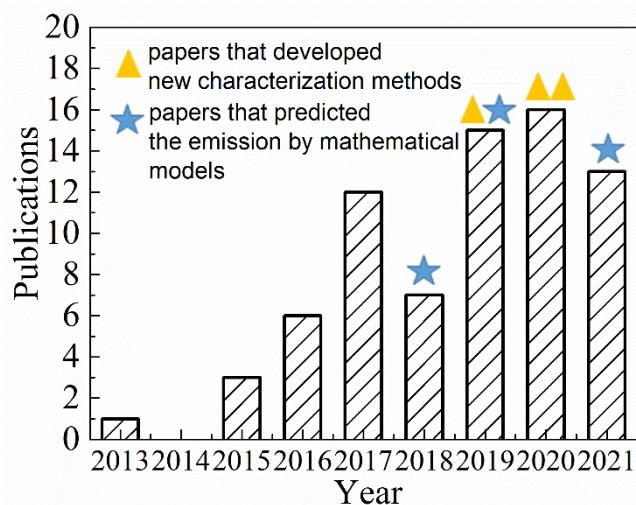
Figure A1.1. Number of publications on the emission of 3D FDM printing.

Not only is a standard emission characterization method/guideline essential to survey the real emission characteristics of 3D FDM printing but also to investigate the factors influencing the

emission level. To have effective control strategies, the identification of influencing factors on the emission from 3D FDM printers at the source level is crucial. Several studies had explained the emission from the source [238, 243-245]. Zhang et al. [238] illustrated the emission process focused on the aerosol dynamics and indicated that factors including filament color, filament brand and filament material may affect the particle emission. Vance et al. [243] and Gu et al. [244] performed various of experiments validating their assumptions on the consistent compositions of emitted particles, filaments, and printed objects. Potter et al. [245] demonstrated the variation of particle emission caused by different filament materials (from the chemical reaction viewpoint). Their investigation contributed to the understanding of the emission characteristic for filaments in raw materials. Unfortunately, the above understanding could not be generalized to the cases using advanced filaments, especially for metal-additive ones. Metal-additive filaments have been found to emit particles in concentration several orders of magnitude higher than non-metal additive filaments. Further investigation of the emission mechanisms in the cases of additive filaments is very desirable. In addition to controlling the influencing factors for reducing the emission at the source level, engineering solutions to trap particles after formed are also important. Control strategies by changing the printing parameters [224, 246, 247], including the ventilation and filtration [248, 249] and controlling the environmental variables [250, 251] have been studied. However, it is challenging from these studies to reach final conclusions guiding end users to select the most effective control method (due to the difference in the evaluation methods). A large amount of emission data obtained from the same experimental setup are required to achieve the above objective. However, it is very costly and time-consuming to obtain all the required emission data by experiments.

Prediction models are alternatives to resolve the above concerns. Zhang et al. [226] developed a lognormal moment model to predict the particle formulation and transient size distributions of formed particles. Zontek [252] combined the eddy diffusion model and Monte Carlo simulation (as shown in Fig. A1.1) to predict the particle emission. Their results showed good performance of the models and perceptive insights of the emission characteristics. Taking a different route, the models developed by the machine learning have also been explored to effectively resolve the time-consuming issues encountered in the prediction and optimization via mechanistic models [253-255] if enough data with high quality are available. Many studies have been applying the machine learning in additive manufacturing [256-261], but limited ones have focused on the relationship between the emission and printing conditions.

Up to the present, many studies regarding the emission characteristics of 3D FDM printers have been published. A comprehensive review of these existing studies would be very desirable to provide journal readers/researchers a clear picture on the status of current study on the emission from 3D FDM printers and to identify the areas/directions required for further studies. Various emission characterization methods, emission mechanisms, and control strategy as well as on the optimization of printing parameters targeting on the emission control are reviewed and discussed in the following sections. Table A1.1 summarizes the experimental setups, measurement conditions and emissions of a 3D FDM printer reported by the existing publications.

Table A1.1 Summary of measurement methods and data from different references

	Study	Measure-ment place	Volume (m³)	Ventilation (h⁻¹)	Main measurement equipment	Sampling point	Filament material	Filament brand	Filament color	Printer	Printing temp (°C)	Bed temp (°C)	Printing object	Printing time	Emission rate (#/min)	Geo Mean
1	Kim et al., 2015 [262]	Chamber 1	0.561		SMPS, 10-420 nm	Upper part of the chamber	PLA-1	-	Brown	Cube, 3D System	210-220	-	Bobbin	2h 30 min	4.89×10^8	27.9
							PLA-2	-	-	3DISON Plus, Rokit	210-220	-	Bobbin	1h 55 min	4.27×10^8	188.2
							ABS	Rokit	Red	Cube, 3D System	250	-	Bobbin	2h 50 min	1.61×10^{10}	32.6
2	Azimi et al., 2016 [221]	Chamber 3.6	1		CPC, 10-1000 nm	Exhaust port	PLA	-	Red	FlashForge Creator	200	110	NISTpart	3h 42 min	1.05×10^8	-
							PLA	-	White	Dremel 3D Idea Builder	230	-	NISTpart	2h 49 min	1.10×10^8	-
							PLA	-	Red	LulzBot Mini	190	45	NISTpart	3h 25 min	1.00×10^8	-
							ABS	-	White	FlashForge Creator	200	110	NISTpart	3h 42 min	4.00×10^{10}	-
							ABS	-	Blue	XYZprinting da Vinci 1.0	230	100	NISTpart	2h 26 min	1.10×10^{10}	-
							ABS	-	Red	LulzBot Mini	240	110	NISTpart	2h 33 min	9.00×10^{10}	-
							ABS	-	Red	LulzBot Mini	240	110	Cube	2h 42 min	8.90×10^{10}	-

#	Author	Location			Instrument	Distance	Material		Color	Printer	Nozzle	Bed	Method	Time	Concentration	
							ABS	-	White	MakerBot Replicator 2X	230	110	NISTpart	2 h 38 min	8.00×10^{10}	-
							HIPS	-	Black	LulzBot Mini	240	100	NISTpart	2 h 28 min	4.00×10^{9}	-
							Nylon	-	Bridge semitransparent	LulzBot Mini	230	65	NISTpart	2 h 55 min	2.00×10^{8}	-
							Laybrick	-	White	LulzBot Mini	200	65	NISTpart	3 h 0 min	6.00×10^{7}	-
							Laywood	-	Brown	LulzBot Mini	200	65	NISTpart	3 h 2 min	8.00×10^{7}	-
							Polycarbonate	-	Transparent	LulzBot Mini	270	110	NISTpart	2 h 38 min	4.00×10^{10}	-
							PCTPE	-	Semitransparent	LulzBot Mini	235	65	NISTpart	3 h 2 min	2.00×10^{10}	-
							T-Glase	-	Transparent red	LulzBot Mini	240	60	NISTpart	3 h 2 min	5.00×10^{9}	-
3	Yi et al., 2016	Chamber (a small room)	0.5	3	SMPS, 10-360 nm	10 cm from the printer	PLA	-	Army green		215	off		14 min	1.28×10^{10}	32.4
							PLA	-	True red	Replicator 2x	215	off	Comb	14 min	1.25×10^{10}	28.3
							PLA	-	Ocean blue		215	off		14 min	1.13×10^{10}	27.5

#	Study	Chamber			Instrument	Location	Material		Color	Printer	Temp1	Temp2	Geometry	Time	Concentration	
	[263]						PLA	-	Transparent blue		215	off		14 min	1.56×10^{10}	30.1
							ABS	-	Natural		230	110		14 min	1.62×10^{10}	70.1
							ABS	-	Red		230	110		14 min	1.35×10^{10}	70.2
							ABS	-	Blue		230	110		14 min	7.43×10^{9}	78.9
							ABS	-	Black		230	110		14 min	1.05×10^{10}	44.6
							PLA	-	Yellow						0.10×10^{8}	-
							ABS	-	Red						2.70×10^{8}	-
							PVA	-	-						1.20×10^{10}	-
4	Floyd et al., 2017 [264]	Chamber	0.0248	16.2	SMPS, 16.8-532.8 nm	right side the printer	HIPS	-	White	Aworldnet A600	210	70	University of Oklahoma Logo	1h 15 min	0.50×10^{8}	-
							PCABS	-	White						6.00×10^{8}	-
							Nylon	-	-						1.20×10^{8}	-
							Bronze-PLA	-	-						3.90×10^{9}	-
							PET	-	-						2.60×10^{8}	-
5		Chamber	1	1			PLA	b	Red, white	A	210	-		-	-	16.8

			PLA	c	Red, white	A	210		-	38.9
			PLA	f	Red, white	A	210		-	63.2
			PLA	b	Red, white	B	215		-	50.6
			PLA	c	Red, white	B	215		-	49.5
			PLA	f	Red, white	B	215		-	35.4
			PLA	b	Red, white	C	230		-	27.9
Zhang et al., 2017 [238]	SMPS, 7-300 nm	10–20 cm from the printer.	PLA	c	Red, white	C	230	Extrusion	-	31.2
			PLA	f	Red, white	C	230		-	28.1
			ABS	a	Red, white	A	270		-	98.6
			ABS	c	Red, white	A	270		-	90.4
			ABS	d	Red, white	A	270		-	40.7
			ABS	f	Red, white	A	270		-	103.0
			ABS	a	Red, white	C	260		-	92.0
			ABS	c	Red, white	C	260		-	118.3
			ABS	d	Red, white	C	260		-	66.0
			ABS	f	Red, white	C	260		-	99.2

						Nylon	e	Nature	A	243				-	129.4
						PLA	-	Red		220	60		65 min	3.61×10^8	57.2
						ABS1	-	light gray		230	120		78 min	3.28×10^{10}	45.6
						ABS2	-	dark gray		240	110		73 min	2.14×10^{10}	58.0
						PVA	-	yellow-brown	3DISON multi 2	190	60		64 min	8.12×10^8	68.0
6	Kwon et al., 2017 [248]	Chamber 2.5	Vary	SMPS, 10-420 nm	2.3 m from the printer	Laywood	-	brown		215	60		64 min	4.65×10^8	59.4
						HIPS	-	white		265	90	Cylindrical object	70 min	3.37×10^{11}	31.5
						Nylon	-	semitransparent		265	90		70 min	3.27×10^{11}	21.8
						ABS1	-	light gray						1.98×10^{11}	43.0
						ABS2	-	dark gray						1.89×10^{11}	45.2
						PLA	-	Red		265	90		70 min	6.82×10^{10}	27.2
						PVA	-	yellow-brown						1.42×10^{11}	85.2
						Laywood	-	brown						6.93×10^{11}	30.0
7		Chamber 0.52			-	PLA		Light blue	Afinia 3D	200-210	50		63min	1.48×10^{10}	22.0

	Reference	Chamber			Measurement	Material	Printer	Color	Temp		Object	Time	Concentration	
						Copper-infused PLA		-	190-240	50		63min	1.10×10^8	28.0
	Vance et al., 2017 [243]	2.45/0.18		SMPS, 14.6-680 nm		Wood-infused PLA	Afinia 3D	-	190-240	50	NIST artifact, scaled 50% size	63min	1.58×10^8	470
						Value-line ABS		Orange	210-250	90		63min	1.08×10^{11}	51.0
						Premium ABS		Yellow	260-270	90		67min	1.25×10^{10}	51.0
						PLA-1			200	70			6.00×10^8	-
						PLA-2			230	70			3.12×10^{11}	7.9
8	Mendes et al., 2017 [246]	Chamber (a test room)	0.18	280	SMPS 2-350 nm	outlet of the chamber	ABS-2	Mini	-	-	230	90	a small object	60 min	8.40×10^{10}	7.9
						ABS-4	Factory Oy		250	90			1.32×10^{12}	10.5
						ABS-1a			230	90			2.22×10^{10}	8.8
						ABS-1b			230	90	-	-	3.72×10^{11}	15.5

No	Reference				Instrument	Location	Material	Brand	Color	Printer	Nozzle	Bed	Model	Time	Concentration	Size
9	Cheng et al., 2018 [247]	Chamber	0.366	-	HPC 300-2500 nm	air outlet	ABS	Voltivo	Red	Flash Forge	240	110	elephant, hemisphere, and pyramid models, rectangular blocks	-	-	-
10	Stefaniak et al., 2017 [265]	Chamber	12.85	1	FMPS, 5.6-560 nm	mixing well	PLA	3DXStat ESD	black	LulzBot	220	65	NIST model	-	8.07×10^9	21.6
							PLA-CNT	F-Electric	black		220	65			4.90×10^9	21.7
							ABS	3DXTech	black		240	110			7.60×10^{11}	22.7
							ABS-CNT	3DXTech	black		240	110			3.66×10^{10}	32.8
							PC	Gizmo Dorks	black		290	100			2.96×10^{11}	47.5
							PC-CNT	3DX Tech	black		290	100			3.26×10^{11}	25.2
11		Chamber	3	1/1.5			ABS		Blue	Zortrax	275	80		4 h	3.80×10^{10}	27.0

			ABS		Green		275	80		4 h	4.30 x 10^{10} 30.0
			ABS		Grey		275	80		4 h	6.50 x 10^{10} 27.0
			ABS		Red		275	80		4 h	4.10 x 10^{10} 28.0
			ABS		Red		275	80		4 h	4.50 x 10^{10} 30.0
			ABS		Red_230		230	80		4 h	4.20 x 10^9 31.0
			ABS		Red_240		240	80		4 h	8.30 x 10^9 29.0
Gu et al., 2019a [222]	FMPS, 5.6-560 nm	mixing well	ABS	Zortrax/3 Dmensio nals/Pont ialis GmbH	Red_250		260	80	90% NIST	4 h	2.30 x 10^{10} 29.0
			ABS		Red_260		260	80		4 h	1.30 x 10^{11} 24.0
			ABS		White		275	80		4 h	2.90 x 10^{10} 27.0
			Ultra-T		Ivory		260	80		4 h 6 min	1.40 x 10^{11} 24.0
			ASA		Blue		254	90		4 h 18 min	1.70 x 10^{11} 24.0
			PETG		Black		254	30		4 h 18 min	9.70 x 10^9 59.0
			ESD		Black		280	70		3 h 30 min	6.50 x 10^{10} 30.0

Reference	Method			Instrument	Distance	Material	Color	Printer	Temp 1	Temp 2	Geometry	Time	Emission	
						GLASS	Transparent		254	30		4 h	2.00 x 10^9	82.0
						HIPS	Yellow		255	80		4 h 6 min	3.30 x 10^9	41.0
						PCABS	Ivory		290	105		3 h 54 min	7.03 x 10^{10}	32.0
						PLA	Green		200			60 min	1.08 x 10^6	-
						PLA polyplus	True green		200			60 min	1.53 x 10^6	-
						PLA Silver	Silver metallic		200			60 min	3.8 x 10^6	-
Chýlek et al., 2019 [240]	Chamber	0.0577	0.3	SMPS, 583 nm	16.5-583 nm; 10 cm away from the nozzle	ABS	Traffic red		230		A simple cylindrical geometry	60 min	1.13 x 10^9	-
12						Polywood -	Light Wood	Ultimaker 3 Extended	200	-		60 min	1.53 x 10^6	-
						PVA	Natural		215			60 min	3.25 x 10^6	-
						Breakaway	White		225			60 min	7.17 x 10^6	-
						Polyflex	Black		223			60 min	8.41x 10^6	-
						CPE	Light grey		240			60 min	3.26 x 10^8	-

No.	Reference	Chamber		Instrument	Location	Material		Color	Printer	Temp	Bed	Object	Time	Concentration	
						PC		Black		260			60 min	1.84 x 10^9	-
						Nylon		Black		245			60 min	3.46 x 10^9	-
						ASA		Green grass		250			60 min	5.89 x 10^9	-
13	Ding et al., 2019 [227]	Chamber 0.384	-	SMPS, 10-420 nm	-	PLA2				200			30 min	4.70 x 10^9	-
						ABS1				220			50 min	2.50 x 10^9	-
						ABS1	-	-	-	240	-	Extrusion	45 min	1.25 x 10^{10}	-
						ABS1				260			48 min	4.75 x 10^{10}	-
						PVA2				220			10 min	3.90 x 10^{10}	-
14	Gu et al., 2019b [266]	Chamber 30	0.5	FMPS, 5.6-560 nm	-	ABS	-	Red	Zortrax	275	80	90% NIST	4 h	-	-
15	Jeon et al., 2020 [267]	Chamber 2.5	36	SMPS, 10-420 nm	Outlet	PLA		Snow-white		215			136 min	3.40 x 10^8	-
						ABS		Snow-white		245	90		134 min	1.50 x 10^{10}	-
						Laywood	-	Brown	3DISON Multi	215		a cube	135 min	2.40 x 10^9	-
						Nylon		Snow-white		245	-		135 min	4.01 x 10^9	-

						PLA	Ultimaker	Ultimate Blue		210	60		36 min	4.75×10^9 13.4
	Poikkimäki et al., 2019 [224]	Chamber 0.3	20	SMPS, 4-573 nm	Right side of the chamber	PLA	colorFabb	woodFill		210	60		36 min	8.86×10^{11} 23.8
16						PLA	colorFabb	copperFill	Ultimaker B.V.	220	60	A frog	36 min	1.73×10^{12} 9.8
						ABS	Ultimaker	Red		240	90		36 min	1.17×10^{10} 13.3
						nGEN	colorFabb	-		220	80		36 min	1.61×10^{10} 13.35
						CNT25	25% CNT							
17	Dunn et al., 2020a [268]	Chamber 0.34	-	SMPS, 10-420 nm/FMPS, 5.6-560 nm	exhuast duct	1KHFC30	30% CNF	-	-	-	-	-	-	-	-
						1KHFZ	10% CNF							
						1AR2	proprietary filament							

#	Reference	Chamber			Instrument	Location	Material		Color/Type	Printer	Nozzle °C	Bed °C		Time	Emission	
							PEEK	unfilled polyetheretherketone								
18	Byrley et al., 2020 [223]	Chamber 2	1		SMPS, from 15.1	20 cm from the chamber wall and 20 cm from the extruder head	pulverized PLA		White	-	180	-	-	40 min	5.60 x 10^10	-
							PLA pellets		Semitransparent		180			51 min	1.70 x 10^9	-
								-								
							ABS pellets		Semitransparent		180			51 min	3.50 x 10^11	-
19	Dunn et al., 2020b [269]	Chamber	0.22	322	SMPS, 10-420 nm	outlet of the chamber	PLA		True orange	Replicator+				2 h	7.10 x 10^6	62.3
							IMPLA	-	Slate Gray impact resistant	Replicator+	-	-	-	2 h	8.17 x 10^9	45.6
							ABS		True yellow	Replicator 2X				2 h	2.83 x 10^9	53.6
			0.45				IMPLA		Slate Gray	Replicator Z18				-	1.40 x 10^10	49.6
20		Chamber -	1		-		ABS	-	White	-	230	110	-	-	4.80 x 10^8	36

120

No.	Reference	Environment			Instrument	Distance	Material	Brand	Color	Printer	Nozzle temp	Bed temp	Model		Concentration	Size
	Sitticho mpoo et al., 2020 [241]				SMPS, 7.77-273 nm		ABS		Orange		230	110			9.00×10^8	36
21	Alberts et al., 2021 [225]	Chamber	0.028	0	FMPS, 5.6-560 nm	30 cm from the top of the chamber	PLA	IGN	White		220	50			1.64×10^6	57.2
							PLA-Cub	ColorFab	Cu-additive		220	50			4.43×10^7	22.7
							ABS	Verbatim	transparent	Type A Machines	240	80	Puck	-	2.06×10^7	29.7
							ABS-W	Tuner MedTech GMASS	tungsten-additive		240	80			3.05×10^8	26.7
22	Ding et al., 2020 [242]	Chamber	1900/1/1	3 (1,5)	SMPS, 10-420 nm	0.5 m from the printer	PLA1	Ecomaylene	Natural		220	50			-	-
							ABS1	Esun	natural	UP Plus 2	260	90	Cube	-	4.00×10^9	35.0
							ABS2	Polymaker	white		260	90			7.00×10^9	39.0
							ABS5	Esun	white		260	90			1.90×10^{10}	30.2

#	Reference	Chamber		Instrument	Location	Material	Manufacturer	Color	Printer	Nozzle (°C)	Bed (°C)	Object	Time		Value
						ABS6	Ecomaylene	white		260	90				2.90×10^{10} 29.3
						ABS7	Ecomaylene	black		260	90				2.50×10^{10} 25.0
						PVA1	OEM	yellow		220	50				8.50×10^{10} -
23	Bernatikova et al., 2021 [270]	Chamber 0.29	0	SMPS, 10-420 nm	next to the 3D printer	PETG	Filament PM	orange	PRUSA i3	245	75	cube-shaped block	1 h	-	86.4
						NGEN	Prusa Research	orange		230	85		1 h 21 min	-	115.5
24	Wojnowski et al., 2021 [271]	Chamber 0.13	-	CPC >2 nm	-	PLA standard	Print-Me	natural	Prusa i3	220	60	Cube	5 min	-	-
						PLA premium	Nebula	natural		220	60		5 min	-	-
						ABS	Nebula	natural		235	60		5 min	-	-
						PETG	Print-Me	natural		235	60		5 min	-	-

#	Reference	Location			Instrument	Position	Material			Printer	Temp			Object	Time	Concentration	
25	Stephens et al., 2013 [237]	Office	45	-	SMPS, 10-420 nm	2 m away from the nearest printer	PLA	-	-	-		200	18	Frog and chain link	20 min	2.00×10^{10}	-
							ABS	-	-	-		220	118		20 min	1.90×10^{11}	-
26	Stabile et al., 2017 [272]	Room	40	0.22	SMPS 6-220 nm	2 m from the printer	PLA			Prusa i3	220					6.78×10^{9}	-
							PLA wood 1			Prusa i3	220					5.77×10^{10}	-
							PLA wood 2			Prusa i3	230					1.91×10^{12}	-
							PLA copper	-	-	Prusa i3	220		-	Minion Dave	40 min	1.98×10^{12}	-
							PLA bamboo			Prusa i3	220					1.47×10^{11}	-
							PLA felx			Prusa i3	240					4.18×10^{10}	-
							CP			Prusa i3	220					1.68×10^{11}	-

No.	Reference	Location			Instrument	Distance	Material		Color	Printer	Temp 1	Temp 2	Print time	Shape	Emission	
—							CP-carbon fiber			Prusa i3	220					2.31×10^{11}	-
							Nylon			Prusa i3	220					-	-
							Ninjaflex			Prusa i3	220					-	-
27	Katz et al., 2019 [273]	Small office	46.4	1.9-4	SMPS, 14.6-685.4 nm	1.5 m from the printer	PLA	-	-	AFINIA-H800	210	50	3h 30 min	Block	3.67×10^{9}	-
							ABS				260	90	5h 18 min		6.92×10^{10}	-
28	Viitanen et al., 2021 [249]	Office room	48.3	vary	SMPS, 10-420 nm	Vary	ABS	-	Red	miniFactory Oy	240	95	-	24-54 min	-	-
29	Zhou et al., 2015 [274]	A ten thousand clean room	60	-	Grimm 1109, 250-32000 nm	Vary	ABS	-	Green/White	-	220	-	Robbot	60-117 min	-	-

#	Reference	Location			Particle counter	Printer position	Material		Color	Printer			Object	Print time		
30	Steinle, 2016 [275]	Chamber /(large lab, small office)	0.85	16	ASM, 180-20000 nm/EDB) and miniDiSC, 7-400 nm	On the top of the chamber	PLA	-	Yellow	Cube 2nd generation, 3DSystems	-	-	Boiled egg cup with chicken feet	2h 45 min	-	-
							ABS	-	Yellow		-	-		2h 45 min	-	-
31	Deng et al., 2016 [276]	Clean room	8	60	CPC (2.5 - 1000 nm)	-	PLA	-	Black	FlashForge Creator	200	60	Make robot	-	-	-
							ABS	-	Red		220	110		-	-	-
32	McDonnell et al., 2017 [277]	Office/3D Printing Club Space/Library/ Dorm Room/Lab	vary	vary	P-trak 20-1000 nm	Close to the printing bed	PLA ABS Nylon Polycarbonate	-	-	-	-	-	-	-	-	-

No	Reference	Location			Instrument	Position	Material		Printer						Time	
33	Bharti and Singh, 2017 [278]	Library	-	-	P-trak 20-1000 nm	-	PLA	-	-	-	210-215	-	-	-	at least 10 min	-	-
34	Preez et al., 2017 [279]	Two different rooms	66/40	no	P-trak 7-1000 nm	less than 10 cm from the printers	ABS - PC - PLA - ultem -		Stratasys/3D Printing Systems (industrial scale)	-	-	-	-	-	-	-	-
35	Youn et al., 2019 [280]	3D printing center	126	no	SMPS, 11-350 nm	-	-	-	white	FINTBOT Z420	230	80	-	-	-	-
36	Setyawati et al.,	Six printing centers	56-666.4	135-613	SMPS, 10-420 nm/FMPS, 5.6-560 nm	Close to the printer or	Vary	-	-	-	-	-	-	-	-	-

#	Reference	Setting	Value		Instrument	Position	Material		Color	Printer	Nozzle T	Bed T	Object	Print time		
	2020 [281]	in the office														
37	Chan et al., 2020 [282]	university 3D printing facility	13.824	-	SMPS, 10-420 nm	in the room or adjoining hallway of the 3D printers	PLA	-	-	MakerBot Replicator 2	-	-	A small objects	< 3 h	-	-
38	Khaki et al., 2021 [283]	family sized living room	41	-	OPS <300 nm	1 m away from the printer	PLA	-	Black	Creality Ender-3	235	80	Cube	~15 min	-	-
							ABS	-	Black		205	50		~20 min	-	-
39	Ding and Ng, 2021 [284]	An office/3D printing laboratories	15	-	SMPS, 10-420 nm	0.5 m away from the printer	PLA			MEX	220			25 min		
							ABS	-	-		260	-	-	25 min	-	-
							PVA				260			25 min		

* The emission rates were captured from the graphs using GetData 2.5 for paper of Azimi et al., 2016 [10], Sittichompoo et al.,2020 [30] and Ding et al., 2020 [31]

A1.2 Formation and dynamic processes of particles

Fig. A1.2 illustrates the mechanisms involved in the particle formation and growth during the 3D printing. Due to the heating of filaments, condensable vapors are generated through the vaporization of filament materials. In this stage, a significant amount of VOCs including condensable SVOCs are emitted. When these SVOCs travel away from the heated printing head, the particle nucleation occurs once the temperature drops and SVOCs become supersaturated [285]. Both homogeneous and heterogeneous nucleation are possible, depending on the additives in the filaments and existence of background particles. At a high concentration of SVOC vapors, particles are nucleated first as a cluster with the sizes exceeding critical values. They then grow sizes by both the vapor condensation and particle coagulation. By the condensation, the rate of particle size growth depends on the vapor saturation condition, chemical composition, and production rate of SVOC, and nucleated particle sizes (relative to the mean free path of ambient air, i.e., the average distance traveled by a molecule between successive collisions) [286]. When nucleated particles are smaller than the mean free path, the size growth is by random collisions of SVOC molecules. The growth of nucleated particles bigger than the mean free path depends on the rate of diffusion of SVOC molecules to the particle surface. In addition to the vapor condensation, the coagulation among particles is also an important mechanism to grow the particle sizes. It should be noted that there is no clear time boundary for condensation and coagulation. Condensation can happen once the size of the nuclei reach the critical size and coagulation happens all the time as it is essentially caused by the particle Brownian motion.
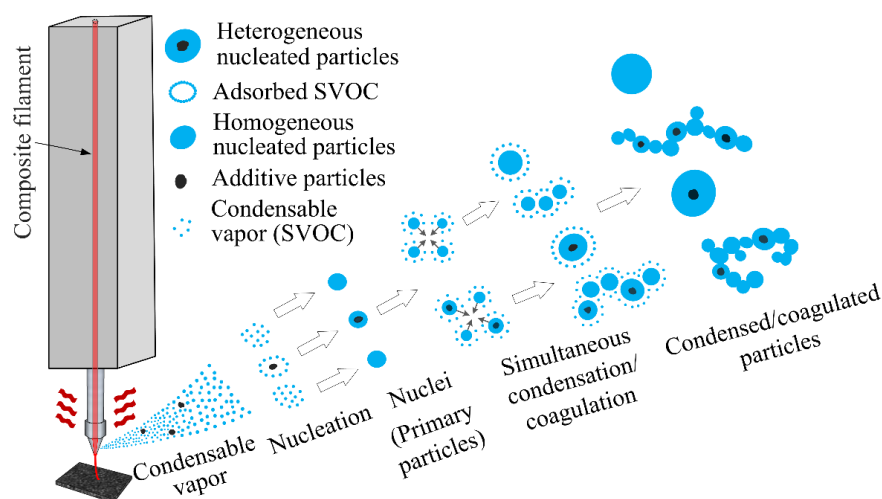
Figure A1.2. Schematic of particle formation and growth process during the 3D printing.

A1.3. Particle measurement methods

A1.3.1. Traditional methods

The characterization of the emission from a 3D FDM printer was performed using test chambers in three different scales: one type of test chambers was in a small scale, i.e., enclosing a printer in a down-sized chamber (Ref. No. 1-24 in Table A1.1); another type was in a single real room (No. 25-28); the last was either in a large space or in multiple real rooms (No. 29-39). Small test chambers were popularly utilized for the emission studies because of its relatively low cost, easy installation, and small footprint in the laboratory settings [287]. For example, down-sized chambers were recommended in the standard to measure particle emissions from a laser printer [288]. However, a standard for characterizing the emission from 3D FDM printers was not found. In the literature, the air change rate, sampling instruments and location were varied in different studies. Unfortunately, the above variables have influential effects on the measured emission data for a 3D FDM printer. For the air change rate, it affects both the flow and temperature fields inside test chambers, resulting in the spatial variation of the particle formation and transport in chambers. The variation of temperature distribution in a test chamber directly influences the emission types and amount of SVOCs, which can be

condensed on particles, thus contributing to the spatial variation of total concentration and size distribution of particles. Low air change rates would minimize the temperature decrease in the proximity to the printing nozzle. The accumulation of emitted particles in a small test chamber was however found by Ding et al. [242] when the air change flow rate was set low. Thus, the authors took the emission measurement by placing a 3D FDM printer in a flow tunnel with an increased airflow around the printing nozzle to eliminate the heat accumulation [242]. However, the temperature change due to the change of air flow rate was not considered. To be able to obtain more realistic emission data, the above study proposed to apply a unit-specific air change rate, which is an equivalent air flow rate ensuring an approximate temperature gradient around the nozzle as that in the real printing condition.

For the sampling instruments, Scanning Mobility Particle Sizers (i.e., SMPSs equipped with a long differential mobility analyzer, DMA, TSI Inc., Shoreview, MN) having the scanning size range from 10 to 700 nm, and Fast Mobility Particle Sizers (FMPSs, TSI Inc., Shoreview, MN) having the measurable size range from 5.6 to 560 nm were widely used for characterizing the size distributions of emitted particles. However, Poikkimäki et al. [224] pointed out that the 3D FDM printing also emitted a large amount of nanocluster particles (< 3 nm). Therefore, the data obtained by SMPSs/FMPSs could underestimate the total concentration of emission particles. Nano SMPS (equipped with nano-DMA) can scan the size of particles from 2 to 150 nm, but the upper size limit is too low to capture the peak size of emitted particles after they grow at a later stage of printing [262]. Obviously, two sets of SMPSs (one set equipped with a long DMA and the other set with Nan-DMA) are required to cover a wide size range encountered in the characterization of particles emitted from a 3D FDM printer. The measuring cycle of a SMPS is also a concern for the characterization of emitted particles in the size range of 10 - 420 nm (~ 1 minute) comparing the dynamic change of particles emitted from filaments of some kinds, which is estimated within 10-15 seconds (according to the

natural convective flow driven by the high temperature of nozzle and heating elements). The measuring time is not a concern for a FMPS because of the use of multiple electrodes in the sizing column providing a size distribution in a second. However, the data collected by a FMPS has found to underestimate the concentration of particles with the sizes greater than 200 nm and overestimate the concentration of particles with the size less than 10 nm [289, 290]. Thus, multiple instruments covering different size ranges and sizing resolutions shall be applied to better characterize the particle emission from a 3D FDM printing. Data collected under different sizing resolutions can also be analyzed to accurately capture the particle dynamics.

The variation of the sampling locations selected in different studies is also contributing to the discrepancy of data. The sampling location would not affect the measurement data if particles and air were well mixed. However, when the sampling location is adjacent to the nozzle, the movement of the nozzle and cooling fan could disturb the surrounding airflow, resulting in spatial variation of temperature and flow around the sampling probe. Cheng et al. [247] found that disturbed air flow next to the sample probe contributes to the fluctuation of measured data. The above issue could be resolved by locating the sampling location away from the printing nozzle. Unfortunately, newly formed particles would not be detectable in the above sampling location.

A1.3.2. Proposed new sampling inlet and measurement criteria

In the consideration of the printing assembly as a point heat source, a conceptual annular sampler as shown in Fig. A1.3 could be a good candidate for the emission measurement. Usually, a cooling fan blowing ambient air (with lower temperature than that near the nozzle) on the nozzle is equipped with the printer to protect the nozzle from overheating. Thus, this flow serves as a trigger for particle nucleation and condensation. If the sampler encloses the cooling fan, which is not only beneficial to have instantaneous and evenly distributed particle

sampling but also remaining a realistic condition. In addition, with an annular inlet of the sampler spatially uniform sampling can be achieved reducing the variability of the particle samples.
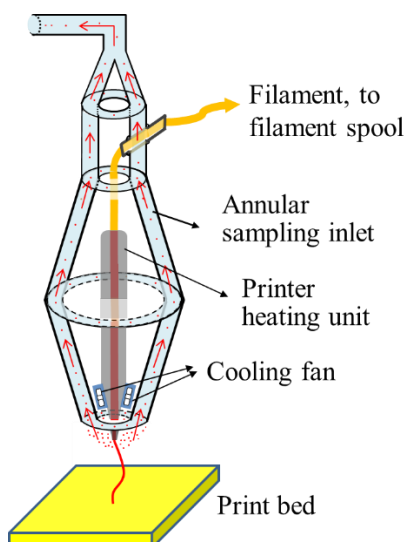
Figure A1.3. Schematic diagram of an annular sampling probe.

In addition to the concerns discussed above, the characterization of particles emitted from a 3D FDM printer shall also satisfy the basic requirements listed in the following:

- 1 m^3 of the test chamber volume is suggested because it is the most used to test the emission from laser printers (for the purpose comparing with laser printer data) [288, 291, 292].

- The material of the chamber should be conductive to minimizing the particle loss due to the electrostatic effect [238, 275, 286, 293]. Frequently cleaning the chamber wall to remove the deposited particles and SVOCs is also required to minimize the outgassing [265, 275].

- The sealing of the test chamber shall be examined. The concentration of background particles should be controlled at the level as low as possible, e.g., less than 200 #/m^3, for minimizing its influence on the particle formation and emission [242, 266].

- The temperature and humidity in the test chamber should be kept at 20-25 °C and 40-

50%, respectively (close to that of a typical indoor environment) [288].

- Sampling tubes should also be conductive and kept as short as possible to reduce the particle loss due to the diffusion [238, 275, 286, 293].

- Type, color, brand, composition (if possible) of filaments should be specified [294].

- For a 3D FDM printer, the printing nozzle assembly design, printing temperature, filament feeding speed, infill percentage, cooling fan speed, printing time and printed objects should be documented [293].

A1.4. Particle emission characteristics

A1.4.1. Emission rate and geometrical mean diameter of common filaments

　　PLA and ABS filaments are the most used feedstock in the 3D FDM printing. Studies have extensively investigated the particle emission from the 3D printing using filaments of these materials (under various printing conditions). Fig. A1.4 graphically summarized the emission rate and geometrical mean diameters (GMDs) of particles emitted from the printing using PLA and ABS filaments in all chamber experiments. For comparison, the same figure also includes the emission data averaged from the printing using filaments of other 20 kinds.
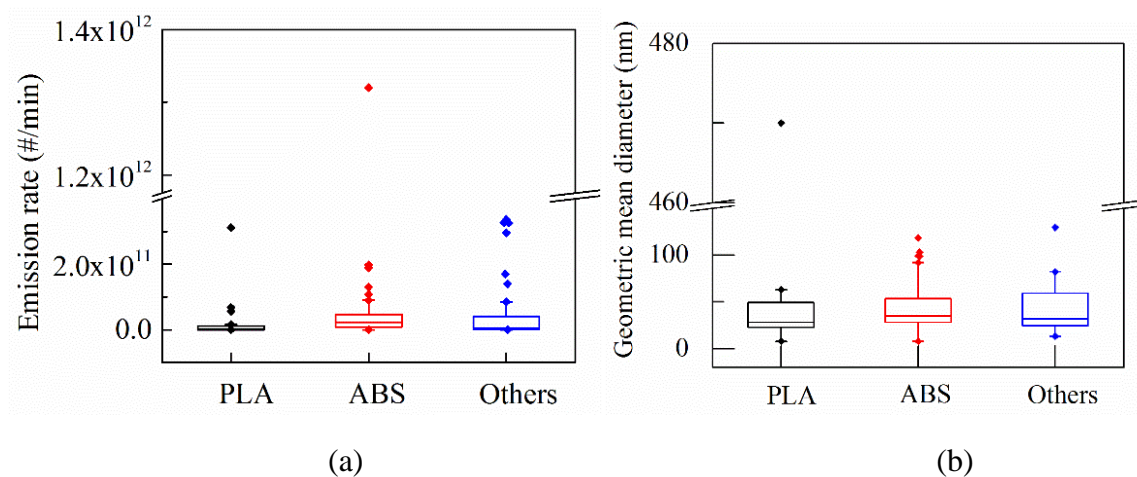

(a)　　　　　　　　　　　　　　　　(b)

Figure A1.4. Emission rate (a) and geometric mean diameter (b) of particles emitted from the 3D FDM printing with different filaments. The maximum of the box is 1.5 times of interquartile range (IQR), the minimum of the box is -1.5 times of the IQR, the top line of the box is the

75th percentile, middle line is the median and the bottom line is the 25th percentile. The rhombus represents outliers. PLA stands for polylactic acid, ABS stands for acrylonitrile butadiene styrene, Others include high impact polystyrene (HIPS), Nylon, Laybrick, Laywood, Polycarbonate, plasticized copolyamide thermoplastic elastomer (PCTPE), transparent polyester resin (T-Glase), Polyethylene terephthalate (PET), PolyVinyl Alcohol (PVA), Acrylonitrile butadiene styrene+0–3% polycarbonate (ULTRAT), Acrylonitrile styrene acrylate (ASA), Polyethylene terephthalate glycol (PETG), PETG+carbon-based conductive additives (ESD), 80% PETG+8–12% fiber glass filings (GLASS), Polywood, Breakaway, Thermoplastic Polyurethane (TPU), Copolyester (CPE), Acrylonitrile Styrene Acrylate (ASA), nGEN (a polyester filament), carbon fiber-filled styrene-free copolyster (CP-carbon fiber).

As evidenced in Fig. A1.4a, many outliers are shown in the cases of different filaments (i.e., PLA, ABS or Others), which could be the data obtained under significantly different measurement conditions. For all the feedstocks, the printing with ABS filaments emitted the highest number of particles per unit time while the printing with PLA filaments emitted least number of particles per unit time. The median emission rates in the cases printing with ABS, PLA and other filaments were 2.2×10^{10}, 6.0×10^{8} and 3.9×10^{9} #/min, respectively. The values of reported emission rate were mostly within the 25th percentile and median value for all kinds of filaments, i.e., from 8.3×10^{9} to 2.2×10^{10} #/min for ABS, from 1.0×10^{8} to 6.0×10^{8} #/min for PLA and from 3.3×10^{8} to 3.9×10^{9} #/min for other filaments.

Figure 4b illustrates the GMDs of particles emitted from the printing with different filaments. The IQRs of GMD are wider than that of emission rates, indicating that the size distributions of emitted particles are very dispersive. The largest median GMD was 35.0 nm and found in the cases with ABS filaments. Particles with GMDs of 31.8 and 29.2 nm were found in the cases printing other and PLA filaments, respectively. The majority of collected

GMD data were in the range between the 25th percentile and median, i.e., from 28.0 to 35.0 nm for ABS, from 23.8 to 29.2 nm for PLA and from 24.9 to 31.8 nm for other filaments.

A1.4.2. Emission characteristics of metal-additive filaments

It should be noted that the data for the cases printing with metal-additive PLA and ABS filaments are not included in Fig. A1.4. The emission rates in the cases printing with metal-additive filaments were at least one order of magnitude higher than those from the printing with original or other additive filaments. Poikkimäki et al. [224] showed that the emission rate for PLA Cu additive and PLA original filaments was 1.7×10^{12} and 4.8×10^9 #/min, respectively. Alberts et al. [225] reported that PLA Cu additive filaments emitted 4.4×10^7 #/min compared to 1.6×10^6 #/min in the cases of PLA original. The printing with ABS W (Tungsten) additive filaments emitted 3.1×10^8 #/min compared to 2.1×10^7 #/min in the printing with ABS original filaments. Even without metal additives in the filaments, the reported emission rates shown in Fig. 4a are all considerably high and may have adverse effect to the public health [295-303]. Because of no existing regulation to limit the particle concentration [294], the high emission rates have attracted investigators' attentions to build the emission database and establish a standard for future control measures.

The GMDs of metal additive filaments were less than those in the cases with nonmetallic additive ones. For copper additive PLA filaments [224], the GMD was 9.8 nm compared to 13.4 nm to the nonmetallic additive one. Alberts et al. [225] found that the GMD for PLA Cu additive and ABS tungsten additive was 22.7 and 26.7 nm, respectively, while the original one was 57.2 and 29.7 nm, respectively. It has been shown that particles in the size range from 10 to 30 nm where the mean sizes of particles emitted from a 3D printing were, are most likely depositing in deep lung area and causing inflammation and possible cancer [286].

A1.5. Reduction of particle emissions

Because a 3D printing typically emits small particles in high concentration during the change of operational conditions, especially when printing with metal-additive filaments, it is necessary to reduce the particle emission for a healthy indoor quality. Blocking the formation of emitted particles (i.e., at the source) is a radical approach for the particle emission control but it may not be always applicable in practice. Engineering control to reduce the emission (i.e., post-process) is the alternatives to the source control. In the following sections, we discuss the emission control strategies from these two aspects.

A1.5.1 Controlling particle emission from the source

It has been shown that 3D printing emits significant VOCs and particles. It is because the heating of filaments was above 200 °C, resulting in the decomposition of some ingredients, typically volatile and semi-volatile organic compounds. According to literatures, the primary SVOCs emitted from commonly used filaments, such as PLA, ABS, Nylon, etc., include lactide, styrene, acetaldehyde, caprolactam, benzaldehyde, ethyl benzene and formaldehyde [221, 222, 240, 268, 287, 304]. The emission concentration for individual SVOCs varies from less than one to hundreds of micrograms per cubic meter depending on printing conditions and the TVOC (including VOCs and SVOCs) is usually in the range of several to ten thousand of micrograms per cubic meter, e.g., 3-11000 mg/m^3 for PLA and ~13.2-9000 mg/m^3 for ABS [300, 301]. Based on the ANSI/CAN/UL 2904 [239] and the Leadership in Energy and Environmental Design [305], the upper limit for indoor TVOC is 500 mg/m^3. For the primary SVOCs, Occupational Safety and Health Administration (OSHA) {OSHA, June 1st 2021 #238} has the 8-hour time-weighted average (TWA) exposure limit and short-term exposure limits (STEL) for different VOCs based on the hazardous level. For example, they are 50 ppm TWA and 100 ppm STEL for styrene, 25 ppm TWA for acetaldehyde, 5 ppm TWA and 10 ppm STEL for caprolactam, 5 ppm TWA and 30 ppm STEL for ethyl benzene, and 0.75 ppm TWA and 2

ppm STEL formaldehyde. For the benzaldehyde, it is not listed in OSHA exposure table, but Australian Inventory of Chemical Substances (IMAP) [306] suggests 2 ppm TWA and 4 ppm STEL respectively. For the lactide, as there is still a lack of sufficient evidence for health effects, the exposure limits are not determined yet. However, considering most of the VOCs or SVOCs have adverse health effects [221, 273, 296], mitigation methods should be applied to control the emissions below the limits.

As explained in Section A1.2, the particle formation is closely related to the amount and type of condensable SVOCs released from heated filaments. If the chemical compositions of SVOCs are known, the ingredients of filaments can always be redesigned (either by altering the percentages of ingredients or replacing some ingredients) to minimize the SVOC emission. Researchers analyzed the compositions in filaments, which contribute to the SVOC emission. Vance et al. [243] studied the Raman spectra of the compositions of SVOCs released from raw ABS and PLA filaments, printed objects and emitted particles. In the case of raw ABS filaments, they found that the spectra agreed well for raw ABS filaments and printed object, but the spectra of emitted particles did not show main peaks indicating the existence of styrene and acrylonitrile, which are two major components in ABS filaments. In the case of PLA filaments, their results showed that the spectra of printed object differed from that of raw filaments, and the spectra of emitted particles presented broad Raman peaks at ~1300 and ~1600 cm^{-1}. The above observations indicated that condensed particles were not from the ABS or PLA polymer itself and they hypothesized that the condensed components were from the chemical additives in the filaments. Research by Bai et al. [285] proved the above hypothesis by finding that the commonly used antioxidants and lubricants oxidize and volatilize at the printing temperature ranges of 230−270 °C. Gu et al. [244] also evidenced that the compositions of the condensed particles were from additives such as retardants. They also studied the particle volatility by heating emitted particles at different temperatures and found that emitted particles started to

evaporate at 150 °C and a certain percentage of particles remained even at 300 °C, which provided additional evidence regarding the particle formation of SVOC-involved nucleation and condensation. In addition, Ding et al. [227] revealed that the main VOCs released were light components of low molecular weight and the depolymerization products of macromolecules, and the percentage of condensable SVOC mass in total VOC (TVOC) were less than 5% for all filaments studied in their investigation.

Metal additive filaments usually emit particles in the concentration 1-2 orders of magnitude higher than those emitted by raw or other additive filaments. Researchers revealed the role of metal additives played in the particle emission. One of the hypotheses was that, after they were released, metal particles, which are blended in filaments, served as nuclei for the heterogeneous nucleation [225, 243, 245]. However, Vance et al. [243] and Alberts et al. [225] did not identify any metals from the filter sampling using the SEM/EDS (energy dispersive X-ray spectrometry) characterization. They thus assumed the presence of metal particles in filaments were not released and unbounded during the heating although it affects the particle emission. Potter et al. [245] hypothesized the effect of metal additives on particle emission from the chemical reaction perspective. They indicated that the catalytic activity of iron and its ability to bind the organic oxygen contributes to low temperature degradation and the formation of lactide, thus this kind of filaments could emit more SVOCs. No experimental evidence was provided to evidence the above hypothesis.

Although the progress has been making on the characterization of chemical compositions of particles emitted from the heating of filaments, the role of additives on the formation of emitted particles remains at large. For example, pigments and dyes are commonly used additives in ABS filaments, but the thermal degradation of pigments and dyes present in ABS plastics has not been carefully studied. In addition, due to the limitation of measurement methods, the reported data on the chemical composition and amount of released SVOCs are in

138

question. The SVOC concentrations were usually several hundreds of ppb [222, 244, 265], thus an accurately sampling SVOC particles is very challenging. First, the sampling time needs to be long enough to reach the minimal detectable quantity of emitted particles. However, the SVOC particles collected on filter media could evaporate during the long sampling period. An annual denuder to collect gas and particle phases of SVOC separately should be applied [286, 307]. Secondly, different sampling locations in a test chamber can significantly vary the data because of the spatial distribution of SVOC in the chamber. Lastly, the analytical procedures such as SEM analysis cannot detect SVOC particles which may evaporate under the vacuum and bombardment of a high-energy electron beam. A sophisticated thermal carbon analysis is required for the above characterization [307].

A1.5.2. Controlling emitted particles by engineering solutions

The engineering control methods were primarily based on the factors influencing the emission, including the nozzle temperature, fan speed, infill setup, ventilation and enclosure, filtration, and humidity. The detailed discussions on these factors are given in the following.

A1.5.2.1 Functional and operational conditions of printing

It has been reported that the nozzle malfunction, e.g., nozzle clogging and print aborted, could increase the particle emission in an FDM printing. As shown by Yi et al. [263], the particle emission by the nozzle malfunction when printing with a PLA filament could increase the concentration of emitted particles by a factor of 3.3 compared to that under a normal operation condition. Mendes et al. [246] also found that because of the nozzle malfunction, the particle concentration increased by 16.76 times when printing with an ABS filament. For the reference, the data reported by the above two studies are reproduced and shown in Fig. A1.5. From the data presented by Poikkimaki et al. [224], it is found that the increase of particle emission was associated with the printing temperature. Although it is difficult to directly

compare the results among different studies owing to different experimental setups, conditions, and filaments used, it is generally believed that operators should avoid the nozzle malfunctions, especially printing with ABS filaments at high temperatures.

The nozzle temperature is a very important parameter that could significantly influence the particle emission in a FDM printing. Researchers have found that the particle emission would be elevated by increasing the nozzle temperature [224, 225, 238, 241, 246, 267, 272]. Fig. A1.6 summarizes the increase ratio of the particle emission from the low to elevated printing temperatures.
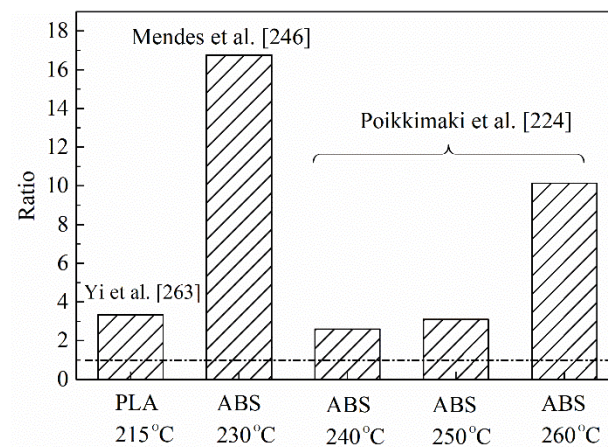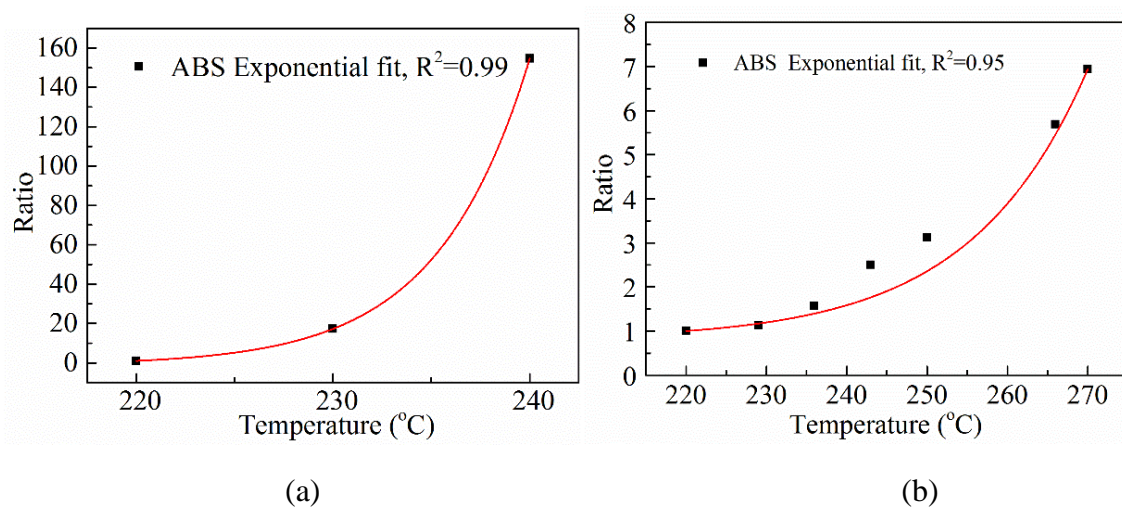

Figure A1.5. Increase ratio of particle emission due to malfunction. Data for Yi et al. [263] are peak values and others are average. PLA-W is PLA filaments with wood additives.

(a)   (b)
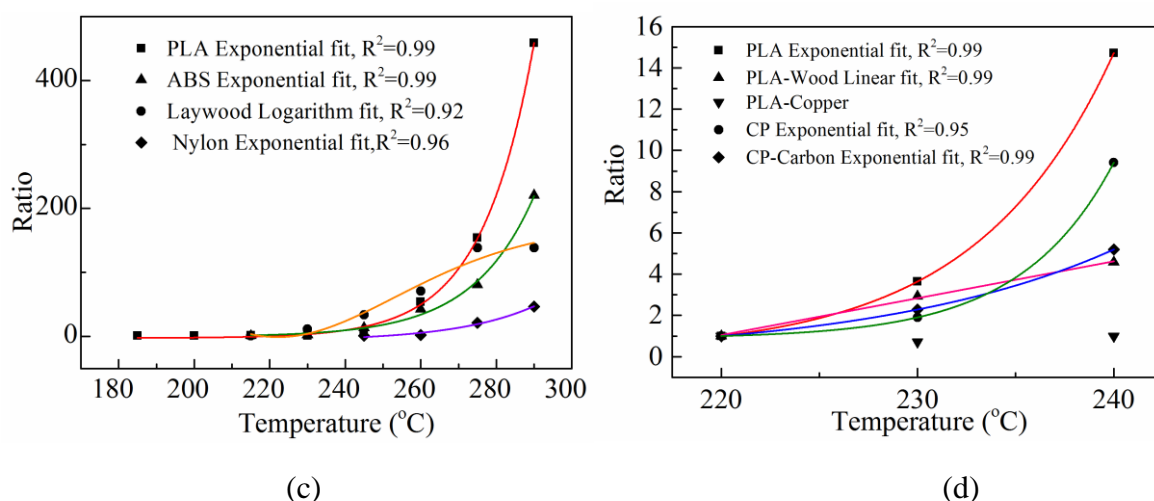
Figure A1.6. Relationship of increase ratio of particle emission with nozzle temperature: (a) from Sittichompoo et al. [241], (b) from Zhang et al. [238], (c) from Stabile et al. [272] and (d) from Jeon et al. [267]. CP stands for copolyster.

Although the data were from four different studies, an exponential growth of the emission ratio with the printing temperature was evident for both PLA (except the wood additive one) and ABS filaments. The above indicated that the particle emission from an FDM printing increases considerably when printing at the temperature higher than the recommended one for these two filaments. In comparison, the wood additive PLA filament (Fig. A1.6c) showed a correlation of linear regression, and the copper additive PLA filament had no clear correlation. Researchers also investigated several other kinds of filaments, for examples, CP, CP-carbon, laywood and nylon [267, 272]. The increase ratios of particles emission for all these filaments were relatively low compared to ABS and PLA under the same measuring condition. A possible reason was that the amount of condensable SVOCs contained in these filaments were low.

Another significant setting that could affect the particle emission was the filament infill parameters, e.g., infill density and height which are the density and height of the non-solid portion inside the outer shell of an object. Cheng et al. [247], Sittichompoo et al. [241] and Khaki et al. [283] found that they had significant influence on the particle emission although

there was inconsistency on the findings of their influence to the particle emission. Fig. A1.7 reproduces the data reported by Chen et al. [247] and Sittichompoo et al. [241]. Based on the data shown in Fig. A1.7, the increase of infill density could exponentially increase the particle emission while the increase of infill height would linearly increase the particle emission. The maximum ratio increase due to the infill density could be as high as 41 times [247], but also could be as low as 1.05 [283]. In comparison, it could reach 16 times [241] and 9 times [247] when increasing the infill height of filaments. The above difference might be caused by different operational settings such as the feeding speed, different printing temperatures, printing objects and cooling fan speeds. The effects of infill parameters on the particle emission from a FDM printing could only be better understood through parametric studies.
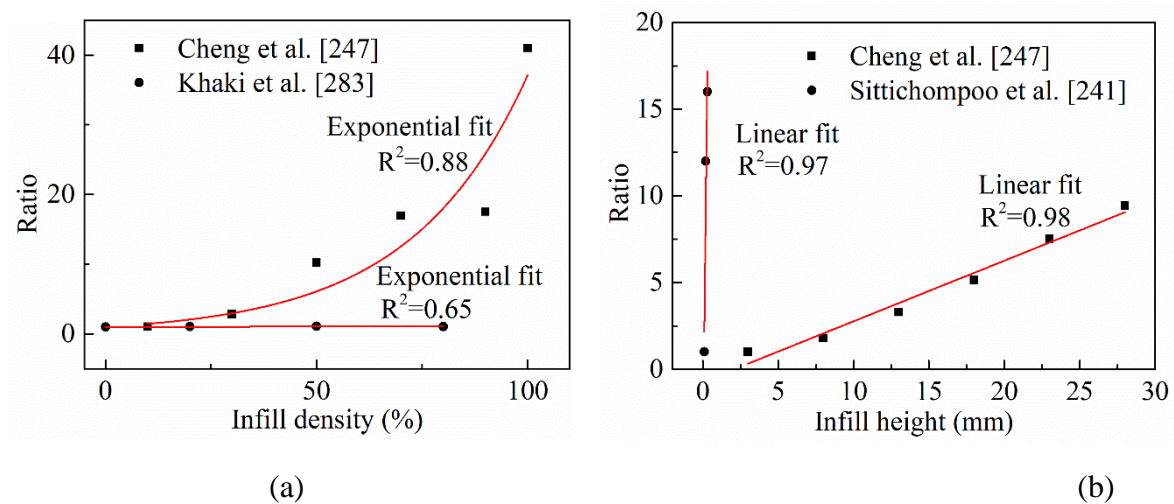
Figure A1.7. Relationship of the increase of particle emission ratio to (a) infill density and (b) infill height.

A1.5.2.2. Effective ventilation and filtration

Local exhaust ventilation (LEV) is considered as a very effective ventilation method [308, 309] because it can directly remove the pollutants from the emitting source. However, its efficiency highly depends on if the printer is enclosed by the LEV. In 3D FDM printing, high particle removal efficiency by using a LEV (highest as 98.3%) is usually achieved by enclosing

the LEV system around the printer, either by adding an enclosure to cover the whole printer [248, 249] or attaching an effective LEV system very close to the nozzle [269], shown as the Enclosure+LEV in Fig. A1.8. In comparison, using the enclosure or LEV alone usually had very low particle removal efficiency unless the enclosure was sealed tightly [249]. Therefore, it is encouraged to combine the LEV with the enclosure. The low efficiency for the LEV case was because the hood of the LEV was too far from the nozzle, which weakened the effectiveness of the LEV [249]. Azimi et al., [310] showed that increasing air change rate was an option to increase removal efficiency for this scenario. Their results illustrated that increasing the air change rate from 25 L/s to 100 L/s could increase the ventilation efficiency from 2% to 80%. Therefore, appropriately increasing air change rate of the ventilation system can also be an effective method.
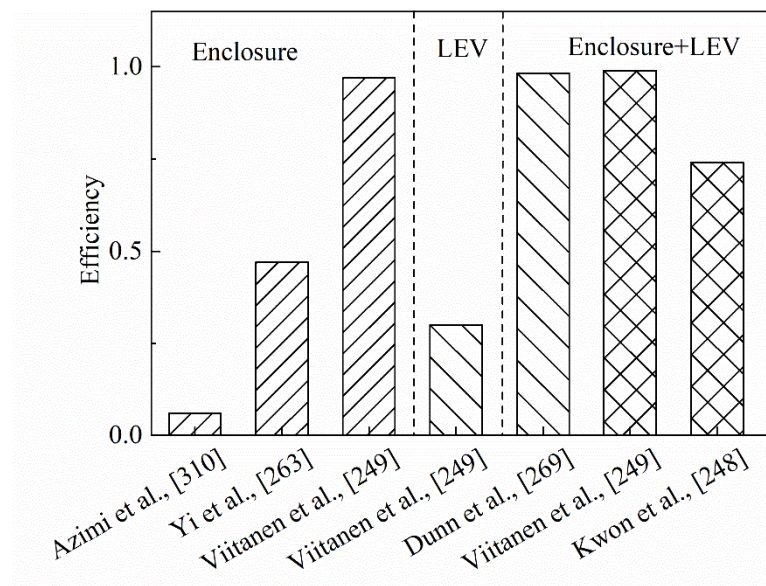
Figure A1.8. Reported particle removal efficiency using the ventilation with or without the enclosure for different studies. *LEV stands for local exhaust ventilation.

The enhancement of particle removal efficiency could be achieved by installing a high efficiency filter at the outlet of the enclosure chamber. As shown in Fig. A1.9, most of the removal efficiencies were higher than 90% [248, 266, 273]. The lowest efficiency was found

when using an electret filter if its minimum efficiency reporting value (MERV) value is lower than 11, which was designed to remove particles in the sizes from 1 to 10 μm with the particle collection efficiency of 60% - 80% for 1 μm particles [248]. Particles emitted from the 3D FDM printing were mainly less than 1 μm in size. Nonetheless, the particle exposure outside the enclosure chamber can be significantly reduced by using HEPA (High Efficiency Particulate Air) filters.
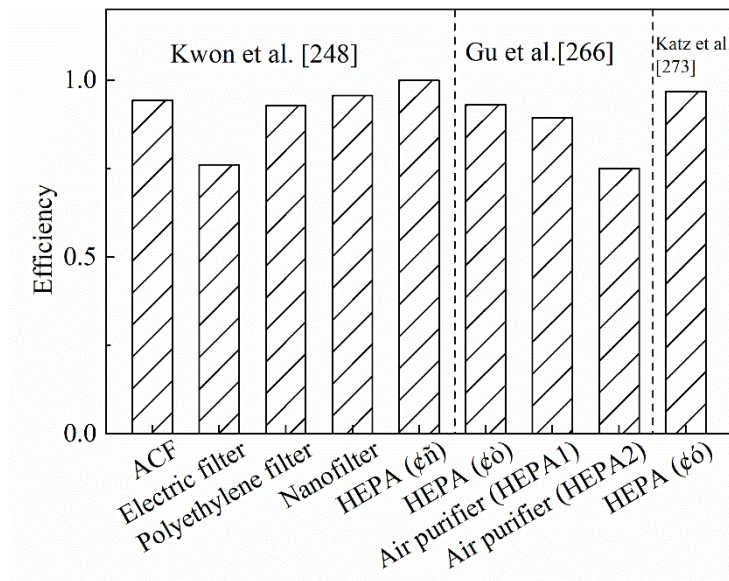
Figure A1.9. Particle removal efficiency using different filters for different studies. ACF stands for active carbon filter.[248, 266, 273]

A1.5.2.3 Environmental factors: chamber humidity and temperature

The increase of the chamber relative humidity (RH) by releasing mists from a humidifier could be a promising method to reduce the concentration of nanoparticles. It is because under a high RH, nanoparticles could grow to larger sizes to be less harmful or being easily removed. The potential particle growth dynamics is that the primary particles collide with the fine droplets or absorb water molecules, even the occurrence of deliquesces, at a high RH [311, 312]. This phenomenon is referred to as the nucleation scavenging, i.e., an aerosol (cloud condensation nuclei) inducing formation of a cloud droplet in supersaturated water vapor. As

mentioned in Section A1.2, the 3D printing emits variety of VOCs and SVOCs, in which the SVOCs condense to from primary particles and serve as the nuclei for more SVOCs to condense on. Many 3D printing SVOCs, such as lactide, acetone and ethanol etc., are water soluble enhancing their growth at high RHs. Rao et al. [250] and Zhu et al. [251] used cool mist humidifiers to increase the RH in the enclosure chamber and found that $PM_{2.5}$ mass concentration increased due to the particle growth when the chamber humidity was higher than 70%. Although the authors explained their observations with the effects of coalescence under the abundant of water molecules, no further data was shown to prove the decrease of nanoparticle concentration. Therefore, more research is needed to confirm the hypothesis. To be noted, the method of increasing humidity should not be applied to some types of filaments, i.e., wood powder added filament, which can lower the elasticity and cause swelling of the modulus at high RH [313].

The chamber temperature should also be important on the control of particle formation and growth because it affects the super-saturation ratio of SVOC vapors. Unfortunately, most of the reported research only focused on the change of the printing nozzle temperature. It is simply because the heating feature was not built in the enclosed chambers in previous studies.

A1.6 Optimization of printing parameters to reduce particle emission

Various factors have been found to have their own effects on the formulation and growth of particles from a 3D FDM printing. The collective effect by all the influencing factors on the particle emission has not been accomplished. It is because that the data reported by different research groups were done by different methods and setups. It is not realistic to perform all the experiments considering all the influencing factors by one single research group. To identify all influencing factors on the emission of particles from a FDM printing, an advanced modelling method for the evaluation is necessary.

Regarding to applying modeling method to estimate 3D printing emissions, we found only a few literatures. Zontek [252] first applied the eddy diffusion model to calculate the spatial and temporal concentration of emitted particles in a test chamber, and then based on the calculated data to evaluate the distribution variation of emitted particles due to the variation of the filament extrusion rate and temperature, printing time, the distance of observers from the source, and diffusivity variables via a Monte Carlo simulation. Zhang et al. [226] developed a lognormal moment model to predict the formation and subsequent evolution of emitted particles. They compared the calculation result with the experimental result to validate their modeling. However, these models were used to predict the emission only and not able to optimize the printing parameters to minimize the emission.

Different from the above numerical modeling, machine learning is also a very effective tool for building a model to deal with multi-dimensional influencing factors without the need to scientifically understand the mechanisms involved in the formation and growth of emitted particles [253, 284, 314-316]. Researchers have been applying the machine learning to the 3D printing, including the printing design [254, 256], process optimization [257, 258], *in-site* monitor for the product quality control [259, 260] and the security of attack detection [261]. However, very few studies were found to improve the particle emission control. Only one study intended to build a complex model to include the exposure variable, yet no practical strategies were actually reported [255]. However, the experience of applying the machine learning models on different aspects about 3D printing can be referred. It was found that artificial neural network (ANN) model had good performance in multi-objective optimization. It is found that 31 papers have used machine learning to optimize operation parameters for 3D printing and 25 of these 31 [43] successfully used single ANN or combined ANN model to conduct the optimization [67]. Results showed that ANN can predict complex relationships between inputs and outputs which cannot be easily recognized by numerical methods and a basic 3-layer ANN

146

is sufficient to achieve an accuracy of prediction as high as 98% [317, 318]. Our research team also successfully applied ANN model to predict nanoparticle retention efficiency in membranes under different conditions which is a multifactorial nonlinear case and has demonstrated the good performance of the ANN modeling [111].

A1.7 Conclusion and future research

This review summarized the published studies related to the emission of particles from the 3D FDM printing, including the mechanisms for the formation and growth of emitted particles, particle characterization methods, influencing factors for the particle emission, control strategy and modeling. The research gaps in each above-listed area were also discussed. The information given in this review could serve as the foundation for the future research on the topic of the particle emission from a 3D FDM printing.

The main issues for the characterization of emitted particles are on the setting of air change rate, the selection of measurement instrument, and the sampling method and location. A unit-specific air exchange rate should consider both the air mixing condition and the temperature distribution in a test chamber. For the fast and accurate capture of the characteristics of particle formulation and evolution, multiple instruments covering a wide size range and having fine sizing resolutions should be utilized at the same time. The sampling points should be evenly distributed around the printing nozzle to avoid the interference from the spatial variation of particle size and concentration, as well as the temperature in a test chamber.

Due to the lack of a standardized measurement method, noticeable inconsistency on the data of particle concentration and size distribution was found. In the cases of the most used PLA and ABS filaments, the particle emission rate at the 25% and 75% percentiles ranged from 1.0×10^8 #/min to 1.1×10^{10} #/min and 3.3×10^8 #/min to 4.0×10^{10} #/min, respectively; ranged from 23.8 nm to 46.6 nm and 28 nm to 53.6 nm, respectively, for the particle size. Compared

to the cases of non-metal filaments, the emission rate could be at least one order of magnitude higher and the emitted particle sizes were smaller in the cases of metal additive filaments. Future research on the filament material under the consideration of minimizing the particle emission during the 3D FDM printing is required. The observation of high emission rate and small sizes of emitted particles during the 3D FDM printing raises the health concerns, requiring effective control strategies to reduce their exposure.

The radical emission control is based on the blocking of emission source. Its success depends on the understanding of influencing factors on the particle emission and mechanisms of emitted particle formation and growth. Although the scientific knowledge of aerosol dynamics has been applied to explain some experimental observations, uncertainties due to the complex environmental and printing conditions, as well as the filament composition, such as blended pigments and metal additives, remains existed.

For the engineering solution to the emission control, we found that the printing nozzle temperature exponentially influenced the particle emission in the cases of printing PLA and ABS filaments, which can emit more condensable SVOCs. For the filaments that emit lower amount of SVOCs, such as CP, CP-carbon, laywood and nylon, the increase ratios of particles emission were relatively low. For additive filaments, it is only found that particle emission increased linearly with elevated temperature for wood-additive PLA. More research is needed for metal-additive filaments in the near future. We further found that the infill parameters, e.g., infill density and height, significantly affect the particle emission rate, which were ignored in the previous studies. In addition, the local ventilation and application of HEPA filters at the enclosure chamber outlet would offer good efficiencies for the particle removal. The change of chamber environment parameters such as humidity and temperature were potential methods to reduce the emission of particles from a 3D FDM printing. Although these findings were useful

in guiding the design of emission control, a comprehensive strategy requires to be developed by linking all existing control knowledge.

The modeling of the formulation and growth of emitted particles is an area which has been the least focused by researchers. The numerical modeling of the particle formulation and dynamics using the general particle dynamic equations has been applied with some success. Alternatively, the machine learning has been very successful in the prediction of the manufacturing outcomes which are affected by multiple factors (without the scientific understanding of the process mechanisms involved) when numerous data sets taken under a standard method are available. It could be applied herein to resolve the difficulty encountered in the phenomenological modeling. Unfortunately, very limited studies have been reported to apply the machine learning for modeling the particle emission from a 3D FDM printing.

Chapter A2 Sampling and Characterization of Particle Emission from the

3D FDM printing

A2.1 Introduction

The fused deposition modeling (FDM) 3D printing technology has been increasingly utilized in various places to fulfill different job tasks, for example, for the model printing in offices and schools, cloth printing in fashion companies, surgical product printing in hospitals and prototype printing in car manufactories [213-215]. Its increasing popularity is due to the time- and cost-efficiency and convenience of prototyping a model. For the FDM printing, a filament is heated to ~200 ∘C and then extruded out of a nozzle. A model prototype is printed layer-by- layer based on a programming code. When the heating temperature is higher than a certain value, the chemical components in the filaments can decompose and vaporize, resulting in the emission of volatile organic compounds (VOCs) and semi-volatile organic compounds (SVOCs) [222]. The emitted SVOCs could form particles via nucleation and condensation as the ambient temperature is reduced [237, 303]. The produced nanoparticles could potentially cause the increase of adiposity and insulin resistance [319], lower the level of sex hormones [320], and many respiratory diseases [228, 229, 321]. It is thus very important to characterize the particle formation and emission, and to propose an effective engineering solution to reduce the human exposure within the building environments.

To investigate the particle emission from 3D FDM printers, researchers have been measuring the total concentration and size distribution of particles, and VOC concentration and composition in test chambers [225, 238, 244, 262], in office spaces or at industrial sites [281, 284]. Some researchers followed the protocol for laser printers [238] and others conducted the measurement using the approaches based on other similar protocols [225, 244, 262]. As a result, significant inconsistency among the reported data sets is observed. It is very challenging to

compare those results to derive the major finding. For example, the particle concentration emitted from printing the same type of filament was found to vary from 10^5 to 10^8 #/m^3 for poly-lactic acid (PLA) filaments, and 10^6 to 10^8 p/m^3 for acrylonitrile butadiene styrene (ABS) filaments [322]. The concentration and major species of VOCs were also greatly varied [222, 244, 245, 296, 304]. To provide better characterization of the emission from 3D printing, the UL published ANSI/CAN/UL 2904 Standard in 2019 [239]. The guideline however allows users to determine experimental variables, e.g., sampling at different locations, printing different objects, different printing parameters and air change rates, etc. It is known that all the above factors can affect the measurement results [267, 272, 276]. Therefore, it remains challenging to compare the data reported by researchers [242, 322]. To exclude the interferences from experimental variables, typically on the temperature distribution, Chýlek et al. [240] and Sittichompoo et al. [241] proposed to use the thermogravimetric analysis (TGA) method. It is only required to put a piece of testing filament, e.g., 2.85 mm in diameter and 10 mm long, in a ceramic tube in a high-temperature furnace and heat the filament to the same temperature as that used in a 3D FDM printer. However, the particle generation rates between the TGA and conventional chamber method may have quantitative differences. For example, the TGA heated the entire 10 mm long filament in the furnace at ~200 °C, and evaporation mass transfer occurred at the whole filament surface area which was about 0.9 cm^2 (=3.14 × 0.285 cm × 1 cm). In comparison, the area taking place evaporation in a real 3D printing was only ~0.06 cm^2 (=3.14/4 × 0.285 cm × 0.285 cm). There is about a 15 times of difference. Besides, the SVOCs of TGA remained in tube at much higher temperature (~200 °C inside the furnace tube) and longer time than the real printing where the temperature of SVOCs reduced

to air temperature of chamber instantly. Therefore, although the TGA method simplifies the sample preparation and measurement, the obtained particle emissions may not be representative for a real FDM printing. It is thus crucial to develop a simple and effective method that can capture the representative particle emission from a FDM printing.

The nanoparticle formation and growth during the 3D FDM printing include homogeneous and heterogeneous nucleation, condensation, and coagulation. The particle formulation and dynamics are very complicated, which depend on the source and yield of SVOC, e.g., filament material, printing temperature, feeding speed, etc., and environmental conditions, e.g., chamber size, air change rate, temperature and flow distribution, etc. Therefore, printing with different conditions and sampling at different locations would lead to different results. The existing metrics, e.g., the emission rate [227, 238, 244, 248, 275], total particle concentration and particle yield [238], only describe the stationary status of the particle emission which cannot reflect a moment of dynamic change of the emission during the printing. When evaluating emissions with fast size change and high emission concentration, such as printing additive filaments [224, 225, 245, 264], the existing metrics may be insufficient to explain the emission characteristics, especially when the sampling is conducted a distance away from the source.

To address the aforementioned issues, a new sampling method to instantly measure the size distribution of emitted particles from the 3D FDM printing was proposed. A new metric, dynamic emission index (DEI), was proposed to better characterize the dynamics of particle formation and growth in 3D printing. The ultimate goals of this study are to prove the feasibility

153

and advantage of the new sampling method, and to validate the new metric for better characterizing the particle emission.

A2.2. Materials and Methods

A2.2.1 3D printer and filaments

A widely used mini Lulzbot 3D printer (Fargo Additive Manufacturing Equipment 3D, LLC, Fargo, SD) was selected for this study [221, 321]. The printing head is made of a hardened steel with a convergent nozzle having a 1.2 mm exit diameter. The recommended filament diameter is 2.85 mm. During printing, a cooling fan was running at 50% speed to protect the nozzle from overheating. The operational parameters, including the printing time, printing speed (60 mm/s), printing temperature (210 ◦C) and bed/substrate temperature (70 ◦C), were kept constant in the printing with different filaments. The investigated filaments include two basic filaments, i.e., original PLA (PLA-O) and ABS in white color (ABS-W), and four filaments with functional additives, i.e., carbon-fiber PLA (PLA-C), iron PLA (PLA-Fe), fluorescent ABS (ABS-F) and glow-in-dark ABS (ABS-G). Note that the particle emission from the printing of ABS-F and ABS-G have not been reported. The PLAs were from Polymaker (Polymaker LLC., Shanghai, CN) and the ABSs were from Gizmo Dorks (Gizmo Dorks LLC., Temple City, CA). The color and composition of tested filaments are given in Table A2.1. For additive ABS filaments, detailed chemical compositions are not available from the vendor. Based on their features, it is assumed the fluorescent filament contains fluorescent pigments and the glow-in-dark filament contains strontium aluminate (or zinc sulfide and calcium sulfide). The suggested printing temperatures for PLAs and ABSs are 205 ◦C and 220–

154

225 °C, respectively. Then 210 °C was selected in all the printings to keep the operating

parameters constant in this study.

Table A2.1. Description for different filaments

Material	Description
PLA-Original (PLA-O)	Polyactide resin (weight > 92%), polymer (weight <7%), transparent, melting point 195 -225 °C, decomposition point 250 °C
PLA-Carbon fiber (PLA-C),	Polyactide resin (weight > 85%), carbon fiber, (weight <14.25%), dark grey, melting point 195 -225 °C, decomposition point 250 °C
PLA-iron additive (PLA-Fe)	Polyactide resin (weight > 55%), iron (weight < 45%), black, melting point 185 -215 °C, decomposition point 250 °C
ABS-White (ABS-W)	Polymer, white
ABS-Fluorescent (ABS-F)	Polymer (UV activated), blue
ABS-Glow (ABS-G)	Polymer, white

A2.2.2 Experimental chamber and instruments

Fig. A2.1 shows the schematic diagram of the experimental system for characterizing the

particle emission from the 3D printing. A testing chamber with a dimension of 1 m × 0.6 m x

0.5 m was used to house the printer sitting at the center of the chamber. Filtered air was

introduced into the chamber from its front side through an air manifold. The outlet located on

the top of the chamber equipped with an activated carbon (AC) filter and a HEPA filter in series.

To instantly characterize emitted particles from the printing nozzle, a rectangular aluminum

cup sampler was designed and fabricated (as shown on the left side of Fig. A2.1). The cup

sampler enclosing both nozzle and cooling fan was attached to the printing head assembly.

After attached, the upper surfaces of the sampler walls were sealed by the extending surface of

the printing head. The bottom surface remained open. The sampling was through four circular ports (one on each side of the sampler) which are aligned with the height of the printing nozzle. Thus, the instantaneous emission from the printing nozzle was quickly sampled from all directions of the sampler and combined into one stream to achieve a uniform sampling. Notice that the inlet of the cooling fan was not enclosed in the sampler, but its four outlets located on the corners of the printing head assembly were enclosed in the sampler (bottom view of Fig. A2.1). Thus, the cooling air was directly shooting at the nozzle to promote the gas to particle nucleation and condensation of SVOCs. From above, it is concluded that the use of the new sampler allows fast capturing realistic characteristics of emitted particles from the 3D printing.

A Scanning Mobility Particle Sizer (SMPS, equipped with the Differential Mobility Analyzer, DMA, Model 3081 or Nano-DMA Model 3085, and the Ultrafine Condensation Particle Counter, UCPC, Model 3776, TSI Inc., Shoreview, MN) was used to measure the size distribution of particles from 10 nm to 500 nm or 5 nm–170 nm. The length of the sampling tubing was kept as short as possible to minimize the diffusion loss of sampled particles. According to the work of Gormley and Kennedy [323], the diffusion loss for particles in the sizes larger than 5 nm in the sampling tube is negligible. A thermometer was placed in the chamber to monitor both temperature and RH, which were kept within 22–24 ∘C and 15–20%, respectively.
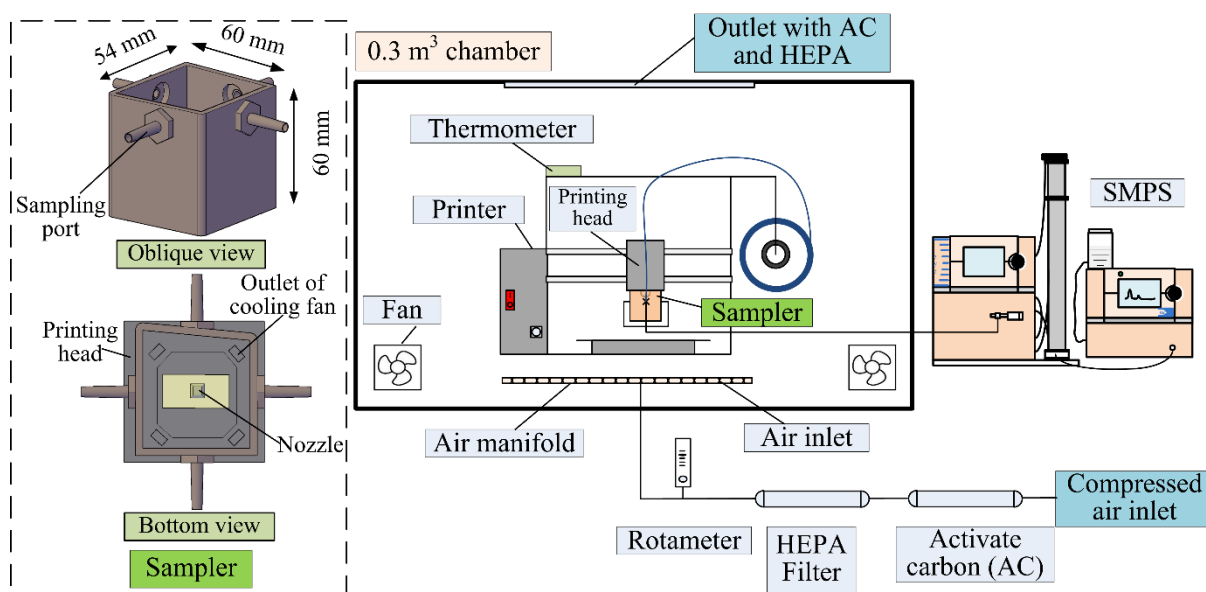
Figure A2.1. The schematic diagram of the experimental system, including the 3D printer, ventilation, flow control and particle measurement instrumentations

A2.2.3 Experimental procedures and conditions

To better understand the particle emission characteristics, three experimental procedures were designed and compared. As shown in Table A2.2, the procedures include the implement of newly designed sampler (Case 1), direct sampling in the chamber at 10 cm away from the nozzle (Case 2) [221, 238, 244], and direct sampling in the chamber with forced convective flow (Case 3). The air change rate was 0.3 h^{-1} 1 for Cases 1 and 2, and 1 h^{-1} 1 for Case 3. Note that, for the sampling through the sampler (Case 1), the effect of air change rate on measurement results should be minimized. In the printing of each filament (no actual object was printed, just extruding), all three procedures were conducted and repeated for at least 4 times to obtain a representative result. The printing time was 155 mins (including 5 mins of preheating) in order to have sufficient time for the emission to reach equilibrium if applies. The

157

post printing period was also set at 150 mins so the particle concentration could return to near-background level.

Prior to each experiment run, all surfaces in the chamber were cleaned by alcohol wipes for minimizing the influence of outgassing from previously deposited particles or VOCs and the chamber was ventilated with filtered air for at least 20 mins. After the cleaning and ventilation, the chamber was sealed and purged with filtered air again for another 20 mins until the background particle concentration was less than 50 p/cm^3 [242]. The measurement was conducted continuously along the air purging, preheating, printing and post-printing (i.e., stop printing). Thus, the particle size distribution was available during the entire printing process.

Table A2.2. Case conditions and descriptions.

Case number and short name	Case description	Auxiliary devices	Sampling points	Air change rate (h^{-1})	Preheating/printing/ printing off (min)
1. New sampler	Sampled using the cup sampler	The sampler	4 sides of the sampler	0.3	5/150/150
2. Chamber	Sampled in the chamber without the sampler	None	10 cm away from the nozzle	0.3	5/150/150
3. Forced convection	Sampled in the chamber and mixed the air with the fans	Axial fans	10 cm away from the nozzle	1	5/150/150

A2.2.4 Data Analysis

A2.2.4.1 Emission rate

To evaluate the particle emission level, we calculated the emission rate based on the mass balance as [244]:

$$\frac{dc(t)}{dt} = \frac{1}{V}R - kc(t) \tag{A2.1}$$

where $c(t)$ is particle concentration, p/cm^3, R is particle emission rate, p/s, V is the volume, m^3, and k is total loss coefficient which can be calculated as:

$$k = \frac{\ln c_1 - \ln c_2}{t_2 - t_1} \tag{A2.2}$$

where c_1 is the particle concentration at least 5 minutes after printing to exclude the unstable period, p/cm^3, c_2 is the particle concentration after the selected time for c_1, p/cm^3, t_1 and t_2 is the time for c_1 and c_2, s, respectively.

Particle emission rate as a function of time can be obtained by solving Eq. (A2.1) as [324]:

$$R = V\left(\frac{c(t) - c(t - \Delta t)\exp(-k\Delta t)}{\Delta t \exp(-k\Delta t)}\right) \tag{A2.3}$$

where Δt is time between two data points, s.

Total particle emission, TP, can be obtained by integrating Eq. (3) over time as:

$$TP = V\left(\frac{\Delta c_p}{t_s - t_b} + kc_{av}\right)(t_s - t_b) \tag{A2.4}$$

where t_b is the time when printing started, s, t_s is the time when particle concentration becomes steady, s, Δc_p is the difference of the particle concentrations between t_b and t_s, p/cm^3; c_{av} is the arithmetic mean of particle concentrations between t_b and t_s, p/cm^3.

A2.2.4.2 Dynamic emission index

In addition to the total particle emission, it is desired to have a metric to illustrate the emission at different time moment during the printing in consideration of dynamic size changes of the emitted particles. Therefore, we propose a new metric, i.e., the dynamic emission index (*DEI*), as:

$$DEI = \frac{C_p(t)}{\sum_{1}^{n} C_t(t)} \times \frac{C_p(t)}{\sum_{0}^{t_z} C_p(t)} \tag{A2.5}$$

where $C_p(t)$ is the particle concentration in a size range (interval) during the printing, $\#/cm^3$, $C_t(t)$ is the total particle concentration at time t, $\#/cm^3$, n is the number of size bins, t_z is the total printing time, minute. This metric shows the time dependent most dominant particle sizes during the entire printing process. The metric refers not only size interval with high concentrations but also provides the variation of emission intensity for each size interval. The value is always less than 1 and the greater the number is, the emission intensity from that particle size range is stronger.

A2.3. Result and Discussion

A2.3.1 Comparison of the particle emission measured by different methods

To investigate the variation among different emission data reported by researchers using different setups and experimental conditions, the maximum number concentration of emitted particles reported in eight literatures and by this study are compared in Table A2.3. The information of the experimental setups and conditions of the eight studies could be found in

Table A2.S1 of Support Information (SI). Among them, Byrley et al. [304] and Ding et al. [242] followed the ANSI/CAN/UL 2904 method and studies from Chylek et al. [240] and Sittichompoo et al. [241] were the only two works using the TGA method. The others used the conventional method (similar to that used in Case 2).

Table A2.3 Comparison of maximum concentration of emitted particles measured in the current and previous studies in the 3D printing of original PLA and ABS filaments.

	Particle concentration (#/cm^3)			
	PLA-Chamber	ABS-Chamber	PLA-Sampler/TGA	ABS-Sampler/TGA
Kim et al. [262]	5.20 x 10^4	1.74 x 10^6	-	-
Stabile et al. [272]	5.15 x 10^3	-	-	-
Zhang et al. [238]	4.20 x 10^2	1.10 x 10^6	-	-
Ding et al. [242]	-	3.52 x 10^5	-	-
Alberts et al. [225]	4.00 x 10^5	8.50 x 10^5	-	-
Byrley et al. [304]	7.73 x 10^5	3.32 x 10^6	-	-
Chylek et al. [240]	1.28 x 10^3	6.80 x 10^5	1.69 x 10^7	1.66 x 10^7
Sittichompoo et al. [241]	-	1.30 x 10^5	-	3.07 x 10^5
This study	8.99 x 10^4	1.02 x 10^6	5.22 x 10^4	8.97 x 10^5

As shown in Table A2.3, the differences of the maximum particle concentrations measured in the chamber are with 3 (7.73×10^5 vs. 4.2×10^2) and 1 (3.32×10^6 vs. 1.30×10^5) orders of magnitude for PLA and ABS, respectively. Note that both Byrley et al. [304] and Ding et al. [242] applied the ANSI/CAN/UL 2904 standard method for the measurement, but their results did not agree with each other due to the adoption of different experimental conditions. To minimize the effects of the printing variables on the measurement result, Chylek

et al. [240] and Sittichompoo et al. [241] both utilized the TGA method to directly measure emitted particles from a heated and melted filament in a tube furnace. However, the particle concentration measured by Chylek et al. [240] was significantly higher than that of Sittichompoo et al. [241] because of the use of much high carrier air flowrates by the latter. The measured particle geometric mean diameter (GMD) from the TGA method was also found to be smaller than those in most chamber studies (not shown in Table 3), which was attributed to the low level of particle condensation and coagulation (due to the reduced particle residence time in tube furnace) when using the TGA method [241]. Furthermore, the temperature in the heating tube was kept at the printing temperature for an entire tested filament sample, which reduces the particle condensation in the tube [240]. Note that the final size distribution of emitted particles by the TGA method highly depends on the heating uniformity in the tube furnace and the temperature gradient in the regions near the furnace outlet and sampling port [325, 326]. It is concluded that the measurement results can be significantly varied because of the difference on sampling methods and locations, air change rate, printing objects and filament features (Table A2.S1).

Different from the chamber sampling, this study used the developed sampler with multiple ports to uniformly sample particles emitted from the printing nozzle. To be mentioned that, both the printing head and cooling fan (except the fan inlet) were enclosed by the sampler, thus quickly capturing the characteristics of emitted particles (taking into the consideration of the aerosol dilution due to the cooling flow). In addition, for our investigation, the printing head was kept stationary (instead of moving) and the printing operation variables were kept constant for the printing with all the filaments. Uncertainties caused by the printing parameters and the

movement of the printing head were thus excluded. The obtained maximum concentrations of emitted particles from printing original PLA and white ABS were in the low and middle ranges, respectively, compared with that reported in the chamber studies. The above observation could be attributed to the accumulation of SVOC in the chamber studies. In addition to the maximum concentration, the time dependent concentrations, and GMDs of emitted particles from different experimental methods are discussed in next section.

A2.3.2 Particle emission characteristics

Fig. A2.2 compares the particle emission characteristics, variation of particle concentrations and GMDs, from printing original color PLA (PLA-O), iron-additive PLA (PLA-Fe) and white ABS (ABS-W) filaments by different measurement methods, i.e., by the designed sampler (case 1), in the chamber without (case 2) and with forced convection (case3). The measurement results for the carbon fiber PLA (PLA-C), fluorescent ABS (ABS-F) and glow in dark ABS (ABS-G) filaments are shown in Fig. A2.S1. The results in 5 mins of preheating and the initial 25 mins of printing were shown as they represented the major characteristics of the emission.

For the preheating, small particles with GMDs of 10–40 nm were measured after ~2 mins by all three methods with variations. Among the three methods, the sampler method first detected the presence of particle emissions for all three filaments while the chamber method with forced convection was the latest, indicating the high sensitivity of the sampler method. The particle emission during the preheating was resulted from the rapid heating (from room temperature to 210 ◦C in 5 mins) of residual filaments in the printing nozzle, leading to SVOC

emission and particle formation. Within 1 min, the nozzle temperature was raised from the room temperature to ~80 ◦C. Ding et al. [227] observed part of tested filaments began melting when the temperature reached 75 ◦C. The filament residues in the printing nozzle were activated after the first minute. No filament was extruding until the temperature reached ~180 ◦C after 2 mins (when a high level of SVOCs was readily to release). As the heat accumulated in the nozzle head, the overheated filament released SVOCs and particles in high concentration after the filament was flowed (dripped) out of the head. After 5 mins, the head was kept at 210 ◦C and the filament started to be extruded. Under the above printing condition, the effect of heat accumulation on the emission was no longer observed once a stable operation was reached, and the particle concentration and diameter were reduced to a low level. Notes that, only the sampler method was able to observe the stop of heat accumulation (concentration rise and reduction in the preheating) for all filaments. The chamber without forced convection can only observe the above dynamics for ABS-W filaments which released a relatively high concentration of SVOCs (compared with that releasing from the PLA filaments).

(a)

(b)
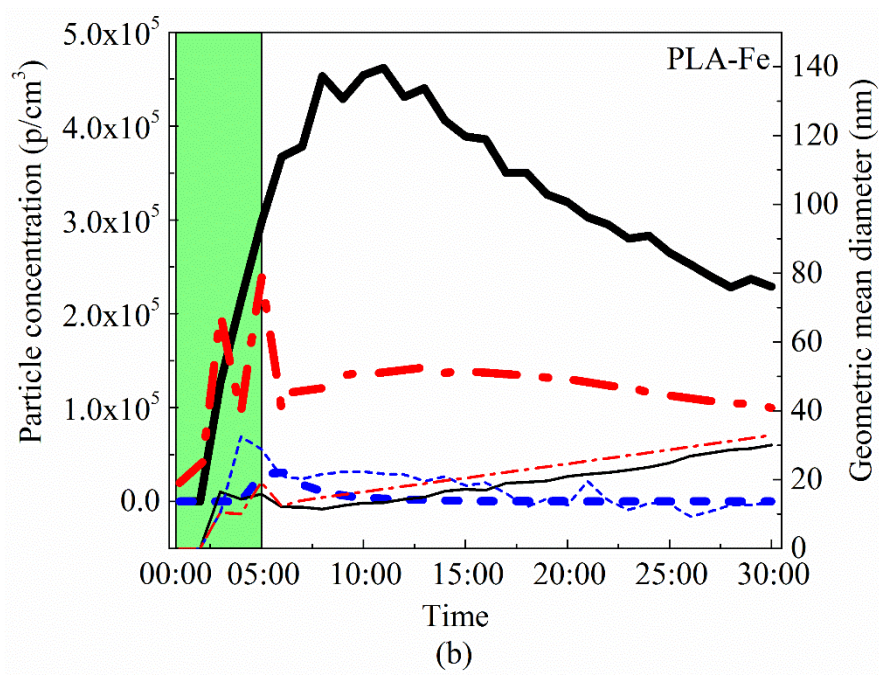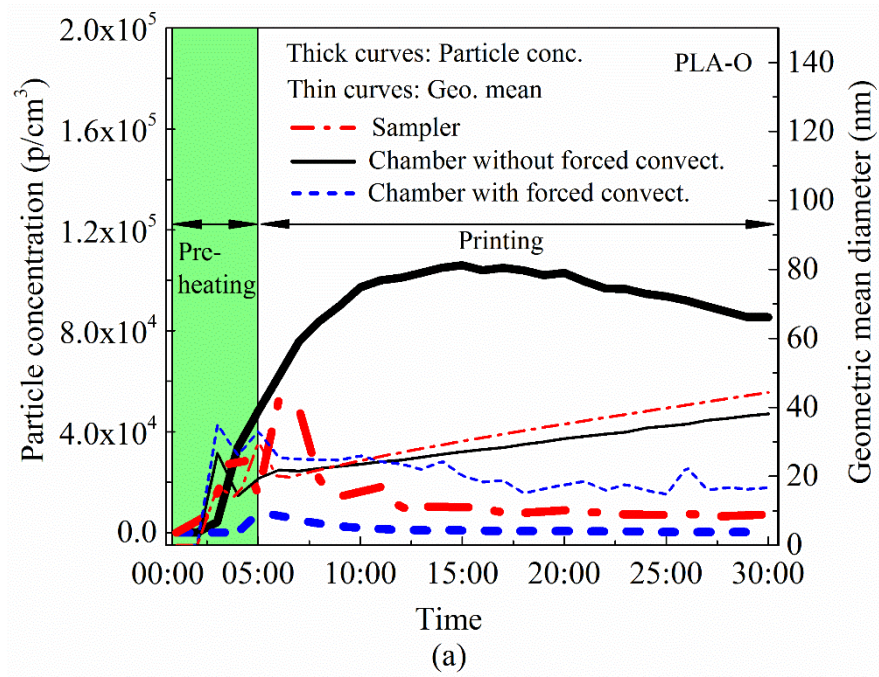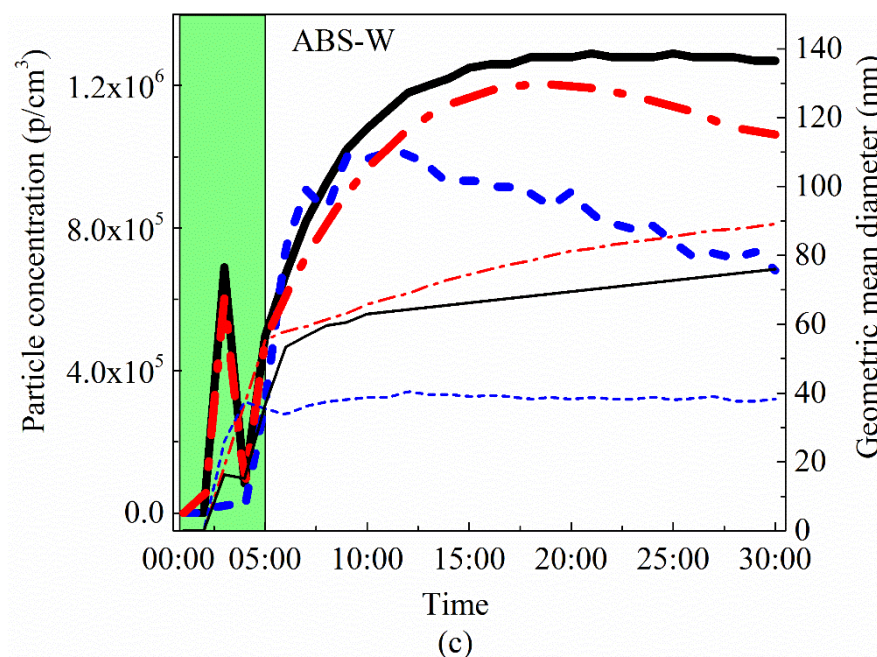
Figure A2.2 Total particle concentration before and during printing process: (a) PLA original filament, (b) PLA iron additive filament and (c) ABS original white filament.

At the beginning of the printing, the particle emission was increased again because of the filament extrusion. Based on measured time-dependent particle concentrations, it is found that not only measurement methods do cause the data variation but also different filaments. The chamber methods basically measured an increased particle concentration and reached the maximum at ~10–15 mins for three filaments. In comparison, the sampler method quickly reached the maximum concentration at the beginning of printing for the two PLAs. Between the two tested PLAs, the Fe additive obviously facilitated the particle formation [225, 243]. For ABS-W filament, it reached the maximum at ~15 mins. The above observation indicated the difference caused by the different properties of filaments where ABS emitted much higher quantities of SVOCs and formed more particles [221, 238]. As the particle concentration emitted by ABS-W was higher, the concentration gradient between nozzle head and the ambient was larger, causing stronger particle diffusion to the sampling area. Therefore, the

trend of the particle concentration for sampler and chamber method were similar. Moreover, due to the dilution effect from the cooling fan enclosed in the cup sampler, the particle concentration measured by the sampler method was lower than the chamber method.

By the chamber method with forced convection, it is found that the additional air flow effectively mixed with emitted particles and reduced the emitted particle concentration (except for ABS-G, to be discussed later). The GMD of measured size distributions were relatively constant during the printing. A similar trend was observed by the sampler method, i.e., the maximum concentration occurred at the beginning of printing for the PLAs and at ~10 mins for the ABS-W. Besides, the result measured by the chamber method with convection agreed with that obtained by the flow tube experiment designed to remove the heat accumulation around the printing head [227]. Different air change rates however could change the amount of accumulated heat around the nozzle, which changes the rate of SVOC condensation and particle formation, resulting in different concentration and mean size of particles. It is thus very challenging to find out a universal air change rate to characterize nucleation events for printing different filaments.

In the print of three other filaments (carbon PLA, fluorescent ABS and glow in dark ABS, Fig. A2.S1), similar trends with variations among three methods and with higher concentrations for ABSs than PLAs were observed. One exception was the glow in dark ABS (ABS-G) that started emitting particles from the beginning of preheating, which was detected by both sampler method and the chamber method with forced convection. The maximum concentration occurred relatively early indicating an early emission of high concentration and low vapor

167

pressure SVOCs from the residual filament. Low vapor pressure of SVOCs quickly formed nuclei and particles, thus a special caution should be taken when printing the ABS-G. The reason why the chamber method without convection could not detect the early particle emission under the above condition was unclear to the authors at this point and further investigation is required. A speculation was due to the missing of capturing the emission plume (without the mixing of additional air flow) by the chamber method without convection.

During the post printing period (not shown), the particle concentration quickly reduced due to the absence of SVOC sources and continuous coagulation. In general, the particle concentration reached the background level after ~30 mins. Also, different measurement methods resulted in different emission data. The measured particle emission concentrations were the highest by the chamber method without convection, and the lowest by the chamber method with convection. In terms of the GMDs of measured size distributions, a slight increase of the particle size for both sampler and chamber method without convection while it was relatively stable for the chamber method with convection. To reduce the measurement uncertainty, the sampler method should be more reliable than the other methods. The particle concentration, GMD and emission rate determined by the sampler method are summarized in Table A2.S2 of SI.

A2.3.3 Emission evaluation

Fig. A2.3 shows the emission rates (#/g) of different filaments based on the measurements by the sampler method. It is found the ABS filaments emitted more particles than PLA filaments, which is consistent with the finding of previous studies [221, 225, 238, 276]. In the

cases of PLA filaments, the one with the Fe additive emitted two orders of magnitude higher

in concentration than the original PLA. The lowest emission is found in the case of PLA-C

filament. The possible reason for the high emission rate of PLA-Fe filaments could be because

the Fe promoted the decomposition of the feedstock, thus releasing more SVOCs [225, 243].

The relative low emission in the case of PLA-C was due to the low ratio of the polyactide resin

(85% compared to the 92% to the PLA-O) in the filaments. In the cases with ABS filaments,

the ABS-W generated more particles than the other two additive ones. As the chemical

compositions of ABS filaments were not provided by the manufacture, we could not

hypothesize possible reasons. However, it is anticipated that the additives in newly developed

filaments suppress the release of SVOCs [245].
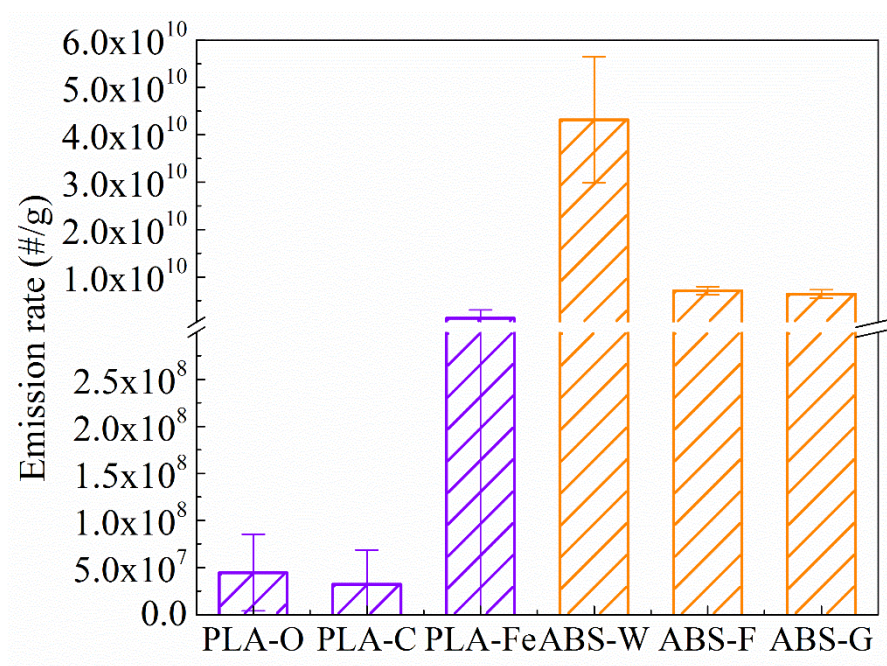
Figure A2.3. Total emission rate from different tested filaments measured by the sampler

method.

Fig.A2.4 shows the size-resolved total particle number emitted in the 155 mins (including in the 5 mins of preheating) for different filaments. It shows the size ranges having the highest particle number were 10–50 nm and 70–100 nm for PLA and ABS filaments, respectively, revealing the substantial difference of two types of filaments.
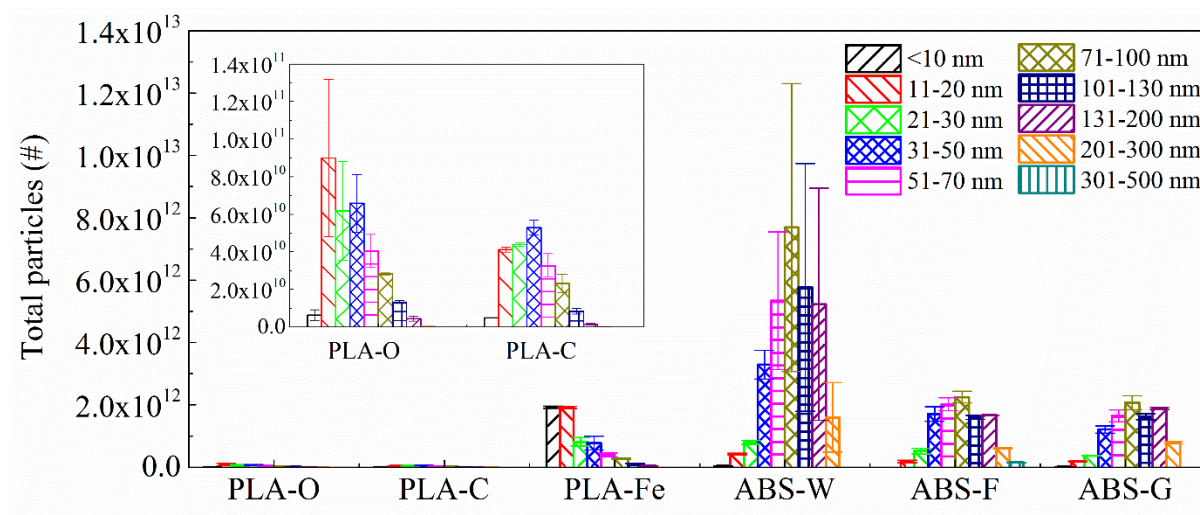
Figure A2.4. Size-resolved, total number of particles emitted in the printing of tested filaments for the first 150 minutes. The numerical data can be found in Table S2. Note that the measured size ranges of emitted particles were different in printing different filaments.

The stationary/stable emission level during the 3D printing of different filaments could be characterized by both total particle emission rate and size-resolved particle number, which have been applied in previous studies. To characterize the dynamics of emitted particles during the 3D printing, we proposed the dynamic emission index (DEI) defined by Eq. (A2.5). Not only does the DEI uncover the size interval having a high concentration but also provide the time dependent changes of size-dependent emission intensity during the 3D printing. More specifically, the increase of the DEI (growth of the curve) for a size interval indicates a net increase rate of smaller particles growing into this size interval due to condensation and/or

coagulation. On the other hand, the decline of the curve reveals a net loss rate of particles in this size interval due to their joining to larger particles. Comparing the DEI for different size intervals amongst different filaments, one can clearly see the different characteristics of different filaments. Fig. A2.5 shows the DEI of PLA-Fe and ABS-G filaments in the initial 30 mins of the printing (the major change in the emitted particle size distributions happened during this period). The result for other tested filaments can be found in Fig. A2.S2.

It is seen from Fig. A2.5 (a) that during the first 5 mins of pre-heating, the particles with the highest intensity were <10 nm and 11–20 nm for the PLA-Fe. Between 5 and 20 mins, the most dominant particles were in 11–20 nm, while the intensities of sub-10 nm, 21–30 nm and 31–50 nm particles were also high. It becomes clear that in the first 20 mins, the major sizes of produced particles by the PLA-Fe were sub-50 nm particles and caution should be paid as they have high deposition rate in deeper lung. During this time interval, modal distributions were seen for particles below 30 nm (<10, 11–20 and 21–30 nm), indicating these particles were experiencing condensation and/or coagulation to grow into the size interval where the DEI shows a growing trend. When the DEI was declining, particles in this size interval collided with other particles then reducing its intensity (concentration). For example, the DEI kept increasing from 5 to ~10 mins for the 11–20 nm particles, indicating its concentration was increasing due to ongoing condensation and/or coagulation of sub-10 nm to grow into 11–20 nm. Meanwhile, that rate was higher than that of 11–20 nm to join larger size intervals. In comparison, a clear increasing trend of DEI for 31–50 and 51–70 nm particles were seen, which indicates they were formed from smaller particles, meanwhile their rate to collide other

particles was low. Again, with the presentation of DEI, detailed information of emitted particles from the 3D printer can be easily and clearly identified.

Quite different results for ABS-G (Fig. A2.5b) compared with that of PLA-Fe were seen. It reveals the inherent difference between the two filaments. The major difference was that particles as large as 100 nm can be formed during the pre-heating for the ABS-G, suspecting there were unbounded solid particles (additives) released during the printing for the ABS-G. After the pre-heating, DEI of particles smaller than 70 nm continued reducing while it was increasing for particles larger than 70 nm. A similar trend for PLA-O and PLA-C and ABS-F can be seen from Fig. A2.S2. It is worth to note that particle size change for ABS-W mainly happened in the first ~10 mins of printing and then the particle sizes became stable.
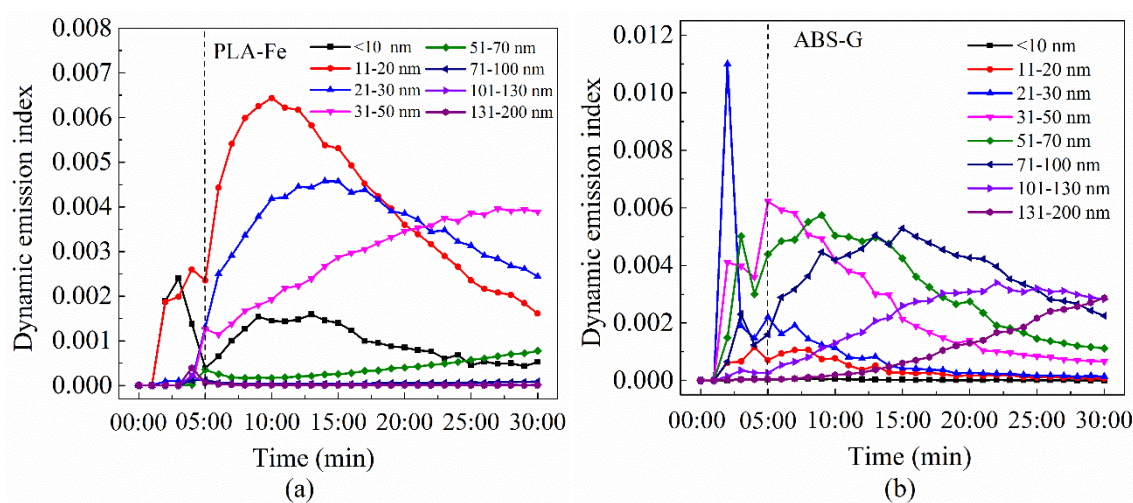
Figure A2.5. Dynamic emission index (DEI) as a function of printing time for (a) Fe-additive PLA filaments, and (b) glow-in-dark ABS filaments.

A2.4 Conclusion

This study proposed a new approach to characterize the instant and original emitted particles from 3D FDM printing. Particle emissions from printing six different filaments, i.e.,

172

the PLA original, PLA carbon-fiber, PLA iron additive, ABS white, ABS fluorescent and ABS glow-in-dark filaments were measured by the new method and the chamber methods (with and without forced convection). Results showed that the new method had the highest sensitivity and capability to characterize particle emissions. The same base material (ABS or PLA) but with different functionalities (additives) can lead to a large difference of characteristics of emitted particles.

Among the six different filaments, the emission rate of PLA-Fe filaments was two orders of magnitude higher than that of other two PLA filaments. The case with ABS-W filaments emitted 6–7 times more particles than those with ABS-F and ABS-G filaments. Our study also found that most particles released in the printing with PLA filaments were in the size range of 10–50 nm, while the modal sizes of particles emitted from the printing with ABS filaments were 70–100 nm. The developed new metric, dynamic emission index (DEI), allows one clearly to identify the change of emission intensity of different size intervals with time. The increase of the DEI for a certain size interval indicates a net increase rate of smaller particles growing into this size interval due to condensation and/or coagulation. On the other hand, the decline of the curve reveals a net loss rate of particles in this size interval due to their joining to larger particles.

A2.5 Support information

Table A2. S1. Summary of measurement conditions for different studies

	Sampling point	Air change rate (h^{-1})	Printing object	Measurement equipment and size range	PLA printing temperature, brand and color	ABS printing temperature, brand and color
Kim et al. [262]	-	0.56	Bobbin (5 x 5 x 3 cm)	SMPS, 10-420 nm	210-220 °C	250 °C
Stabile et al. [272]	2 m from the printer	-	Minion Dave (2.38 x 2.27 x3.58 cm)	SMPS, 6-220 nm	220 °C	-
Zhang et al. [238]	10 cm away from the nozzle	1	Extrusion	SMPS, 7-300 nm	210 °C, white	270 °C, green
Ding et al. [242]	0.5 m from the printer	3	Cube	SMPS, 10-420 nm	-	260 °C, Ecomaylene, white
Alberts et al. [225]	30 cm from the top of the chamber	0	Puck (5.08x 0.52 cm)	FMPS, 5.6-560 nm	220 °C, white	240 °C, transparent
Byrley et al. [304]	20 cm from the center of the printer	1	Standard NIST test object	SMPS, from 15.1 nm	220 °C	240 °C
Chylek et al. [240]	10 cm away from the nozzle	0.3 (chamber)/300 cm³/min (TGA)	Cylinder (2 x1 cm)	SMPS, 16-583 nm	200 °C, Polymaker, green	230 °C, Filamentum, red
Sittichompoo et al. [241]	-	1 (chamber) /127(TGA)	Flat	SMPS, 7.77-273 nm	-	230 °C white
This study	10 cm away from the nozzle	0.3	Extrusion	SMPS, 9.65-305.1 nm	210 °C, Polymaker, white	210 °C Gizmodorks, white
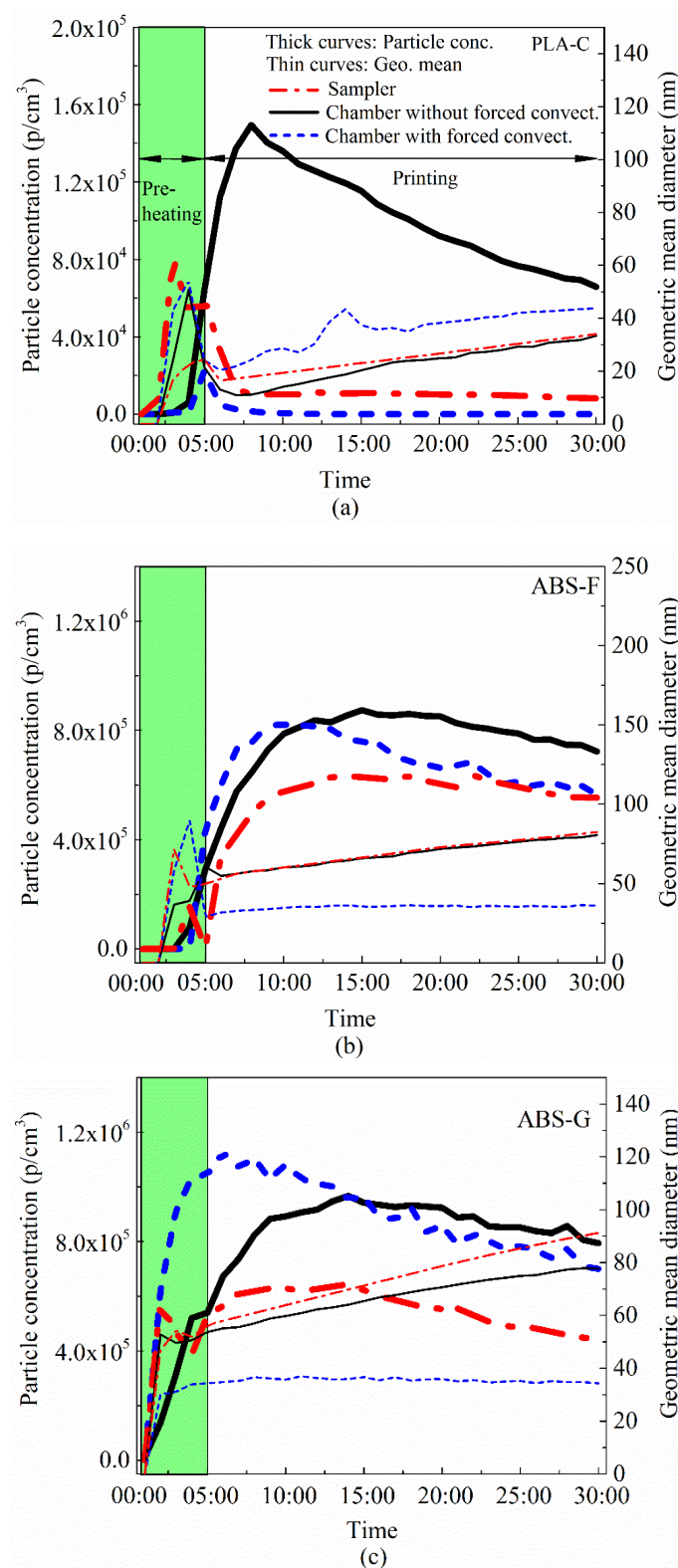
Figure A2.S1. Total particle concentration before and during printing process: (a) PLA carbon fiber filament, (b) ABS fluorescent filament and (c) ABS glow in dark filament.

Table A2.S2. Summary of particle measurements and emissions for different filaments (Case 2)

	Measurement equipment and size range	Average concentration (p/cm^3)	Average geo mean diameter (nm)	Emission rate (#/g)
PLA-O	SMPS (9.65-305.1 nm)	4.84 x 10^3	57.3	4.46 x 10^7
PLA-C	SMPS (9.65-305.1 nm)	4.34 x 10^3	70.0	3.22 x 10^7
PLA-Fe	SMPS (5.05-171.5 nm)	6.15 x 10^4	51.6	1.28 x 10^9
ABS-W	SMPS (9.65-305.1 nm)	9.39 x 10^5	87.6	4.32 x 10^{10}
ABS-F	SMPS (16-469.8 nm)	3.29 x 10^5	95.3	7.10 x 10^9
ABS-G	SMPS (9.65-305.1 nm)	2.98 x 10^5	94.2	6.35 x 10^9
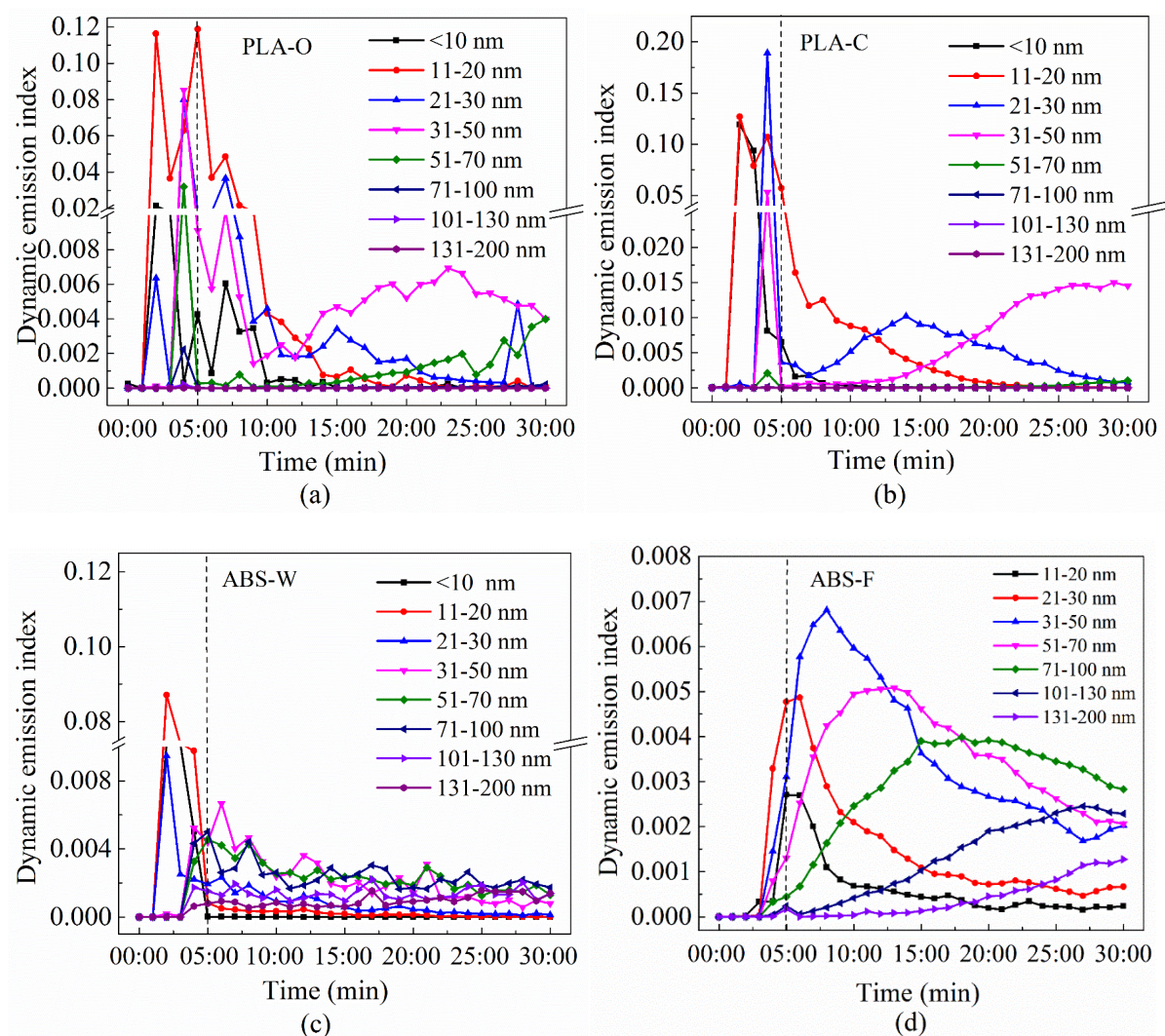
Figure A2.S2. Dynamic emission index for (a) PLA-O, (b) PLA-C, (c) ABS-W and (d) ABS-F.

Appendix II: Vita

EDUCATION

B.S., Heating, Ventilation, and Air conditioning Engineer, Beijing University of Civil Engineering and Architecture, China, 2009

M.S., Heating, Ventilation, and Air conditioning Engineer, Beijing University of Civil Engineering and Architecture, China, 2012

Ph.D., Heating, Ventilation, and Air conditioning Engineer, Tianjin University, China, 2017

Ph.D., student, Mechanical & Nuclear Engineering, Virginia Commonwealth University, 2019-2023.05.13 (Expected)

PUBLICATIONS (13 in total)

1. ***Jie Zhang,*** Wilson Poon, Sheng-Chieh Chen. 2023. Experimental and theoretical retentions of sub-10 nm colloidal nanoparticles by large-pore ultrafiltration membranes in isopropanol and water. *Journal of Membrane Science*, *121487*

2. ***Jie Zhang,*** Da-Ren Chen, and Sheng-Chieh Chen. 2022. A review of emission characteristics and control strategies for particles emitted from 3D fused deposition modeling (FDM) printing. *Building and Environment: 109348.*

3. ***Jie Zhang,*** Da-Ren Chen, and Sheng-Chieh Chen. 2022. Sampling and characterization of particle emission from the 3D FDM printing. *Journal of Building Engineering 52: 104476.*

4. ***Jie Zhang,*** Zhengwei Long. 2017. Study of the oil mist filtration performance: pressure drop characteristics and filter efficiency model. *Aerosol and Air Quality Research 17(4): 1063-1072.*

5. ***Jie Zhang,*** Yuan Shao, Zhengwei Long. 2016. Physicochemical characterization of oily particles emitted from different machining processes. *Journal of Aerosol Science, 96:1-13.*

6. ***Jie Zhang***, Zhengwei Long, Wei Liu, Qingyan Chen. 2016. Strategy for studying ventilation performance in factories. *Aerosol and Air Quality Research, 16: 442–452.*

7. ***Jie Zhang,*** Tianwei Liu, Sheng-Chieh Chen. Modeling and optimizing for sustainable design of ultrafiltration system using artificial neural network and particle swarm optimization (In process)

8. Ruikang He, ***Jie Zhang***, Gediminas Mainelis. 2022. Resuspension of particles deposited by nano-enabled consumer sprays: the role of product type, flooring material and resuspension. *Indoor air.*

9. Fan Zheng, Pan-pan Ji, ***Jie Zhang***, Doris Segets, Da-Ren Chen, and Sheng-Chieh Chen. 2021. Wavelet neural network modeling for the retention efficiency of sub-15 nm nanoparticles in ultrafiltration under small particle to pore diameter ratio. *Journal of Membrane Science: 119503.*

10. Wang, Congcong, ***Jie Zhang,*** Jiangyue Chao, Changle Yang, and Hongbing Chen. 2021. Evaluation of dynamic airflow structures in a single-aisle aircraft cabin mockup based on numerical simulation. *Indoor and Built Environment: 1420326X21992094.*

11. Congcong Wang, ***Jie Zhang***, Junjie Liu et al. 2021. Experimental study of thermo-fluid boundary conditions, airflow and temperature distributions in a single aisle aircraft cabin mockup. *Indoor and Built Environment 30(8), pp.1185-1199.*

12. Zhuangbo Feng, Junyan Yang, and ***Jie Zhang***. 2020. Numerical optimization on newly

developed electrostatic enhanced pleated air filters for efficient removal of airborne ultra-fine particles: Towards sustainable urban and built environment. *Sustainable Cities and Society 54: 102001.*

13. Wei Liu, Ruoyu You, ***Jie Zhang,*** Qingyan Chen. 2016. Development of a fast fluid dynamics-based adjoint method for the inverse design of indoor environments. *Journal of Building Performance Simulation, 1-18.*

CONFERENCE Presentations   (* Speaker/Presenter)

1. ***Jie Zhang****, Sheng-Chieh Chen, Measurement of Ultrafiltration Efficiency of NPs down to 2 nm in Chemicals and Optimization of Filtration Performance Using Machine Learning Technique. 62nd Semi-Annual Meeting, Center for Filtration Research (CFR), Oct. 10-11, 2022, Minnesota, US

2. ***Jie Zhang****, Sheng-Chieh Chen, Accurate measurement of particle emission from 3d printing processes and characterization of particles for additive filaments. AFS FiltCon 2021 Virtual Conference, April 19-21, 2021, US. (Poster)

3. ***Jie Zhang****, Sheng-Chieh Chen, Optimization of ultrafiltration for particles down to 2 nm through different membranes in IPA and chemicals. 61st Semi-Annual Meeting, Center for Filtration Research (CFR), May. 05-06, 2022, Minnesota, US

4. ***Jie Zhang****, Sheng-Chieh Chen, Measurement of Ultrafiltration Efficiency of NPs down to 2 nm in Chemicals and Optimization of Filtration Performance Using Machine Learning Technique. 60th Semi-Annual Meeting, Center for Filtration Research (CFR), Dec. 02-03, 2021, Minnesota, US

5. ***Jie Zhang****, Sheng-Chieh Chen, Membrane ultrafiltration in isopropyl alcohol (Chemicals) and optimization of operation conditions using radial basis function neural networks and particle swarm optimization algorithm. 59th Semi-Annual Meeting, Center for Filtration Research (CFR), Jun. 10-11, 2022, Minnesota, US

6. ***Jie Zhang****, Zheng Fan, Sheng-Chieh Chen, Membrane ultrafiltration for isopropyl alcohol cleanliness and recycling through combination of radial basis function neural networks and particle swarm optimization algorithm. 58th Semi-Annual Meeting, Center for Filtration Research (CFR), Nov. 05-06, 2022, Minnesota, US

HONORS AND AWARDS

- Dissertation scholarship awards ($9375), Virginia Commonwealth University, 2022
- Excellent Master thesis, Beijing University of Civil Engineering and Architecture 2012
- China National Scholarship, Beijing University of Civil Engineering and Architecture 2008
- China National Scholarship, Beijing University of Civil Engineering and Architecture 2007

SKILLS

- Strong research capabilities and statistical analysis skills
- Over 7 years of lab experience in conducting experiments about air filtration, liquid filtration and particle and VOC exposure

- Skills in prediction and optimization filtration using machine learning models
- Proficient in using SMPS, CPC, SEM, ICP-MS
- Proficient in CFD, Energyplus, Matlab
- Proven ability to write reports (12 publications) and present results (multiple presentations)
- Interact productively with people with diverse backgrounds

Teaching EXPERIENCE

Guest lecturer	University of Chicago	2022

MENTORING EXPERIENCE

Tianwei Liu	UMich, summer intern	2022
Mohammed Nabie	VCU, summer intern	2021

Reference:

1. Suhalim, N.S., N. Kasim, E. Mahmoudi, I.J. Shamsudin, A.W. Mohammad, F. Mohamed Zuki, and N.L.-A. Jamari, Rejection mechanism of ionic solute removal by nanofiltration membranes: An overview. Nanomaterials, 2022. 12(3): p. 437.
2. Mohammad, A.W., Y. Teow, W. Ang, Y. Chung, D. Oatley-Radcliffe, and N. Hilal, Nanofiltration membranes review: Recent advances and future prospects. Desalination, 2015. 356: p. 226-254.
3. Lin, S.H. and C.S. Wang, Recovery of isopropyl alcohol from waste solvent of a semiconductor plant. Journal of hazardous materials, 2004. 106(2-3): p. 161-168.
4. Hoefflinger, B., ITRS: The international technology roadmap for semiconductors, in Chips 2020: a guide to the future of nanoelectronics. 2011, Springer. p. 161-174.
5. Hu, S.-C., T. Lin, S.-H. Huang, B.-R. Fu, and M.-H. Hu, Energy savings approaches for high-tech manufacturing factories. Case Studies in Thermal Engineering, 2020. 17: p. 100569.
6. J., L., THE ELEC. 2018.
7. Chen, S.-C., D. Segets, T.-Y. Ling, W. Peukert, and D.Y. Pui, An experimental study of ultrafiltration for sub-10 nm quantum dots and sub-150 nm nanoparticles through PTFE membrane and Nuclepore filters. Journal of Membrane Science, 2016. 497: p. 153-161.
8. Lee, H., D. Segets, S. Süß, W. Peukert, S.-C. Chen, and D.Y. Pui, Retention mechanisms of 1.7 nm ZnS quantum dots and sub-20 nm Au nanoparticles in ultrafiltration membranes. Journal of Membrane Science, 2018. 567: p. 58-67.
9. Reinhardt, K. and W. Kern, Handbook of silicon wafer cleaning technology. 2018: William Andrew.
10. Leiknes, T., The effect of coupling coagulation and flocculation with membrane filtration in water treatment: A review. Journal of Environmental Sciences, 2009. 21(1): p. 8-12.
11. Madsen, H.T., Membrane filtration in water treatment–removal of micropollutants, in Chemistry of advanced environmental purification processes of water. 2014, Elsevier. p. 199-248.
12. Hube, S., M. Eskafi, K.F. Hrafnkelsdóttir, B. Bjarnadóttir, M.Á. Bjarnadóttir, S. Axelsdóttir, and B. Wu, Direct membrane filtration for wastewater treatment and resource recovery: A review. Science of the total environment, 2020. 710: p. 136375.
13. Pearce, G., Introduction to membranes: Filtration for water and wastewater treatment. Filtration & separation, 2007. 44(2): p. 24-27.
14. Mizuno, T., A. Namiki, S. Tsuzuki, and T. Numaguchi. A novel filter rating method for less than 30 nm particle. in 2008 International Symposium on Semiconductor Manufacturing (ISSM). 2008. IEEE.
15. Lipnizki, F., Industrial applications of ultrafiltration in pharmaceutical biotechnology. Engineering in life sciences, 2005. 5(1): p. 81-83.
16. Mohammad, A.W., C.Y. Ng, Y.P. Lim, and G.H. Ng, Ultrafiltration in food processing industry: review on application, membrane fouling, and fouling control. Food and bioprocess technology, 2012. 5: p. 1143-1156.
17. Park, J.-G., S.-H. Lee, J.-S. Ryu, Y.-K. Hong, T.-G. Kim, and A.A. Busnaina, Interfacial and electrokinetic characterization of IPA solutions related to semiconductor wafer drying and cleaning. Journal of the Electrochemical society, 2006. 153(9): p. G811.

18. Yin, Z., Y. Ma, B. Tanis-Kanbur, and J.W. Chew, Fouling behavior of colloidal particles in organic solvent ultrafiltration. Journal of Membrane Science, 2020. 599: p. 117836.
19. Takakura, T. and S. Tsuzuki. Particle removal efficiency evaluation of filters in IPA. in 2016 International Symposium on Semiconductor Manufacturing (ISSM). 2016. IEEE.
20. Berne, B.J. and R. Pecora, Dynamic light scattering: with applications to chemistry, biology, and physics. 2000: Courier Corporation.
21. Markus, A., P. Krystek, P. Tromp, J. Parsons, E. Roex, P. De Voogt, and R. Laane, Determination of metal-based nanoparticles in the river Dommel in the Netherlands via ultrafiltration, HR-ICP-MS and SEM. Science of the total environment, 2018. 631: p. 485-495.
22. Lee, H., S.-C. Chen, C. Kim, E. Westenburg, S.I. Moon, and D.Y. Pui, Evaluation of concentration measurement techniques of colloidal nanoparticles for microfiltration and ultrafiltration applications: Inductively coupled plasma-mass spectrometry, nanoparticle tracking analysis and electrospray-scanning mobility particle sizer. Separation and Purification Technology, 2017. 184: p. 34-42.
23. Chen, D.-R. and D.Y. Pui, Experimental investigation of scaling laws for electrospraying: dielectric constant effect. Aerosol science and technology, 1997. 27(3): p. 367-380.
24. Lee, H., D. Segets, S. Süß, W. Peukert, S.-C. Chen, and D.Y. Pui, Liquid filtration of nanoparticles through track-etched membrane filters under unfavorable and different ionic strength conditions: Experiments and modeling. Journal of Membrane Science, 2017. 524: p. 682-690.
25. Langford, A., M. Bruchsaler, and M. Gupta, Suspension properties and characterization of aluminum-adjuvanted vaccines, in Practical Aspects of Vaccine Development. 2022, Elsevier. p. 225-266.
26. Adair, J., E. Suvaci, and J. Sindel, Surface and colloid chemistry. 2001.
27. Lin, T., Z. Lu, and W. Chen, Interaction mechanisms and predictions on membrane fouling in an ultrafiltration system, using the XDLVO approach. Journal of Membrane Science, 2014. 461: p. 49-58.
28. Brant, J.A. and A.E. Childress, Assessing short-range membrane–colloid interactions using surface energetics. Journal of Membrane Science, 2002. 203(1-2): p. 257-273.
29. Wijenayaka, L.A., M.R. Ivanov, C.M. Cheatum, and A.J. Haes, Improved parametrization for extended Derjaguin, Landau, Verwey, and Overbeek predictions of functionalized gold nanosphere stability. The Journal of Physical Chemistry C, 2015. 119(18): p. 10064-10075.
30. Fjordbøge, A.S., B. Uthuppu, M.H. Jakobsen, S.V. Fischer, and M.M. Broholm, Mobility of electrostatically and sterically stabilized gold nanoparticles (AuNPs) in saturated porous media. Environmental Science and Pollution Research, 2019. 26: p. 29460-29472.
31. Trinh, T.A., Q. Han, Y. Ma, and J.W. Chew, Microfiltration of oil emulsions stabilized by different surfactants. Journal of Membrane Science, 2019. 579: p. 199-209.
32. Tanudjaja, H.J. and J.W. Chew, Assessment of oil fouling by oil-membrane interaction energy analysis. Journal of Membrane Science, 2018. 560: p. 21-29.
33. Kim, S., M. Marion, B.-H. Jeong, and E.M. Hoek, Crossflow membrane filtration of interacting nanoparticle suspensions. Journal of Membrane Science, 2006. 284(1-2): p. 361-372.
34. Park, J.-A. and S.-B. Kim, DLVO and XDLVO calculations for bacteriophage MS2 adhesion to iron oxide particles. Journal of Contaminant Hydrology, 2015. 181: p. 131-140.

35. Bergendahl, J.A. and D. Grasso, Mechanistic basis for particle detachment from granular media. Environmental Science & Technology, 2003. 37(10): p. 2317-2322.
36. Hahn, M.W. and C.R. O'Melia, Deposition and reentrainment of Brownian particles in porous media under unfavorable chemical conditions: Some concepts and applications. Environmental science & technology, 2004. 38(1): p. 210-220.
37. Lin, K., Z. Shen, Q. Liang, J. Xu, and H. Liu, The study of slag particle deposition process based on Monte Carlo simulation. Powder Technology, 2022. 407: p. 117630.
38. Koblinger, L. and W. Hofmann, Monte Carlo modeling of aerosol deposition in human lungs. Part I: Simulation of particle transport in a stochastic lung structure. Journal of Aerosol Science, 1990. 21(5): p. 661-674.
39. Hofmann, W. and L. Koblinger, Monte Carlo modeling of aerosol deposition in human lungs. Part II: Deposition fractions and their sensitivity to parameter variations. Journal of Aerosol Science, 1990. 21(5): p. 675-688.
40. Johnson, W., X. Li, and G. Yal, Colloid retention in porous media: Mechanistic confirmation of wedging and retention in zones of flow stagnation. Environmental science & technology, 2007. 41(4): p. 1279-1287.
41. Tufenkji, N. and M. Elimelech, Deviation from the classical colloid filtration theory in the presence of repulsive DLVO interactions. Langmuir, 2004. 20(25): p. 10818-10828.
42. Shen, C., B. Li, Y. Huang, and Y. Jin, Kinetics of coupled primary-and secondary-minimum deposition of colloids under unfavorable chemical conditions. Environmental science & technology, 2007. 41(20): p. 6976-6982.
43. Goh, G.D., S.L. Sing, and W.Y. Yeong, A review on machine learning in 3D printing: applications, potential, and challenges. Artificial Intelligence Review, 2021. 54(1): p. 63-94.
44. Reddy, Y., P. Viswanath, and B.E. Reddy, Semi-supervised learning: A brief review. Int. J. Eng. Technol, 2018. 7(1.8): p. 81.
45. Baker, B., O. Gupta, N. Naik, and R. Raskar, Designing neural network architectures using reinforcement learning. arXiv preprint arXiv:1611.02167, 2016.
46. Fetanat, M., M. Keshtiara, Z.-X. Low, R. Keyikoglu, A. Khataee, Y. Orooji, V. Chen, G. Leslie, and A. Razmjou, Machine learning for advanced design of nanocomposite ultrafiltration membranes. Industrial & Engineering Chemistry Research, 2021. 60(14): p. 5236-5250.
47. Gao, H., S. Zhong, R. Dangayach, and Y. Chen, Understanding and Designing a High-Performance Ultrafiltration Membrane Using Machine Learning. Environmental Science & Technology, 2023.
48. Zahmatkesh, S., M.K. Amiri, S.P.G. Zaferani, M.R.S. Emami, M. Hajiaghaei-Keshteli, M.D. Albaqami, A.M. Tighezza, M. Shafahi, and N. Han, Machine learning modeling of polycarbonate ultrafiltration membranes at different temperatures, Al2O3 nanoparticle volumes, and water ratios. Chemosphere, 2023. 313: p. 137424.
49. Rong-Ji, W., L. Xin-Hua, W. Qing-Ding, and W. Lingling, Optimizing process parameters for selective laser sintering based on neural network and genetic algorithm. The International Journal of Advanced Manufacturing Technology, 2009. 42: p. 1035-1042.
50. Ibrahim, M. and M. Norashikin, Pore Size Prediction of Polyethersulfone Ultrafiltration Membranes Using Artificial Neural Networks. Journal of Nanoscience and Nanotechnology, 2010. 10(9): p. 6211-6215.

51. Chen, H. and A.S. Kim, Prediction of permeate flux decline in crossflow membrane filtration of colloidal suspension: a radial basis function neural network approach. Desalination, 2006. 192(1-3): p. 415-428.

52. Sahoo, G.B. and C. Ray, Predicting flux decline in crossflow membranes using artificial neural networks and genetic algorithms. Journal of Membrane Science, 2006. 283(1-2): p. 147-157.

53. Yu, H., Y. Song, R. Liu, H. Pan, L. Xiang, and F. Qian, Identifying changes in dissolved organic matter content and characteristics by fluorescence spectroscopy coupled with self-organizing map and classification and regression tree analysis during wastewater treatment. Chemosphere, 2014. 113: p. 79-86.

54. Cabassud, M., N. Delgrange-Vincent, C. Cabassud, L. Durand-Bourlier, and J. Laine, Neural networks: a tool to improve UF plant productivity. Desalination, 2002. 145(1-3): p. 223-231.

55. Park, S., S.-S. Baek, J. Pyo, Y. Pachepsky, J. Park, and K.H. Cho, Deep neural networks for modeling fouling growth and flux decline during NF/RO membrane filtration. Journal of Membrane Science, 2019. 587: p. 117164.

56. Badrnezhad, R. and B. Mirza, Modeling and optimization of cross-flow ultrafiltration using hybrid neural network-genetic algorithm approach. Journal of Industrial and Engineering Chemistry, 2014. 20(2): p. 528-543.

57. Bowen, W.R., M.G. Jones, and H.N. Yousef, Dynamic ultrafiltration of proteins–A neural network approach. Journal of membrane science, 1998. 146(2): p. 225-235.

58. Bowen, W.R., M.G. Jones, and H.N. Yousef, Prediction of the rate of crossflow membrane ultrafiltration of colloids: A neural network approach. Chemical Engineering Science, 1998. 53(22): p. 3793-3802.

59. Zhao, Y., J.S. Taylor, and S. Chellam, Predicting RO/NF water quality by modified solution diffusion model and artificial neural networks. Journal of membrane science, 2005. 263(1-2): p. 38-46.

60. Alizadeh, M.J. and M.R. Kavianpour, Development of wavelet-ANN models to predict water quality parameters in Hilo Bay, Pacific Ocean. Marine pollution bulletin, 2015. 98(1-2): p. 171-178.

61. Curcio, S., V. Calabrò, and G. Iorio, Reduction and control of flux decline in cross-flow membrane processes modeled by artificial neural networks. Journal of Membrane Science, 2006. 286(1-2): p. 125-132.

62. Yang, L. and A. Shami, On hyperparameter optimization of machine learning algorithms: Theory and practice. Neurocomputing, 2020. 415: p. 295-316.

63. Fouskakis, D. and D. Draper, Stochastic optimization: a review. International Statistical Review, 2002. 70(3): p. 315-349.

64. Birbil, Ş.İ., S.-C. Fang, and R.-L. Sheu, On the convergence of a population-based global optimization algorithm. Journal of global optimization, 2004. 30: p. 301-318.

65. Bi, W., G.C. Dandy, and H.R. Maier, Improved genetic algorithm optimization of water distribution system design by incorporating domain knowledge. Environmental Modelling & Software, 2015. 69: p. 370-381.

66. Xia, X., L. Gui, G. He, C. Xie, B. Wei, Y. Xing, R. Wu, and Y. Tang, A hybrid optimizer based on firefly algorithm and particle swarm optimization algorithm. Journal of computational science, 2018. 26: p. 488-500.

67. Asadi-Eydivand, M., M. Solati-Hashjin, A. Fathi, M. Padashi, and N.A.A. Osman, Optimal design of a 3D-printed scaffold using intelligent evolutionary algorithms. Applied Soft Computing, 2016. 39: p. 36-47.

68. Luitel, B. and G.K. Venayagamoorthy. Differential evolution particle swarm optimization for digital filter design. in 2008 IEEE Congress on Evolutionary Computation (IEEE World Congress on Computational Intelligence). 2008. IEEE.

69. Ababneh, J.I. and M.H. Bataineh, Linear phase FIR filter design using particle swarm optimization and genetic algorithms. Digital Signal Processing, 2008. 18(4): p. 657-668.

70. Fetimi, A., A. Dâas, Y. Benguerba, S. Merouani, M. Hamachi, O. Kebiche-Senhadji, and O. Hamdaoui, Optimization and prediction of safranin-O cationic dye removal from aqueous solution by emulsion liquid membrane (ELM) using artificial neural network-particle swarm optimization (ANN-PSO) hybrid model and response surface methodology (RSM). Journal of Environmental Chemical Engineering, 2021. 9(5): p. 105837.

71. Bagheri, M., S.A. Mirbagheri, A.M. Kamarkhani, and Z. Bagheri, Modeling of effluent quality parameters in a submerged membrane bioreactor with simultaneous upward and downward aeration treating municipal wastewater using hybrid models. Desalination and Water Treatment, 2016. 57(18): p. 8068-8089.

72. Ye, M., X. Wang, and Y. Xu, Parameter identification for proton exchange membrane fuel cell model using particle swarm optimization. International journal of hydrogen energy, 2009. 34(2): p. 981-989.

73. Yusuf, Z., N.A. Wahab, and S. Sahlan, Modeling of filtration process using PSO-neural network. Journal of Telecommunication, Electronic and Computer Engineering (JTEC), 2017. 9(3): p. 15-19.

74. Chithra, K., A. Srinivasan, V. Vijayalakshmi, and A. Asuntha, PID controller tuning in reverse osmosis system based on particle swarm optimization. International Journal of Scientific & Technology, 2015. 3: p. 351-358.

75. Madaeni, S., N.T. Hasankiadeh, A. Kurdian, and A. Rahimpour, Modeling and optimization of membrane fabrication using artificial neural network and genetic algorithm. Separation and purification technology, 2010. 76(1): p. 33-43.

76. Wei, W., O. Ramalho, L. Malingre, S. Sivanantham, J.C. Little, and C. Mandin, Machine learning and statistical models for predicting indoor air quality. Indoor Air, 2019. 29(5): p. 704-726.

77. McCarthy, W.P., H.N. Blais, T.F. O'Callaghan, M. Hossain, M. Moloney, M. Danaher, C. O'Connor, and J.T. Tobin, Application of nanofiltration for the removal of chlorate from skim milk. International Dairy Journal, 2022. 128: p. 105321.

78. Chou, M.L., L.T. Lin, D. Devos, and T. Burnouf, Nanofiltration to remove microparticles and decrease the thrombogenicity of plasma: in vitro feasibility assessment. Transfusion, 2015. 55(10): p. 2433-2444.

79. Fallahianbijan, F., S. Giglia, C. Carbrello, D. Bell, and A.L. Zydney, Impact of protein fouling on nanoparticle capture within the Viresolve® Pro and Viresolve® NFP virus removal membranes. Biotechnology and bioengineering, 2019. 116(9): p. 2285-2291.

80. Shi, Y.-T., X. Meng, L. Yao, and M. Tian, A full-scale study of nanofiltration: Separation and recovery of NaCl and Na2SO4 from coal chemical industry wastewater. Desalination, 2021. 517: p. 115239.

81. Shon, H., S. Phuntsho, D. Chaudhary, S. Vigneswaran, and J. Cho, Nanofiltration for water and wastewater treatment–a mini review. Drinking Water Engineering and Science, 2013. 6(1): p. 47-53.

82. Moreno, M., L.P. Mazur, S.E. Weschenfelder, R.J. Regis, R.A. de Souza, B.A. Marinho, A. da Silva, S.M.G.U. de Souza, and A.A.U. de Souza, Water and wastewater treatment by micellar enhanced ultrafiltration–A critical review. Journal of Water Process Engineering, 2022. 46: p. 102574.

83. Tsuzuki, S. Evauation of particle removal efficiency of filters in high temperature sulfuric acid using 30 nm liquid particle counter—Tomoyuki Takakura. in 2015 Joint e-Manufacturing and Design Collaboration Symposium (eMDC) & 2015 International Symposium on Semiconductor Manufacturing (ISSM). 2015. IEEE.

84. International technology roadmap for devices and systems. 2022 update. Yield Enhancement: p. 12.

85. Li, X., S. De Feyter, and I.F. Vankelecom, Poly (sulfone)/sulfonated poly (ether ether ketone) blend membranes: Morphology study and application in the filtration of alcohol based feeds. Journal of Membrane Science, 2008. 324(1-2): p. 67-75.

86. Kochan, J., T. Wintgens, R. Hochstrat, and T. Melin, Impact of wetting agents on the filtration performance of polymeric ultrafiltration membranes. Desalination, 2009. 241(1-3): p. 34-42.

87. Knotter, D.M., S.A. Wolters, and M.A. Kasanrokijat, Particle concentration measurements in process liquids using light-scattering techniques. Particulate Science and Technology, 2007. 25(5): p. 435-447.

88. Kaszuba, M., D. McKnight, M.T. Connah, F.K. McNeil-Watson, and U. Nobbmann, Measuring sub nanometre sizes using dynamic light scattering. Journal of nanoparticle research, 2008. 10: p. 823-829.

89. Filipe, V., A. Hawe, and W. Jiskoot, Critical evaluation of Nanoparticle Tracking Analysis (NTA) by NanoSight for the measurement of nanoparticles and protein aggregates. Pharmaceutical research, 2010. 27: p. 796-810.

90. Meijerink, M.J., K.P. De Jong, and J. Zečević, Growth of supported gold nanoparticles in aqueous phase studied by in situ transmission electron microscopy. The Journal of Physical Chemistry C, 2019. 124(3): p. 2202-2212.

91. Amendola, V. and M. Meneghetti, Size evaluation of gold nanoparticles by UV− vis spectroscopy. The Journal of Physical Chemistry C, 2009. 113(11): p. 4277-4285.

92. Jreije, I., M. Hadioui, and K.J. Wilkinson, Sample preparation for the analysis of nanoparticles in natural waters by single particle ICP-MS. Talanta, 2022. 238: p. 123060.

93. Raja, P.M.V., Barron, A. R., , UV-Visible Spectroscopy. Rice University, 2021.

94. Greiner, R., V. Gräf, A. Burcza, B. Hetzer, J. Milsmann, and E. Walz, Engineered Nanomaterials in the Food Sector, in Comprehensive Analytical Chemistry. 2015, Elsevier. p. 579-616.

95. Tsai, D., R. Zangmeister, L. Pease Iii, M. Tarlov, and M. Zachariah, Gas-phase ion-mobility characterization of SAM-functionalized Au nanoparticles. Langmuir, 2008. 24(16): p. 8483-8490.

96. Komada, S., T. Kobayashi, Y. Arao, K. Tsuchiya, and Y. Mori, Optical properties of manganese-doped zinc sulfide nanoparticles classified by size using poor solvent. Advanced Powder Technology, 2012. 23(6): p. 872-877.

97. Segets, D., S. Komada, B. Butz, E. Spiecker, Y. Mori, and W. Peukert, Quantitative evaluation of size selective precipitation of Mn-doped ZnS quantum dots by size distributions calculated from UV/Vis absorbance spectra. Journal of nanoparticle research, 2013. 15: p. 1-13.

98. Van der Bruggen, B., C. Vandecasteele, T. Van Gestel, W. Doyen, and R. Leysen, A review of pressure‑driven membrane processes in wastewater treatment and drinking water production. Environmental progress, 2003. 22(1): p. 46-56.

99. Bottino, A., G. Capannelli, A. Comite, C. Costa, R. Firpo, A. Jezowska, and M. Pagliero, Treatment of olive mill wastewater through integrated pressure-driven membrane processes. Membranes, 2020. 10(11): p. 334.

100. Al Abdulgader, H., V. Kochkodan, and N. Hilal, Hybrid ion exchange–Pressure driven membrane processes in water treatment: A review. Separation and Purification Technology, 2013. 116: p. 253-264.

101. Luque, S., D. Gómez, and J.R. Álvarez, Industrial applications of porous ceramic membranes (pressure‑driven processes). Membrane Science and Technology, 2008. 13: p. 177-216.

102. Garnier, C., W. Guiga, L. Marie-Laure, and C. Fargues, Water reuse in the food processing industries: A review on pressure-driven membrane processes as reconditioning treatments. Journal of Food Engineering, 2022: p. 111397.

103. Kimura, K., S. Toshima, G. Amy, and Y. Watanabe, Rejection of neutral endocrine disrupting compounds (EDCs) and pharmaceutical active compounds (PhACs) by RO membranes. Journal of membrane science, 2004. 245(1-2): p. 71-78.

104. Ozay, Y., S. Ozdemir, S. Gonca, O. Canli, and N. Dizge, Phenolic compounds recovery from pistachio hull using pressure-driven membrane process and a cleaner production of biopesticide. Environmental Technology & Innovation, 2021. 24: p. 101993.

105. Haerens, K., S. Van Deuren, E. Matthijs, and B. Van der Bruggen, Challenges for recycling ionic liquids by using pressure driven membrane processes. Green Chemistry, 2010. 12(12): p. 2182-2188.

106. Cha, M., C. Boo, and C. Park, Simultaneous retention of organic and inorganic contaminants by a ceramic nanofiltration membrane for the treatment of semiconductor wastewater. Process Safety and Environmental Protection, 2022. 159: p. 525-533.

107. Cui, Z., Y. Jiang, and R. Field, Fundamentals of pressure-driven membrane separation processes, in Membrane technology. 2010, Elsevier. p. 1-18.

108. Jelen, P., Pressure-driven membrane processes: principles and definitions. New applications of membrane processes., 1992: p. 7-14.

109. Elimelech, M., J. Gregory, and X. Jia, Particle deposition and aggregation: measurement, modelling and simulation. 2013: Butterworth-Heinemann.

110. Van Oss, C.J., Interfacial forces in aqueous media. 2006: CRC press.

111. Fan, Z., P.-p. Ji, J. Zhang, D. Segets, D.-R. Chen, and S.-C. Chen, Wavelet neural network modeling for the retention efficiency of sub-15 nm nanoparticles in ultrafiltration under small particle to pore diameter ratio. Journal of membrane science, 2021. 635: p. 119503.

112. He, Z., S. Kasemset, A.Y. Kirschner, Y.-H. Cheng, D.R. Paul, and B.D. Freeman, The effects of salt concentration and foulant surface charge on hydrocarbon fouling of a poly (vinylidene fluoride) microfiltration membrane. Water research, 2017. 117: p. 230-241.

113.   Yin, Z., R.J.E. Yeow, Y. Ma, and J.W. Chew, Link between interfacial interaction and membrane fouling during organic solvent ultrafiltration of colloidal foulants. Journal of Membrane Science, 2020. 611: p. 118369.

114.   Hinds, W.C., Aerosol technology: properties, behavior, and measurement of airborne particles. 1999: John Wiley & Sons.

115.   Manton, M., Brownian diffusion of aerosols to the face of a nuclepore filter. Atmospheric Environment (1967), 1979. 13(4): p. 525-531.

116.   Spurny, K., J.P. Lodge, E.R. Frank, and D.C. Sheesley, Aerosol filtration by means of Nuclepore filters: structural and filtration properties. Environmental Science & Technology, 1969. 3(5): p. 453-464.

117.   Twomey, S., Equations for the decay of diffusion of particles in an aerosol flowing through circular or rectangular channels. Bull Observ Puy de Dome, 1962. 10: p. 173-180.

118.   Ruckenstein, E. and D.C. Prieve, Adsorption and desorption of particles and their chromatographic separation. AIChE Journal, 1976. 22(2): p. 276-283.

119.   Gregory, J., Approximate expressions for retarded van der Waals interaction. Journal of colloid and interface science, 1981. 83(1): p. 138-145.

120.   Israelachvili, J.N., Intermolecular and surface forces. 2011: Academic press.

121.   Bhattacharjee, S., A. Sharma, and P.K. Bhattacharya, Estimation and influence of long range solute. Membrane interactions in ultrafiltration. Industrial & engineering chemistry research, 1996. 35(9): p. 3108-3121.

122.   Bhattacharjee, S. and A. Sharma, Apolar, polar, and electrostatic interactions of spherical particles in cylindrical pores. Journal of colloid and interface science, 1997. 187(1): p. 83-95.

123.   Van Oss, C., A. Docoslis, W. Wu, and R. Giese, Influence of macroscopic and microscopic interactions on kinetic rate constants: I. Role of the extended DLVO theory in determining the kinetic adsorption constant of proteins in aqueous media, using von Smoluchowski's approach. Colloids and Surfaces B: Biointerfaces, 1999. 14(1-4): p. 99-104.

124.   Van Oss, C., Acid—base interfacial interactions in aqueous media. Colloids and Surfaces A: Physicochemical and Engineering Aspects, 1993. 78: p. 1-49.

125.   Cornelissen, E., T. Van den Boomgaard, and H. Strathmann, Physicochemical aspects of polymer selection for ultrafiltration and microfiltration membranes. Colloids and surfaces A: Physicochemical and engineering aspects, 1998. 138(2-3): p. 283-289.

126.   Sood, V., S. Dhar, and D.S. Katti, Quantitative Estimation of Long-Range Interactions at the Nanoscale. bioRxiv, 2018: p. 478800.

127.   Tolman, R.C., The effect of droplet size on surface tension. The journal of chemical physics, 1949. 17(3): p. 333-337.

128.   Biggs, S., Steric and bridging forces between surfaces bearing adsorbed polymer: an atomic force microscopy study. Langmuir, 1995. 11(1): p. 156-162.

129.   Butt, H.-J., M. Kappl, H. Mueller, R. Raiteri, W. Meyer, and J. Rühe, Steric forces measured with the atomic force microscope at various temperatures. Langmuir, 1999. 15(7): p. 2559-2565.

130.   Scaffardi, L.B. and J.O. Tocho, Size dependence of refractive index of gold nanoparticles. Nanotechnology, 2006. 17(5): p. 1309.

131.   Vafaei, S. and M. Podowski, Analysis of the relationship between liquid droplet size and contact angle. Advances in Colloid and Interface Science, 2005. 113(2-3): p. 133-146.

132.   Zakria, H.S., M.H.D. Othman, R. Kamaludin, M.A. Rahman, J. Jaafar, and A.F. Ismail, The use of PVDF membrane for wastewater treatment, in Emerging Techniques for Treatment of Toxic Metals from Wastewater. 2023, Elsevier. p. 289-318.

133.   Men, Y., Z. Li, L. Zhu, X. Wang, S. Cheng, and Y. Lyu, New insights into membrane fouling during direct membrane filtration of municipal wastewater and fouling control with mechanical strategies. Science of The Total Environment, 2023. 869: p. 161775.

134.   Günay, M.G., U. Kemerli, C. Karaman, O. Karaman, A. Güngör, and H. Karimi-Maleh, Review of functionalized nano porous membranes for desalination and water purification: MD simulations perspective. Environmental Research, 2023. 217: p. 114785.

135.   Kim, T.-H., C. Park, and S. Kim, Water recycling from desalination and purification process of reactive dye manufacturing industry by combined membrane filtration. Journal of Cleaner Production, 2005. 13(8): p. 779-786.

136.   Wang, L.K., N.K. Shammas, M. Cheryan, Y.-M. Zheng, and S.-W. Zou, Treatment of food industry foods and wastes by membrane filtration. Membrane and Desalination Technologies, 2011: p. 237-269.

137.   El Fadil, A., R. Verbeke, M. Kyburz, P.E. Aerts, and I.J. Vankelecom, From academia to industry: Success criteria for upscaling nanofiltration membranes for water and solvent applications. Journal of Membrane Science, 2023: p. 121393.

138.   Takakura, T., S. Daikoku, and S. Tsuzuki. Particle removal efficiency evaluation of filters in high temperature IPA. in 2017 Joint International Symposium on e-Manufacturing and Design Collaboration (eMDC) & Semiconductor Manufacturing (ISSM). 2017. IEEE.

139.   Zhang, J., W. Poon, and S.-C. Chen, Experimental and theoretical retentions of sub-10 nm colloidal nanoparticles by large-pore ultrafiltration membranes in isopropanol and water. Journal of Membrane Science, 2023. 674: p. 121487.

140.   Xu, Q. and J. Jiang, Recent development in machine learning of polymer membranes for liquid separation. Molecular Systems Design & Engineering, 2022.

141.   Rall, D., A.M. Schweidtmann, M. Kruse, E. Evdochenko, A. Mitsos, and M. Wessling, Multi-scale membrane process optimization with high-fidelity ion transport models through machine learning. Journal of Membrane Science, 2020. 608: p. 118208.

142.   Jawad, J., A.H. Hawari, and S.J. Zaidi, Artificial neural network modeling of wastewater treatment and desalination using membrane processes: A review. Chemical Engineering Journal, 2021. 419: p. 129540.

143.   Bagheri, M., A. Akbari, and S.A. Mirbagheri, Advanced control of membrane fouling in filtration systems using artificial intelligence and machine learning techniques: A critical review. Process Safety and Environmental Protection, 2019. 123: p. 229-252.

144.   Yusuf, Z., N.A. Wahab, and S. Sudin, Soft computing techniques in modelling of membrane filtration system: A review. Desalin. Water Treat, 2019. 161: p. 144-155.

145.   Dornier, M., M. Decloux, G. Trystram, and A. Lebert, Dynamic modeling of crossflow microfiltration using neural networks. Journal of membrane science, 1995. 98(3): p. 263-273.

146.   Rahmanian, B., M. Pakizeh, S.A.A. Mansoori, and R. Abedini, Application of experimental design approach and artificial neural network (ANN) for the determination of potential micellar-enhanced ultrafiltration process. Journal of Hazardous materials, 2011. 187(1-3): p. 67-74.

147.   Liu, Q.-F. and S.-H. Kim, Evaluation of membrane fouling models based on bench-scale experiments: a comparison between constant flowrate blocking laws and artificial neural network (ANNs) model. Journal of Membrane Science, 2008. 310(1-2): p. 393-401.

148.   Corbatón-Báguena, M.-J., M.-C. Vincent-Vela, J.-M. Gozálvez-Zafrilla, S. Álvarez-Blanco, J. Lora-García, and D. Catalán-Martínez, Comparison between artificial neural networks and Hermia's models to assess ultrafiltration performance. Separation and Purification Technology, 2016. 170: p. 434-444.

149.   Shetty, G.R. and S. Chellam, Predicting membrane fouling during municipal drinking water nanofiltration using artificial neural networks. Journal of Membrane Science, 2003. 217(1-2): p. 69-86.

150.   Darwish, N., N. Hilal, H. Al-Zoubi, and A. Mohammad, Neural networks simulation of the filtration of sodium chloride and magnesium chloride solutions using nanofiltration membranes. Chemical Engineering Research and Design, 2007. 85(4): p. 417-430.

151.   Purkait, M., V.D. Kumar, and D. Maity, Treatment of leather plant effluent using NF followed by RO and permeate flux prediction using artificial neural network. Chemical Engineering Journal, 2009. 151(1-3): p. 275-285.

152.   Barello, M., D. Manca, R. Patel, and I.M. Mujtaba, Neural network based correlation for estimating water permeability constant in RO desalination process under fouling. Desalination, 2014. 345: p. 101-111.

153.   Al-Shayji, K.A., Modeling, simulation, and optimization of large-scale commercial desalination plants. 1998, Virginia Polytechnic Institute and State University.

154.   Madaeni, S., M. Shiri, and A. Kurdian, Modeling, optimization, and control of reverse osmosis water treatment in kazeroon power plant using neural network. Chemical Engineering Communications, 2015. 202(1): p. 6-14.

155.   Al-Abri, M. and N. Hilal, Artificial neural network simulation of combined humic substance coagulation and membrane filtration. Chemical Engineering Journal, 2008. 141(1-3): p. 27-34.

156.   Sargolzaei, J., M.H. Asl, and A.H. Moghaddam, Membrane permeate flux and rejection factor prediction using intelligent systems. Desalination, 2012. 284: p. 92-99.

157.   Aydiner, C., I. Demir, and E. Yildiz, Modeling of flux decline in crossflow microfiltration using neural networks: the case of phosphate removal. Journal of membrane science, 2005. 248(1-2): p. 53-62.

158.   Aydiner, C., I. Demir, B. Keskinler, and O. Ince, Joint analysis of transient flux behaviors via membrane fouling in hybrid PAC/MF processes using neural network. Desalination, 2010. 250(1): p. 188-196.

159.   Chellam, S., Artificial neural network model for transient crossflow microfiltration of polydispersed suspensions. Journal of Membrane Science, 2005. 258(1-2): p. 35-42.

160.   Liu, Q.-F., S.-H. Kim, and S. Lee, Prediction of microfiltration membrane fouling using artificial neural network models. Separation and Purification Technology, 2009. 70(1): p. 96-102.

161.   Strugholtz, S., S. Panglisch, J. Gebhardt, and R. Gimbel, Neural networks and genetic algorithms in membrane technology modelling. Journal of Water Supply: Research and Technology—AQUA, 2008. 57(1): p. 23-34.

162.   Nandi, B., A. Moparthi, R. Uppaluri, and M. Purkait, Treatment of oily wastewater using low cost ceramic membrane: Comparative assessment of pore blocking and artificial neural network models. chemical engineering research and design, 2010. 88(7): p. 881-892.

163.   Shokrkar, H., A. Salahi, N. Kasiri, and T. Mohammadi, Mullite ceramic membranes for industrial oily wastewater treatment: experimental and neural network modeling. Water Science and Technology, 2011. 64(3): p. 670-676.

164.   Liu, Y., G. He, M. Tan, F. Nie, and B. Li, Artificial neural network model for turbulence promoter-assisted crossflow microfiltration of particulate suspensions. Desalination, 2014. 338: p. 57-64.

165.   Rahmanian, B., M. Pakizeh, S.A.A. Mansoori, M. Esfandyari, D. Jafari, H. Maddah, and A. Maskooki, Prediction of MEUF process performance using artificial neural networks and ANFIS approaches. Journal of the Taiwan Institute of Chemical Engineers, 2012. 43(4): p. 558-565.

166.   Niemi, H., A. Bulsari, and S. Palosaari, Simulation of membrane separation by neural networks. Journal of membrane science, 1995. 102: p. 185-191.

167.   Delgrange, N., C. Cabassud, M. Cabassud, L. Durand-Bourlier, and J. Laine, Modelling of ultrafiltration fouling by neural network. Desalination, 1998. 118(1-3): p. 213-227.

168.   Delgrange, N., C. Cabassud, M. Cabassud, L. Durand-Bourlier, and J. Laine, Neural networks for prediction of ultrafiltration transmembrane pressure–application to drinking water production. Journal of membrane science, 1998. 150(1): p. 111-123.

169.   Chew, C.M., M. Aroua, and M. Hussain, A practical hybrid modelling approach for the prediction of potential fouling parameters in ultrafiltration membrane water treatment plant. Journal of Industrial and Engineering Chemistry, 2017. 45: p. 145-155.

170.   Teodosiu, C., O. Pastravanu, and M. Macoveanu, Neural network models for ultrafiltration and backwashing. Water Research, 2000. 34(18): p. 4371-4380.

171.   Bhattacharjee, C. and M. Singh, Studies on the applicability of artificial neural network (ANN) in continuous stirred ultrafiltration. Chemical Engineering & Technology: Industrial Chemistry‐Plant Equipment‐Process Engineering‐Biotechnology, 2002. 25(12): p. 1187-1192.

172.   Oh, H., M. Yu, E. Gwon, J. Koo, S. Kim, and A. Koizumi, KNT-artificial neural network model for flux prediction of ultrafiltration membrane producing drinking water. Water Science and Technology, 2004. 50(8): p. 103-110.

173.   Kabsch-Korbutowicz, M. and M. Kutylowska, Use of artificial intelligence in predicting the turbidity retention coefficient during ultrafiltration of water. Environment Protection Engineering, 2011. 37(2): p. 75-84.

174.   Lin, W., L. Jing, Z. Zhu, Q. Cai, and B. Zhang, Removal of heavy metals from mining wastewater by Micellar-Enhanced Ultrafiltration (MEUF): experimental investigation and Monte Carlo-based artificial neural network modeling. Water, Air, & Soil Pollution, 2017. 228: p. 1-11.

175.   Soleimani, R., N.A. Shoushtari, B. Mirza, and A. Salahi, Experimental investigation, modeling and optimization of membrane separation using artificial neural network and multi-objective optimization using genetic algorithm. Chemical engineering research and design, 2013. 91(5): p. 883-903.

176.   Bowen, W.R., M.G. Jones, J.S. Welfoot, and H.N. Yousef, Predicting salt rejections at nanofiltration membranes using artificial neural networks. Desalination, 2000. 129(2): p. 147-162.

177.   Al-Zoubi, H., N. Hilal, N. Darwish, and A. Mohammad, Rejection and modelling of sulphate and potassium salts by nanofiltration membranes: neural network and Spiegler–Kedem model. Desalination, 2007. 206(1-3): p. 42-60.

178.   Shetty, G.R., H. Malki, and S. Chellam, Predicting contaminant removal during municipal drinking water nanofiltration using artificial neural networks. Journal of Membrane Science, 2003. 212(1-2): p. 99-112.

179.   Mousavi, M. and A. Avami, Modeling and simulation of water softening by nanofiltration using artificial neural network. 2006.
180.   Ammi, Y., L. Khaouane, and S. Hanini, Prediction of the rejection of organic compounds (neutral and ionic) by nanofiltration and reverse osmosis membranes using neural networks. Korean Journal of Chemical Engineering, 2015. 32: p. 2300-2310.
181.   Yangali-Quintanilla, V., A. Verliefde, T.-U. Kim, A. Sadmani, M. Kennedy, and G. Amy, Artificial neural network models based on QSAR for predicting rejection of neutral organic compounds by polyamide nanofiltration and reverse osmosis membranes. Journal of membrane science, 2009. 342(1-2): p. 251-262.
182.   Khaouane, L., Y. Ammi, and S. Hanini, Modeling the retention of organic compounds by nanofiltration and reverse osmosis membranes using bootstrap aggregated neural networks. Arabian Journal for Science and Engineering, 2017. 42: p. 1443-1453.
183.   Pardeshi, P.M., A.A. Mungray, and A.K. Mungray, Determination of optimum conditions in forward osmosis using a combined Taguchi–neural approach. Chemical Engineering Research and Design, 2016. 109: p. 215-225.
184.   Aish, A.M., H.A. Zaqoot, and S.M. Abdeljawad, Artificial neural network approach for predicting reverse osmosis desalination plants performance in the Gaza Strip. Desalination, 2015. 367: p. 240-247.
185.   Jafar, M.M. and A. Zilouchian, Prediction of critical desalination parameters using radial basis functions networks. Journal of Intelligent and Robotic Systems, 2002. 34: p. 219-230.
186.   Murthy, Z. and M.M. Vora, Prediction of reverse osmosis performance using artificial neural network. 2004.
187.   Abbas, A. and N. Al-Bastaki, Modeling of an RO water desalination unit using neural networks. Chemical Engineering Journal, 2005. 114(1-3): p. 139-143.
188.   Lee, Y.G., Y.S. Lee, J.J. Jeon, S. Lee, D.R. Yang, I.S. Kim, and J.H. Kim, Artificial neural network model for optimizing operation of a seawater reverse osmosis desalination plant. Desalination, 2009. 247(1-3): p. 180-189.
189.   Cabrera, P., J.A. Carta, J. González, and G. Melián, Artificial neural networks applied to manage the variable operation of a simple seawater reverse osmosis plant. Desalination, 2017. 416: p. 140-156.
190.   Righton, R., Development of an artificial neural network model for predicting the performance of a reverse osmosis (RO) unit. 2009, Curtin University.
191.   Libotean, D., J. Giralt, F. Giralt, R. Rallo, T. Wolfe, and Y. Cohen, Neural network approach for modeling the performance of reverse osmosis membrane desalting. Journal of Membrane Science, 2009. 326(2): p. 408-419.
192.   Khayet, M., C. Cojocaru, and M. Essalhi, Artificial neural network modeling and response surface methodology of desalination by reverse osmosis. Journal of Membrane Science, 2011. 368(1-2): p. 202-214.
193.   Garg, M.C. and H. Joshi, A new approach for optimization of small-scale RO membrane using artificial groundwater. Environmental technology, 2014. 35(23): p. 2988-2999.
194.   Moradi, A., V. Mojarradi, and M. Sarcheshmehpour, Prediction of RO membrane performances by use of artificial neural network and using the parameters of a complex mathematical model. Research on Chemical Intermediates, 2013. 39: p. 3235-3249.
195.   Salgado-Reyna, A., E. Soto-Regalado, R. Gómez-González, F. Cerino-Córdova, R. García-Reyes, M. Garza-González, and M. Alcalá-Rodríguez, Artificial neural networks for

modeling the reverse osmosis unit in a wastewater pilot treatment plant. Desalination and Water Treatment, 2015. 53(5): p. 1177-1187.

196.   Farahbakhsh, J., M. Delnavaz, and V. Vatanpour, Simulation and characterization of novel reverse osmosis membrane prepared by blending polypyrrole coated multiwalled carbon nanotubes for brackish water desalination and antifouling properties using artificial neural networks. Journal of Membrane Science, 2019. 581: p. 123-138.

197.   Ruiz-García, A. and J. Feo-García, Operating and maintenance cost in seawater reverse osmosis desalination plants. Artificial neural network based model. Desalination and Water Treatment, 2017. 73: p. 73-79.

198.   Jawad, J., A.H. Hawari, and S. Zaidi, Modeling of forward osmosis process using artificial neural networks (ANN) to predict the permeate flux. Desalination, 2020. 484: p. 114427.

199.   Jawad, J., A.H. Hawari, and S.J. Zaidi, Modeling and sensitivity analysis of the forward osmosis process to predict membrane flux using a novel combination of neural network and response surface methodology techniques. Membranes, 2021. 11(1): p. 70.

200.   Lee, K.S. and Z.W. Geem, A new meta-heuristic algorithm for continuous engineering optimization: harmony search theory and practice. Computer methods in applied mechanics and engineering, 2005. 194(36-38): p. 3902-3933.

201.   Rajabi Moshtaghi, H., A. Toloie Eshlaghy, and M.R. Motadel, A comprehensive review on meta-heuristic algorithms and their classification with novel approach. Journal of Applied Research on Industrial Engineering, 2021. 8(1): p. 63-89.

202.   Abualigah, L., M.A. Elaziz, A.M. Khasawneh, M. Alshinwan, R.A. Ibrahim, M.A. Al-Qaness, S. Mirjalili, P. Sumari, and A.H. Gandomi, Meta-heuristic optimization algorithms for solving real-world mechanical engineering design problems: a comprehensive survey, applications, comparative analysis, and results. Neural Computing and Applications, 2022: p. 1-30.

203.   Li, C., Z. Yang, H. Yan, and T. Wang. The application and research of the GA-BP neural network algorithm in the MBR membrane fouling. in Abstract and Applied Analysis. 2014. Hindawi.

204.   Li, W., C. Li, J. Nie, and T. Wang. The research of least squares support vector machine optimized by particle swarm optimization algorithm in the simulation MBR prediction. in 2015 2nd International Conference on Electrical, Computer Engineering and Electronics. 2015. Atlantis Press.

205.   Yusuf, Z., N.A. Wahab, and A. Abusam, Neural network-based model predictive control with CPSOGSA for SMBR filtration. International Journal of Electrical and Computer Engineering, 2017. 7(3): p. 1538.

206.   ENGINEERS'HANDBOOK, I., Process Control and Optimization. 2006, CRC press, BG Liptak, Florida, USA.

207.   Eberhart, R. and J. Kennedy. A new optimizer using particle swarm theory. in MHS'95. Proceedings of the sixth international symposium on micro machine and human science. 1995. Ieee.

208.   Haykin, S., Neural networks: a comprehensive foundation. 1998: Prentice Hall PTR.

209.   Zhou, P., Z. Li, S. Snowling, B.W. Baetz, D. Na, and G. Boyd, A random forest model for inflow prediction at wastewater treatment plants. Stochastic Environmental Research and Risk Assessment, 2019. 33: p. 1781-1792.

210. Li, X., Z. Li, W. Huang, and P. Zhou, Performance of statistical and machine learning ensembles for daily temperature downscaling. Theoretical and Applied Climatology, 2020. 140: p. 571-588.

211. Kovacs, D.J., Z. Li, B.W. Baetz, Y. Hong, S. Donnaz, X. Zhao, P. Zhou, H. Ding, and Q. Dong, Membrane fouling prediction and uncertainty analysis using machine learning: A wastewater treatment plant case study. Journal of Membrane Science, 2022. 660: p. 120817.

212. Kalisher, A.J. Advanced Manufacturing and Materials: Challenges for the Safety Professional. in ASSE Professional Development Conference and Exposition. 2016. OnePetro.

213. Spahiu, T., N. Grimmelsmann, A. Ehrmann, E. Shehi, and E. Piperi. On the possible use of 3D printing for clothing and shoe manufacture. in Proceedings of the 7th International Conference of Textile, Tirana, Albania. 2016.

214. Tan, D.K., M. Maniruzzaman, and A. Nokhodchi, Advanced pharmaceutical applications of hot-melt extrusion coupled with fused deposition modelling (FDM) 3D printing for personalised drug delivery. Pharmaceutics, 2018. 10(4): p. 203.

215. Yadav, D.K., R. Srivastava, and S. Dev, Design & fabrication of ABS part by FDM for automobile application. Materials Today: Proceedings, 2020. 26: p. 2089-2093.

216. 3D printing market size worldwide from 2013 to 2021.

217. Intelligence, M., 3D printing market – growth, trends, COVID-19 impact, and forecasts,2022-2027.

218. Grand View Research, Market research report, 3D printing (3DP) market analysis by printer type (desktop, industrial), by technology, by software, by application, by vertical, by region, and segment forecasts,2018-2025. 2017.

219. Gross, B.C., J.L. Erkal, S.Y. Lockwood, C. Chen, and D.M. Spence, Evaluation of 3D printing and its potential impact on biotechnology and the chemical sciences. 2014, ACS Publications.

220. Zukas, V. and J.A. Zukas, An introduction to 3D printing. 2015: First Edition Design Pub.

221. Azimi, P., D. Zhao, C. Pouzet, N.E. Crain, and B. Stephens, Emissions of ultrafine particles and volatile organic compounds from commercially available desktop three-dimensional printers with multiple filaments. Environmental science & technology, 2016. 50(3): p. 1260-1268.

222. Davis, A.Y., Q. Zhang, J.P. Wong, R.J. Weber, and M.S. Black, Characterization of volatile organic compound emissions from consumer level material extrusion 3D printers. Building and Environment, 2019. 160: p. 106209.

223. Byrley, P., W.K. Boyes, K. Rogers, and A.M. Jarabek, 3D printer particle emissions: Translation to internal dose in adults and children. Journal of aerosol science, 2021. 154: p. 105765.

224. Poikkimäki, M., V. Koljonen, N. Leskinen, M. Närhi, O. Kangasniemi, O. Kausiala, and M. Dal Maso, Nanocluster aerosol emissions of a 3D printer. Environmental Science & Technology, 2019. 53(23): p. 13618-13628.

225. Alberts, E., M. Ballentine, E. Barnes, and A. Kennedy, Impact of metal additives on particle emission profiles from a fused filament fabrication 3D printer. Atmospheric Environment, 2021. 244: p. 117956.

226. Zhang, Q., G. Sharma, J.P. Wong, A.Y. Davis, M.S. Black, P. Biswas, and R.J. Weber, Investigating particle emissions and aerosol dynamics from a consumer fused deposition

modeling 3D printer with a lognormal moment aerosol model. Aerosol Science and Technology, 2018. 52(10): p. 1099-1111.

227.   Ding, S., B.F. Ng, X. Shang, H. Liu, X. Lu, and M.P. Wan, The characteristics and formation mechanisms of emissions from thermal decomposition of 3D printer polymer filaments. Science of the Total Environment, 2019. 692: p. 984-994.

228.   House, R., N. Rajaram, and S. Tarlo, Case report of asthma associated with 3D printing. Occupational Medicine, 2017. 67(8): p. 652-654.

229.   Su, W.-C., Y. Chen, and J. Xi, Estimation of the deposition of ultrafine 3D printing particles in human tracheobronchial airways. Journal of Aerosol Science, 2020. 149: p. 105605.

230.   Park, J., O.h. Kwon, C. Yoon, and M. Park, Estimates of particulate matter inhalation doses during three‐dimensional printing: How many particles can penetrate into our body? Indoor air, 2021. 31(2): p. 392-404.

231.   Pandit, S., P. Singh, M. Sinha, and R. Parthasarathi, Integrated QSAR and adverse outcome pathway analysis of chemicals released on 3D printing using acrylonitrile butadiene styrene. Chemical Research in Toxicology, 2021. 34(2): p. 355-364.

232.   Roth, G.A., C.L. Geraci, A. Stefaniak, V. Murashov, and J. Howard, Potential occupational hazards of additive manufacturing. Journal of Occupational and Environmental hygiene, 2019. 16(5): p. 321-328.

233.   Stefaniak, A., R. LeBouf, M. Duling, J. Yi, A. Abukabda, C. McBride, and T. Nurkiewicz, Inhalation exposure to three-dimensional printer emissions stimulates acute hypertension and microvascular dysfunction. Toxicology and applied pharmacology, 2017. 335: p. 1-5.

234.   Krajnak, K., M. Farcas, W. McKinney, S. Waugh, K. Mandler, M. Jackson, J. Matheson, T. Thomas, and Y. Qian, Inhalation of particulate and emissions from 3 dimensional (3D) printers: Effects on the olfactory bulb (OB) and hypothalamic‐pituitary‐endocrine axes. The FASEB journal, 2021. 35.

235.   Farcas, M.T., A.B. Stefaniak, A.K. Knepp, L. Bowers, W.K. Mandler, M. Kashon, S.R. Jackson, T.A. Stueckle, J.D. Sisler, and S.A. Friend, Acrylonitrile butadiene styrene (ABS) and polycarbonate (PC) filaments three-dimensional (3-D) printer emissions-induced cell toxicity. Toxicology letters, 2019. 317: p. 1-12.

236.   Joob, B. and V. Wiwanitkit, Estimation of Cancer Risk Due to Exposure to Airborne Particle Emission of a Commercial Three-dimensional Printer. Indian journal of medical and paediatric oncology, 2017. 38(03): p. 409-409.

237.   Stephens, B., P. Azimi, Z. El Orch, and T. Ramos, Ultrafine particle emissions from desktop 3D printers. Atmospheric Environment, 2013. 79: p. 334-339.

238.   Zhang, Q., J.P. Wong, A.Y. Davis, M.S. Black, and R.J. Weber, Characterization of particle emissions from consumer fused deposition modeling 3D printers. Aerosol Science and Technology, 2017. 51(11): p. 1275-1286.

239.   ANSI, A., CAN/UL 2904 Standard Method for Testing and Assessing Particle and Chemical Emissions from 3D Printers. American National Standards Institute: Washington, DC, USA, 2019.

240.   Chýlek, R., L. Kudela, J. Pospíšil, and L. Šnajdárek, Fine particle emission during fused deposition modelling and thermogravimetric analysis for various filaments. Journal of Cleaner Production, 2019. 237: p. 117790.

241.   Sittichompoo, S., S. Kanagalingam, L. Thomas-Seale, A. Tsolakis, and J. Herreros, Characterization of particle emission from thermoplastic additive manufacturing. Atmospheric Environment, 2020. 239: p. 117765.

242.   Ding, S., M.P. Wan, and B.F. Ng, Dynamic analysis of particle emissions from FDM 3D printers through a comparative study of chamber and flow tunnel measurements. Environmental Science & Technology, 2020. 54(22): p. 14568-14577.

243.   Vance, M.E., V. Pegues, S. Van Montfrans, W. Leng, and L.C. Marr, Aerosol emissions from fuse-deposition modeling 3D printers in a chamber and in real indoor environments. Environmental Science & Technology, 2017. 51(17): p. 9516-9523.

244.   Gu, J., M. Wensing, E. Uhde, and T. Salthammer, Characterization of particulate and gaseous pollutants emitted during operation of a desktop 3D printer. Environment international, 2019. 123: p. 476-485.

245.   Potter, P.M., S.R. Al-Abed, F. Hasan, and S.M. Lomnicki, Influence of polymer additives on gas-phase emissions from 3D printer filaments. Chemosphere, 2021. 279: p. 130543.

246.   Mendes, L., A. Kangas, K. Kukko, B. Mølgaard, A. Säämänen, T. Kanerva, I. Flores Ituarte, M. Huhtiniemi, H. Stockmann-Juvala, and J. Partanen, Characterization of emissions from a desktop 3D printer. Journal of Industrial Ecology, 2017. 21(S1): p. S94-S106.

247.   Cheng, Y.-L., L.-C. Zhang, F. Chen, and Y.-H. Tseng, Particle emissions of material-extrusion-type desktop 3D printing: the effects of infill. International Journal of Precision Engineering and Manufacturing-Green Technology, 2018. 5: p. 487-497.

248.   Kwon, O., C. Yoon, S. Ham, J. Park, J. Lee, D. Yoo, and Y. Kim, Characterization and control of nanoparticle emission during 3D printing. Environmental science & technology, 2017. 51(18): p. 10357-10368.

249.   Viitanen, A.K., K. Kallonen, K. Kukko, T. Kanerva, E. Saukko, T. Hussein, K. Hämeri, and A. Säämänen, Technical control of nanoparticle emissions from desktop 3D printing. Indoor Air, 2021. 31(4): p. 1061-1071.

250.   Rao, C., F. Gu, P. Zhao, N. Sharmin, H. Gu, and J. Fu, Capturing PM2. 5 emissions from 3D printing via nanofiber-based air filter. Scientific reports, 2017. 7(1): p. 10366.

251.   Zhu, Q., Q. Yao, J. Liu, J. Sun, and Q. Wang, Emissions from the fused filament fabrication 3D printing with lignocellulose/polylactic acid filament. BioResources, 2020. 15(4): p. 7560.

252.   Zontek, T.L., S. Hollenbeck, J. Jankovic, and B.R. Ogle, Modeling particle emissions from three-dimensional printing with acrylonitrile–butadiene–styrene polymer filament. Environmental Science & Technology, 2019. 53(16): p. 9656-9663.

253.   Koeppe, A., C.A.H. Padilla, M. Voshage, J.H. Schleifenbaum, and B. Markert, Efficient numerical modeling of 3D-printed lattice-cell structures using neural networks. Manufacturing Letters, 2018. 15: p. 147-150.

254.   Williams, G., N.A. Meisel, T.W. Simpson, and C. McComb, Design repository effectiveness for 3D convolutional neural networks: Application to additive manufacturing. Journal of Mechanical Design, 2019. 141(11).

255.   Rojek, I., D. Mikołajewski, M. Macko, Z. Szczepański, and E. Dostatni, Optimization of extrusion-based 3D printing process using neural networks for sustainable development. Materials, 2021. 14(11): p. 2737.

256.   Gu, G.X., C.-T. Chen, D.J. Richmond, and M.J. Buehler, Bioinspired hierarchical composite design using machine learning: simulation, additive manufacturing, and experiment. Materials Horizons, 2018. 5(5): p. 939-945.

257.   He, H., Y. Yang, and Y. Pan, Machine learning for continuous liquid interface production: Printing speed modelling. Journal of Manufacturing Systems, 2019. 50: p. 236-246.

258.   Deng, L., B. Feng, and Y. Zhang, An optimization method for multi-objective and multi-factor designing of a ceramic slurry: Combining orthogonal experimental design with artificial neural networks. Ceramics International, 2018. 44(13): p. 15918-15923.

259.   Okaro, I.A., S. Jayasinghe, C. Sutcliffe, K. Black, P. Paoletti, and P.L. Green, Automatic fault detection for laser powder-bed fusion using semi-supervised machine learning. Additive Manufacturing, 2019. 27: p. 42-53.

260.   Scime, L. and J. Beuth, Using machine learning to identify in-situ melt pool signatures indicative of flaw formation in a laser powder bed fusion additive manufacturing process. Additive Manufacturing, 2019. 25: p. 151-165.

261.   Pham, G.N., S.-H. Lee, O.-H. Kwon, and K.-R. Kwon, Anti-3D weapon model detection for safe 3D printing based on convolutional neural networks and D2 shape distribution. Symmetry, 2018. 10(4): p. 90.

262.   Kim, Y., C. Yoon, S. Ham, J. Park, S. Kim, O. Kwon, and P.-J. Tsai, Emissions of nanoparticles and gaseous material from 3D printer operation. Environmental science & technology, 2015. 49(20): p. 12044-12053.

263.   Yi, J., R.F. LeBouf, M.G. Duling, T. Nurkiewicz, B.T. Chen, D. Schwegler-Berry, M.A. Virji, and A.B. Stefaniak, Emission of particulate matter from a desktop three-dimensional (3D) printer. Journal of Toxicology and Environmental Health, Part A, 2016. 79(11): p. 453-465.

264.   Floyd, E.L., J. Wang, and J.L. Regens, Fume emissions from a low-cost 3-D printer with various filaments. Journal of occupational and environmental hygiene, 2017. 14(7): p. 523-533.

265.   Stefaniak, A.B., R.F. LeBouf, J. Yi, J. Ham, T. Nurkewicz, D.E. Schwegler-Berry, B.T. Chen, J.R. Wells, M.G. Duling, and R.B. Lawrence, Characterization of chemical contaminants generated by a desktop fused deposition modeling 3-dimensional printer. Journal of occupational and environmental hygiene, 2017. 14(7): p. 540-550.

266.   Gu, J., E. Uhde, M. Wensing, F. Xia, and T. Salthammer, Emission control of desktop 3D printing: the effects of a filter cover and an air purifier. Environmental Science & Technology Letters, 2019. 6(8): p. 499-503.

267.   Jeon, H., J. Park, S. Kim, K. Park, and C. Yoon, Effect of nozzle temperature on the emission rate of ultrafine particles during 3D printing. Indoor Air, 2020. 30(2): p. 306-314.

268.   Dunn, K.L., K.H. Dunn, D. Hammond, and S. Lo, Three-dimensional printer emissions and employee exposures to ultrafine particles during the printing of thermoplastic filaments containing carbon nanotubes or carbon nanofibers. Journal of Nanoparticle Research, 2020. 22: p. 1-13.

269.   Dunn, K.L., D. Hammond, K. Menchaca, G. Roth, and K.H. Dunn, Reducing ultrafine particulate emission from multiple 3D printers in an office environment using a prototype engineering control. Journal of Nanoparticle Research, 2020. 22: p. 1-11.

270.   Bernatikova, S., A. Dudacek, R. Prichystalova, V. Klecka, and L. Kocurkova, Characterization of ultrafine particles and VOCs emitted from a 3D printer. International Journal of Environmental Research and Public Health, 2021. 18(3): p. 929.

271.   Wojnowski, W., R. Marcinkowska, and B. Zabiegała. Real-time monitoring of volatiles and particles emitted from thermoplastic filaments during 3D printing. in IOP Conference Series: Materials Science and Engineering. 2021. IOP Publishing.

272.   Stabile, L., M. Scungio, G. Buonanno, F. Arpino, and G. Ficco, Airborne particle emission of a commercial 3D printer: the effect of filament material and printing temperature. Indoor Air, 2017. 27(2): p. 398-408.

273.   Katz, E.F., J.D. Goetz, C. Wang, J.L. Hart, B. Terranova, M.L. Taheri, M.S. Waring, and P.F. DeCarlo, Chemical and physical characterization of 3D printer aerosol emissions with and without a filter attachment. Environmental Science & Technology, 2019. 54(2): p. 947-954.

274.   Zhou, Y., X. Kong, A. Chen, and S. Cao, Investigation of ultrafine particle emissions of desktop 3D printers in the clean room. Procedia Engineering, 2015. 121: p. 506-512.

275.   Steinle, P., Characterization of emissions from a desktop 3D printer and indoor air measurements in office settings. Journal of Occupational and Environmental Hygiene, 2016. 13(2): p. 121-132.

276.   Deng, Y., S.-J. Cao, A. Chen, and Y. Guo, The impact of manufacturing parameters on submicron particle emissions from a desktop 3D printer in the perspective of emission reduction. Building and Environment, 2016. 104: p. 311-319.

277.   McDonnell, B., X. Jimenez Guzman, M. Dolack, T.W. Simpson, and J.M. Cimbala. 3D printing in the wild: a preliminary investigation of air quality in college maker spaces. in 2016 International Solid Freeform Fabrication Symposium. 2016. University of Texas at Austin.

278.   Bharti, N. and S. Singh, Three-dimensional (3D) printers in libraries: Perspective and preliminary safety analysis. Journal of chemical education, 2017. 94(7): p. 879-885.

279.   Du Preez, S., A. Johnson, R.F. LeBouf, S.J. Linde, A.B. Stefaniak, and J. Du Plessis, Exposures during industrial 3-D printing and post-processing tasks. Rapid Prototyping Journal, 2018.

280.   Youn, J.-S., J.-W. Seo, S. Han, and K.-J. Jeon, Characteristics of nanoparticle formation and hazardous air pollutants emitted by 3D printer operations: from emission to inhalation. RSC advances, 2019. 9(34): p. 19606-19612.

281.   Setyawati, M.I., D. Singh, S.P. Krishnan, X. Huang, M. Wang, S. Jia, B.H.R. Goh, C.G. Ho, R. Yusoff, and M.H. Kathawala, Occupational inhalation exposures to nanoparticles at six Singapore printing centers. Environmental science & technology, 2020. 54(4): p. 2389-2400.

282.   Chan, F.L., C.-Y. Hon, S.M. Tarlo, N. Rajaram, and R. House, Emissions and health risks from the use of 3D printers in an occupational setting. Journal of Toxicology and Environmental Health, Part A, 2020. 83(7): p. 279-287.

283.   Khaki, S., E. Duffy, A.F. Smeaton, and A. Morrin, Monitoring of particulate matter emissions from 3D printing activity in the home setting. Sensors, 2021. 21(9): p. 3247.

284.   Ding, S. and B.F. Ng, Particle emission levels in the user operating environment of powder, ink and filament-based 3D printers. Rapid Prototyping Journal, 2021. 27(6): p. 1124-1132.

285.   Bai, X., B. Stein, K. Smith, and D. Isaac, Effects of reprocessing on additives in ABS plastics, detected by gas chromatography/mass spectrometry. Progress in Rubber Plastics and Recycling Technology, 2012. 28(1): p. 1-14.

286. Hinds, W.C. and Y. Zhu, Aerosol technology: properties, behavior, and measurement of airborne particles. 2022: John Wiley & Sons.

287. Ren, J., M. Tang, and A. Novoselac, Experimental study to quantify airborne particle deposition onto and resuspension from clothing using a fluorescent-tracking method. Building and environment, 2022. 209: p. 108580.

288. BAM, F.I.f.M.R. and Testing, Test Method for the Determination of Emissions from Hardcopy Devices within the Award of the Blue Angel Ecolabel for Equipment with Printing Function according to RAL-UZ-171. 2012.

289. Jeong, C.-H. and G.J. Evans, Inter-comparison of a fast mobility particle sizer and a scanning mobility particle sizer incorporating an ultrafine water-based condensation particle counter. Aerosol Science and Technology, 2009. 43(4): p. 364-373.

290. Zimmerman, N., C.-H. Jeong, J.M. Wang, M. Ramos, J.S. Wallace, and G.J. Evans, A source-independent empirical correction procedure for the fast mobility and engine exhaust particle sizers. Atmospheric Environment, 2015. 100: p. 178-184.

291. UL, UL 2823, GREENGUARD Certification Program Method for Measuring and Evaluating Chemical and Particle Emissions from Electronic Equipment Using Dynamic Environmental Chambers. 2014, Underwriters Laboratories Northbrook, IL.

292. ASTM, D., 6670-01-Standard Practice for Full-Scale Chamber Determination of Volatile Organic Emissions from Indoor Materials. 2001, Products.

293. Zhang, J., D.-R. Chen, and S.-C. Chen, Sampling and characterization of particle emission from the 3D FDM printing. Journal of Building Engineering, 2022. 52: p. 104476.

294. Taylor, A.A., E.L. Freeman, and M.J. van der Ploeg, Regulatory developments and their impacts to the nano-industry: A case study for nano-additives in 3D printing. Ecotoxicology and Environmental Safety, 2021. 207: p. 111458.

295. Wojtyła, S., P. Klama, and T. Baran, Is 3D printing safe? Analysis of the thermal treatment of thermoplastics: ABS, PLA, PET, and nylon. Journal of occupational and environmental hygiene, 2017. 14(6): p. D80-D85.

296. Wojtyła, S., P. Klama, K. Śpiewak, and T. Baran, 3D printer as a potential source of indoor air pollution. International Journal of Environmental Science and Technology, 2020. 17: p. 207-218.

297. Mak, S.L., W. Tang, C.H. Li, W.H. Chiu, and H. Lau. A critical review on hazardous chemical emissions and particle from fused decomposition modelling (FDM) machine. in 2019 IEEE International Conference on Industrial Engineering and Engineering Management (IEEM). 2019. IEEE.

298. Rodríguez-Hernández, A., A. Chiodoni, S. Bocchini, and R. Vazquez-Duhalt, 3D printer waste, a new source of nanoplastic pollutants. Environmental pollution, 2020. 267: p. 115609.

299. Sikora, P., M. Chougan, K. Cuevas, M. Liebscher, V. Mechtcherine, S.H. Ghaffar, M. Liard, D. Lootens, P. Krivenko, and M. Sanytsky, The effects of nano-and micro-sized additives on 3D printable cementitious and alkali-activated composites: A review. Applied Nanoscience, 2021: p. 1-19.

300. Dobrzyńska, E., D. Kondej, J. Kowalska, and M. Szewczyńska, State of the art in additive manufacturing and its possible chemical and particle hazards. Indoor air, 2021. 31(6): p. 1733-1758.

301. Min, K., Y. Li, D. Wang, B. Chen, M. Ma, L. Hu, Q. Liu, and G. Jiang, 3D printing-induced fine particle and volatile organic compound emission: An emerging health risk. Environmental Science & Technology Letters, 2021. 8(8): p. 616-625.
302. Ciornei, M., R.I. Iacobici, I.D. Savu, and D. Simion. FDM 3D printing process-risks and environmental aspects. in Key Engineering Materials. 2021. Trans Tech Publ.
303. Manoj, A., M. Bhuyan, S.R. Banik, and M.R. Sankar, Review on particle emissions during fused deposition modeling of acrylonitrile butadiene styrene and polylactic acid polymers. Materials Today: Proceedings, 2021. 44: p. 1375-1383.
304. Byrley, P., M.A.G. Wallace, W.K. Boyes, and K. Rogers, Particle and volatile organic compound emissions from a 3D printer filament extruder. Science of the Total Environment, 2020. 736: p. 139604.
305. Long, N., E. Bonnema, K. Field, and P. Torcellini, ANSI/ASHRAE/USGBC/IES Standard 189.1-2009. Evaluation, 2010.
306. (IMAP), A.I.o.C.S., Single Assessment Report. Benzaldehyde: Human Health Tier II Assessment. 2016.
307. Chen, S.-C., C.-J. Tsai, C.-Y. Huang, H.-D. Chen, S.-J. Chen, C.-C. Lin, J.-H. Tsai, C.C.-K. Chou, S.-C.C. Lung, and W.-R. Huang, Chemical mass closure and chemical characteristics of ambient ultrafine particles and other PM fractions. Aerosol Science and Technology, 2010. 44(9): p. 713-723.
308. Kong, X., C. Guo, Z. Lin, S. Duan, J. He, Y. Ren, and J. Ren, Experimental study on the control effect of different ventilation systems on fine particles in a simulated hospital ward. Sustainable Cities and Society, 2021. 73: p. 103102.
309. Zhang, J., Z. Long, W. Liu, and Q. Chen, Strategy for studying ventilation performance in factories. Aerosol and Air Quality Research, 2016. 16(2): p. 442-452.
310. Azimi, P., T. Fazli, and B. Stephens, Predicting concentrations of ultrafine particles and volatile organic compounds resulting from desktop 3D printer operation and the impact of potential control strategies. Journal of Industrial Ecology, 2017. 21(S1): p. S107-S119.
311. Chen, S.-C., C.-J. Tsai, C.C.-K. Chou, G.-D. Roam, S.-S. Cheng, and Y.-N. Wang, Ultrafine particles at three different sampling locations in Taiwan. Atmospheric Environment, 2010. 44(4): p. 533-540.
312. Ohata, S., N. Moteki, T. Mori, M. Koike, and Y. Kondo, A key process controlling the wet removal of aerosols: new observational evidence. Scientific reports, 2016. 6(1): p. 34113.
313. Kariz, M., M. Sernek, and M.K. Kuzman, Effect of humidity on 3D-printed specimens from wood-PLA filaments. Wood Res, 2018. 63(5): p. 917-922.
314. Wu, Z., A. Tran, D. Rincon, and P.D. Christofides, Machine learning-based predictive control of nonlinear processes. Part I: theory. AIChE Journal, 2019. 65(11): p. e16729.
315. Espadoto, M., N.S.T. Hirata, and A.C. Telea, Deep learning multidimensional projections. Information Visualization, 2020. 19(3): p. 247-269.
316. Gan, Z., H. Li, S.J. Wolff, J.L. Bennett, G. Hyatt, G.J. Wagner, J. Cao, and W.K. Liu, Data-driven microstructure and microhardness design in additive manufacturing using a self-organizing map. Engineering, 2019. 5(4): p. 730-735.
317. Qi, X., G. Chen, Y. Li, X. Cheng, and C. Li, Applying neural-network-based machine learning to additive manufacturing: current applications, challenges, and future perspectives. Engineering, 2019. 5(4): p. 721-729.

318.   Wohlkinger, W. and M. Vincze. Shape-based depth image to 3D model matching and classification with inter-view similarity. in 2011 IEEE/RSJ International Conference on Intelligent Robots and Systems. 2011. IEEE.

319.   Grun, F. and B. Blumberg, Minireview: the case for obesogens. Molecular Endocrinology, 2009. 23(8): p. 1127-1134.

320.   Pan, G., T. Hanaoka, M. Yoshimura, S. Zhang, P. Wang, H. Tsukino, K. Inoue, H. Nakazawa, S. Tsugane, and K. Takahashi, Decreased serum free testosterone in workers exposed to high levels of di-n-butyl phthalate (DBP) and di-2-ethylhexyl phthalate (DEHP): a cross-sectional study in China. Environmental health perspectives, 2006. 114(11): p. 1643-1648.

321.   Stefaniak, A.B., L.N. Bowers, A.K. Knepp, M.A. Virji, E.M. Birch, J.E. Ham, J. Wells, C. Qi, D. Schwegler-Berry, and S. Friend, Three-dimensional printing with nano-enabled filaments releases polymer particles containing carbon nanotubes into air. Indoor air, 2018. 28(6): p. 840-851.

322.   Byrley, P., B.J. George, W.K. Boyes, and K. Rogers, Particle emissions from fused deposition modeling 3D printers: Evaluation and meta-analysis. Science of The Total Environment, 2019. 655: p. 395-407.

323.   Gormley, P. and M. Kennedy. Diffusion from a stream flowing through a cylindrical tube. in Proceedings of the Royal Irish Academy. Section A: Mathematical and Physical Sciences. 1948. JSTOR.

324.   Schripp, T., S. Mulakampilly, W. Delius, E. Uhde, M. Wensing, T. Salthammer, R. Kreuzig, M. Bahadir, L. Wang, and L. Morawska, Comparison of ultrafine particle release from hardcopy devices in emission test chambers and office rooms. Gefahrstoffe-Reinhaltung der Luft, 2009. 69(3): p. 71-76.

325.   Chen, S.-C., J. Wang, H. Fissan, and D.Y. Pui, Optimizing filtration experiments for length and fractal dimension characterization of non-spherical particles. Aerosol Science and Technology, 2015. 49(8): p. 547-555.

326.   Chen, S.-C., J. Wang, H. Fissan, and D.Y. Pui, Exposure assessment of nanosized engineered agglomerates and aggregates using Nuclepore filter. Journal of nanoparticle research, 2013. 15: p. 1-15.